# Ab initio Study of Organic Molecules Adsorbed on Technologically Relevant Surfaces

**He Lin**

**A thesis presented for the degree of Doctor of Philosophy**


**Department of Materials Science**

**University of Milano-Bicocca**

**Italy**

**June 2016**

# Ab initio Study of Organic Molecules Adsorbed on Technologically Relevant Surfaces

Ph.D. Thesis

He Lin

Supervisor: Prof. Gian Paolo Brivio

Co-Supervisor: Dr. Guido Fratesi

# Abstract

In this thesis we investigated materials of relevance to photovoltaics and organic electronics, and the studied systems involving surfaces with technological applications, such as graphene and $TiO_2$. We make use of the density functional theory (DFT) to calculate the structural and electronic properties of the system, and the Ab initio molecular dynamics to check the temperature dependent effects. Finally, we simulate the core excited spectroscopic measurements by the transition potential approach and use the Time-Dependent DFT to calculate the optical absorption coefficient.

We first focused on covalent adsorption of aromatic radicals onto graphene.. Our results show that the adsorption of an aromatic radical generates two spin-dependent mid-gap states located around the Fermi energy which induce magnetic moments in graphene. This phenomenon can modify the band of pristine graphene and introduces a gap, but this effect is almost independent of the specific chemical functionalization by the aromatic radical. In this way it is possible to magnetize graphene just using s, p electrons without any d-metal impurities.

Next we investigated the adsorption of prototypical dyes (catechol and isonicotinic acid) on the $TiO_2$ anatase (101) and rutile (110) surfaces by DFT, Ab initio molecular dynamics and TDDFT calculations. We found that thermal

fluctuation induce changes in the position of the molecular levels around the $TiO_2$ valence band edge. For the anatase (101) surface, these fluctuations enhance significantly the low-energy tail of the absorption spectrum, and the sensitization can be improved by increasing the hybridization between the adsorbed dye and $TiO_2$ states. But sensitization effects are less relevant for the rutile (110) surface. As an extension of this work towards more realistic materials for applications, we studied two more complex species, namely perylene-tetra-carboxylic-dianhydride (PTCDA) and perylene-tetra-carboxylic-diimide (PTCDI) adsorbed on the $TiO_2$ rutile (110) surface. These molecules determine a more pronounced sensitization effect with a substantial red-shift of the first peak of the dye/$TiO_2$ absorption relative to the free dye.

Finally, the unoccupied molecular orbitals of corannulene ($C_{20}H_{10}$) were studied by the transition-potential (TP-DFT) approach, and we collaborated with the experimental group of Dr. Andrea Goldoni at ELETTRA, Trieste, Italy who deposited a monolayer of such molecules on Ag(111), and measured X-ray photoemission spectroscopy (XPS) and Near-edge X-ray absorption fine structure (NEXAFS). From our calculation of the intrinsic dichroism resulting from the corannulene curvature and polarization dependent NEXAFS measurement of the unoccupied molecular orbitals, the molecules were found to be oriented at a small tilt angle of ~5 degrees from the surface. The molecular tilting results in different electron screening of the core hole in XPS. The corresponding core level shifts broaden the C 1s photoemission peak and produce a splitting of the NEXAFS LUMO resonance, which is strongly contributed by all the C atoms. Higher energy transitions involve different molecular orbitals ($\pi$ and $\sigma$) depending on the excited C atom.

# Contents

# Chapter 1

# Introduction

The understanding of adsorption phenomena occurring at surfaces is of central importance for many fields of research in Physics and Chemistry. In particular it is fundamental for the materials of relevance to organic electronics and photovoltaics. Though much information on these subjects may be obtained by means of surface science experiments, a full understanding can be reached with the combined resort to numerical simulations.

Since density functional theory (DFT) was introduced in the 1960's [1,2], it has demonstrated the most important tool in the study of ground state properties of condensed matter systems. Together with the steadily increase of accessible computational power, it is now possible to investigate the molecule-surface systems with continuously increasing complexity by means of DFT calculations, and DFT generally gives correct adsorption sites and binding energies in excellent agreement with experiments. The idea of DFT can be extended with the time-dependent density functional theory (TDDFT) to deal with electronic excitations [3] and calculate optical spectra of molecules and solids. In addition, the Ab initio molecular dynamics can be used to check the temperature dependent effects [4].

Graphene have been proposed as a versatile material for many potential applications [5,6]. The possibility of tailoring the electronic properties of graphene has attracted a considerable scientific interest and several methods have been

attempted [7–9]. The use of adsorbed organic species would exploit the large versatility of chemical synthesis for optimal tuning and would incorporate molecules possibly playing active role in devices. However, adsorption of aromatic molecules, have been shown to mostly determine the opening of a small gap [10], while aromatic radicals are expected to induce stronger modifications through covalent bonding [11].

In the field of organic molecule derived devices, the surfaces of $TiO_2$ have shown to be a technologically important material for many applications, most notably, in photovoltaic, including solar energy conversion [12,13], such as Dye-sensitized solar cells (DSSCs). As prototypical models for $TiO_2$-based DSSCs, catechol and isonicotinic acid adsorbed on $TiO_2$ have attracted a considerable scientific interest [14–26]. Theoretical studies of the geometry and electronic properties available in the literature [14–31] have been performed using DFT but only recently a cluster calculation [31] has employed TDDFT methods to determine the absorption coefficient. Since experiments and photovoltaic applications are usually carried out at room temperature, it is important to understand how thermal fluctuations affect the electronic structure and hence the optical absorption spectrum of dye-sensitized $TiO_2$.

Corannulene, $C_{20}H_{10}$, presents an intriguing curvature (it can be seen as a cap of $C_{60}$ fullerene) and $C_{5v}$ symmetry [32,33]. Now available on the kilogram scale thanks to a practical synthetic route recently developed [34], corannulene is a strong electron acceptor and good conductor, so it attracts interest for applications in organic and hybrid devices as well as for the possibility of studying symmetry mismatch on surfaces and $\pi$–$\pi$ interactions ubiquitous in molecular complexes in nanoscience, materials chemistry, and biochemistry.

This thesis is organized as follows. In Chapter 1 the theoretical framework and methods are introduced. Chapter 2 addresses the question of how the covalent attachment of aromatic radicals may modify the electronic properties of graphene. In particular, the analysis will proceed by examining whether spin-polarization could be achieved by bonding of aromatic radicals, where the resulting magnetism would be distributed, and to what extent the properties of the bonded species would change upon adsorption. In Chapter 3, we investigate the adsorption of catechol and isonicotinic acid on the $TiO_2$ anatase (101) and rutile (110) surfaces. The effects of thermal fluctuations on the structure and absorption spectrum of dye-sensitized $TiO_2$ is discussed. In addition, the sensitization effects on the anatase (101) and rutile (110) surfaces will be compared. As an extension towards more realistic materials for applications, the properties of two more complex molecular species, namely perylene-tetra-carboxylic-dianhydride (PTCDA) and perylene-tetra-carboxylic-diimide (PTCDI) adsorbed on the $TiO_2$ rutile (110) surface will be shown. In Chapter 4, the unoccupied molecular orbitals of corannulene are investigated by experimental and simulated electron core-level spectroscopy, and we discuss in detail the tilting of molecule on the surface.

# Chapter 2

# Computational Methods and measurements

*Since in this thesis the result of numerical simulations for the organic molecular adsorbed on technologically relevant surfaces will be presented, the theoretical methods and measurements will be described in this chapter.*

## 2.1 Density Functional Theory

Density Functional Theory (DFT) has proven to be successful in accounting for structural and electronic properties of a vast class of materials, ranging from atoms and molecules to crystals and other complex extended systems. The DFT is based upon two theorems first proved by Hohenberg and Kohn (HK) [1]:

Theorem I: For any systems of interacting electrons in an external potential $V_{\text{ext}}(\mathbf{r})$, the potential $V_{\text{ext}}(\mathbf{r})$ is determined uniquely by the ground state particle density $\rho_0(\mathbf{r})$.

Theorem II: Consider the energy functional

$$E_{\mathrm{HK}}[\rho] = F_{\mathrm{HK}}[\rho] + \int V_{\mathrm{ext}}(\mathbf{r})\rho(\mathbf{r})d\mathbf{r} \tag{2.1}$$

where $F_{\mathrm{HK}}[\rho]$ is a universal functional of the density which does not depend on the external potential $V_{\mathrm{ext}}(\mathbf{r})$. $E_{\mathrm{HK}}[\rho]$ is minimal at the exact ground-state density $\rho_0(\mathbf{r})$ relative to arbitrary variations of $\rho$ constrained to a fixed number of particles.

The HK theorems provide a general theoretical result but not a way to solve the quantum many-body problem in practice for a system of $N$ electrons. This is accomplished by the Kohn-Sham approach [2], which rewrites the Hohenberg/Kohn energy functional (2.1) in the form

$$E_{\mathrm{KS}}[\rho] = T_0[\rho] + E_{\mathrm{H}}[\rho] + E_{\mathrm{xc}}[\rho] + \int V_{\mathrm{ext}}(\mathbf{r})\rho(\mathbf{r})d\mathbf{r} \tag{2.2}$$

where the independent-particle kinetic energy $T_0$ (atomic units are used) is given by

$$T_0 = \frac{1}{2}\sum_{i=1}^{N}\int d\mathbf{r}\,|\nabla\psi_i(\mathbf{r})|^2 \tag{2.3}$$

$\psi_i(r)$ is the one-particle orbitals. $E_{\mathrm{H}}[\rho]$ is the classical Coulomb interaction functional (the Hartree energy) equal to

$$E_{\mathrm{H}}[\rho] = \frac{1}{2}\iint \frac{\rho(\mathbf{r})\rho(\mathbf{r}')}{|\mathbf{r}-\mathbf{r}'|}d\mathbf{r}d\mathbf{r}' \tag{2.4}$$

The exchange-correlation energy $E_{\mathrm{xc}}[\rho]$ is defined as the difference $F_{\mathrm{HK}}[\rho] - T_0[\rho] - E_{\mathrm{H}}[\rho]$. In order to apply DFT in practice, a good approximation for $E_{\mathrm{xc}}[\rho]$ is necessary; this problem will be addressed in the next

section. By applying the variational principle of Theorem II to the HK energy functional in Eq. (2.2) we obtain the Euler equation

$$\mu = V_{\mathrm{KS}}(\mathbf{r}) + \frac{\delta T_0[\rho]}{\delta \rho(\mathbf{r})} \tag{2.5}$$

where

$$V_{\mathrm{KS}}(\mathbf{r}) = V_{\mathrm{H}}(\mathbf{r}) + V_{\mathrm{xc}}(\mathbf{r}) + V_{\mathrm{ext}}(\mathbf{r}) = \int \frac{\rho(\mathbf{r}')}{|\mathbf{r}-\mathbf{r}'|} d\mathbf{r}' + V_{\mathrm{xc}}(\mathbf{r}) + V_{\mathrm{ext}}(\mathbf{r}) \tag{2.6}$$

and $\mu$ is a Lagrange multiplier from the conservation of the total number of particles. By minimizing Eq. (2.2) it is possible to write a single particle Schrödinger auxiliary equation with potential $V_{\mathrm{KS}}(\mathbf{r})$ which gives the same ground state charge density as that of the interacting system.

$$\left[-\frac{1}{2}\nabla^2 + V_{\mathrm{KS}}(\mathbf{r})\right]\psi_i(\mathbf{r}) = \varepsilon_i \psi_i(\mathbf{r}) \tag{2.7}$$

The one-particle orbitals $\psi_i(r)$ can be then used to construct the density

$$\rho(\mathbf{r}) = \sum_{i=1}^{N} |\psi_i(\mathbf{r})|^2 \tag{2.8}$$

Eq. (2.7) is named Kohn-Sham (KS) equation. Since $V_{\mathrm{KS}}(\mathbf{r})$ depends on the charge density, Eq. (2.7) has to be solved self-consistently. It is worthy to note that the eigenvalues and eigenfunctions do not have any physical meaning, but they are just mathematical devices used to obtain the ground-state energy and charge density of the full many-body system.

## 2.2 Approximations for the exchange-correlation functional

The Kohn-Sham approach separates out the independent-particle kinetic energy (2.3) and the Hartree term (2.4) from the universal functional $F_{\mathrm{HK}}[\rho]$, and the remaining exchange-correlation functional $E_{\mathrm{xc}}[\rho]$ can be reasonably approximated as a local or nearly local functional of the density. The first and most widespread approximation to $E_{\mathrm{xc}}[\rho]$ is the Local Density Approximation (LDA) [2], in which the exchange-correlation energy is simply an integral over all space with the exchange-correlation energy density at each point assumed to be the same as that of a homogeneous electron gas with the same density,

$$E_{\mathrm{xc}}^{\mathrm{LDA}}[\rho] = \int \varepsilon_{\mathrm{xc}}^{\mathrm{hom}}(\rho(\mathbf{r}))\rho(\mathbf{r})d\mathbf{r} \tag{2.9}$$

where $\varepsilon_{\mathrm{xc}}^{\mathrm{hom}}(\rho(\mathbf{r}))$ is the exchange-correlation energy per electron of the homogeneous electron gas at density $\rho(\mathbf{r})$. The LDA can be extended to include a spin dependent $\rho(\mathbf{r})$, and that is the so-called Local Spin Density Approximation (LSDA). The self-interaction is automatically avoided in the Hartree-Fork (HF) approach, while in the LSDA, an explicit correction has to be considered. The LSDA works remarkably well even in the systems in which the electron gas is rather inhomogeneous. Typically LSDA results in a good accuracy in reproducing experimental structural and vibrational properties of strongly bound systems. It usually overestimates bonding energies and underestimates bond lengths. In order to improve the LSDA, the Generalized Gradient Approximation (GGA), where the gradient of the density is also considered, has been introduced. In the GGA, the exchange-correlation energy depends both on the electron density and on its gradient:

$$E_{\mathrm{xc}}^{\mathrm{GGA}}[\rho_{\uparrow},\rho_{\downarrow}]=\int f(\rho_{\uparrow},\rho_{\downarrow},\nabla\rho_{\uparrow},\nabla\rho_{\downarrow})d\mathbf{r} \tag{2.10}$$

where $f$ is a parametrized analytic function. To obtain reasonable results the function $f$ must be chosen carefully. The GGA introduces non-local gradient dependence and allows one to recover the well known relationship of the exchange-correlation hole of LSDA. In comparison with LSDA, GGA tends to improve total energies, atomization energies, energy barriers and structural energy differences. The exchange-correlation functional used in this thesis is the Perdew-Burke-Ernzerhof (PBE) functional [35]. The PBE functional is based on Perdew-Wang 1991 (PW91) [36]. It contains a unified real space cutoff for exchange and correlation holes to avoid spurious long range parts in the second order gradient expansion of density.

In addition, in this thesis the dye-semiconductor interfaces are influenced by the vdW forces. The vdW interactions called London forces appear between non-polar particles which are polarizable. Due to charge fluctuations, instantaneous dipoles arise, which induce a dipolar moment in other polarizable particles. This results in a coupled movement of electrons in both systems, which lowers the total energy of the system and causes the particles to attract one another. The dispersion forces stems from the frequency-dependency of the interaction. The GGA functional can be corrected to include this kind of long-range interactions. One of commonly used approaches is Grimme's DFT-D2 [37]. It is based on Becke's power-series ansatz from 1997 and is explicitly parameterized by including damped atom-pairwise dispersion corrections of the form $C_6 \cdot R^{-6}$. It is suggested as an efficient and accurate quantum chemical method for large systems where dispersion forces are of general importance. In this thesis Quantum Espresso has been used to perform the

DFT calculations for PTCDA and PTCDI/rutile (110), and the Grimme approach is adopted.

## 2.3 Time-Dependent Density Functional Theory

The standard DFT as described in Sec. 2.1 is a ground-state theory, and is hence not meant for the calculation of electronic excitations. However, one can extend the idea of static DFT with the time-dependent density functional theory (TDDFT) to deal with electronic excitations. The formal foundation of TDDFT is the Runge-Gross (RG) theorem (1984) [38]. The RG theorem proves that there is a one-to-one correspondence between the time-dependent external potential $V_{\text{ext}}(\mathbf{r},t)$, and the electronic density $\rho(\mathbf{r},t)$, for many body systems evolving from a fixed initial state $\Psi(t_0)$.

When the RG theorem applies it is possible to extend the KS equation (2.7) to the time-dependent case:

$$\left[-\frac{1}{2}\nabla^2 + V_{\text{eff}}(\mathbf{r},t)\right]\psi_i(\mathbf{r},t) = i\frac{\partial}{\partial t}\psi_i(\mathbf{r},t) \tag{2.11}$$

$$\rho(\mathbf{r},t) = \sum_{i=1}^{N} |\psi_i(\mathbf{r},t)|^2 \tag{2.12}$$

where $V_{\text{eff}}(\mathbf{r},t) = V_{\text{H}}(\mathbf{r},t) + V_{\text{xc}}(\mathbf{r},t) + V_{\text{ext}}(\mathbf{r},t)$ is the effective time-dependent potential felt by the electrons. It consists of the sum of the time-dependent Hartree term $V_{\text{H}}(\mathbf{r},t)$, the exchange-correlation potential $V_{\text{xc}}(\mathbf{r},t)$, plus the external time-dependent potential $V_{\text{ext}}(\mathbf{r},t)$.

Using TDDFT, one can study how a system behaves when subject to a time-dependent external perturbation. The key formula is a Dyson-like representation

of the exact linear density response $\chi$ of an interacting many electron system in terms of the non-interacting Kohn-Sham response $\chi_0$:

$$\chi(\mathbf{r},\mathbf{r}',\omega)=\chi_0(\mathbf{r},\mathbf{r}',\omega)+\int d\mathbf{r}_1 d\mathbf{r}_2 \chi_0(\mathbf{r},\mathbf{r}_1,\omega)K(\mathbf{r}_1,\mathbf{r}_2,\omega)\chi(\mathbf{r}_2,\mathbf{r}',\omega) \qquad (2.13)$$

which has to be solved iteratively and where $K$ has been introduced as

$$K(\mathbf{r}_1,\mathbf{r}_2,\omega)=\frac{1}{|\mathbf{r}_1-\mathbf{r}_2|}+f_{\mathrm{xc}}(\mathbf{r}_1,\mathbf{r}_2,\omega) \qquad (2.14)$$

where $f_{\mathrm{xc}}(\mathbf{r}_1,\mathbf{r}_2,\omega)$ is the frequency dependent exchange-correlation kernel.

The exact exchange-correlation kernel is of course unknown, and practical calculations must rely on some approximation. The simplest approximation (the random phase approximation or RPA) (cite FW p.153) consists in neglecting $f_{\mathrm{xc}}$:

$$f_{\mathrm{xc}}(\mathbf{r}_1,\mathbf{r}_2,\omega)=0 \qquad (2.15)$$

Actually the most commonly used approximation, due to its simplicity, is the adiabatic local-density approximation (ALDA) [3], in which $f_{\mathrm{xc}}(\mathbf{r}_1,\mathbf{r}_2,\omega)$ is approximated by the ($\omega$-independent) functional derivative of the LDA exchange-correlation potential.

$$f_{\mathrm{xc}}(\mathbf{r}_1,\mathbf{r}_2)=\delta(\mathbf{r}_1-\mathbf{r}_2)\frac{\partial V_{\mathrm{xc}}^{\mathrm{LDA}}(\rho(\mathbf{r}_1),\mathbf{r}_1)}{\partial\rho(\mathbf{r}_1)} \qquad (2.16)$$

Apart from ALDA, each ground-state functional such GGA or a hybrid one can yield a corresponding adiabatic approximation. All applications of TDDFT to calculate

absorption spectra (see Chapter 5) in this thesis will use the adiabatic PBE approximation.

## 2.4 Car-Parrinello approach

The Car-Parrinello approach is a method to simulate molecular dynamics proposed by Roberto Car and Michele Parrinello in 1985 [4]. It explicitly introduces the electronic degrees of freedom as fictitious dynamical variables to keep the system close to the Born-Oppenheimer surface. According to this basic idea, Car and Parrinello introduced the following Lagrangian

$$\mathcal{L}_{\mathrm{CP}} = \sum_I \frac{1}{2} M_I \dot{\mathbf{R}}_I^2 + \sum_i \mu \left\langle \dot{\phi}_i \middle| \dot{\phi}_i \right\rangle - \left\langle \Psi_0 \middle| H_{\mathrm{e}}^{\mathrm{KS}} \middle| \Psi_0 \right\rangle + \sum_{i,j} \Lambda_{ij} \left( \left\langle \phi_i \middle| \phi_j \right\rangle - \delta_{ij} \right) \qquad (2.17)$$

where the first term is the nuclei kinetic energy, the second term is the fictitious kinetic energy of the KS orbitals $\{\phi_i\}$, the third term is KS energy, and the last term is a Lagrange multiplier term. Here, $M_I$ and $\mathbf{R}_I$ are mass and position of the *I*-th nucleus, $\mu$ is the fictitious mass, $\Psi_0$ is the many-body wave function constructed with the orbitals obtained from KS Hamiltonian $H_{\mathrm{e}}^{\mathrm{KS}}$, and $\Lambda_{ij}$ are the Lagrange multipliers. The Lagrangian in Eq. (2.17) generates the corresponding Car-Parrinello equations of motion:

$$M_I \ddot{\mathbf{R}}_I(t) = -\nabla_I \left\langle \Psi_0 \middle| H_{\mathrm{e}}^{\mathrm{KS}} \middle| \Psi_0 \right\rangle \qquad (2.18)$$

$$\mu \ddot{\phi}_i(t) = -H_{\mathrm{e}}^{\mathrm{KS}} \phi_i + \sum_j \Lambda_{ij} \phi_j \qquad (2.19)$$

The fictitious mass $\mu$ controls the lowest and maximum electron frequencies ($\omega_{\mathrm{e}}^{\min}$ and $\omega_{\mathrm{e}}^{\max}$) according to

$$\omega_{\mathrm{e}}^{\min} \propto \left( \frac{E_{\mathrm{gap}}}{\mu} \right)^{1/2} \qquad (2.20)$$

$$\omega_{\mathrm{e}}^{\max} \propto \left( \frac{E_{\mathrm{cut}}}{\mu} \right)^{1/2} \tag{2.21}$$

where $E_{\mathrm{gap}}$ is the electronic energy difference between the lowest unoccupied (LUMO) and the highest occupied (HOMO) orbital, and $E_{\mathrm{cut}}$ is the largest kinetic energy in an expansion of the wave function in terms of a plane wave basis set. In order to guarantee adiabatic separation of the electronic and nuclear subsystems and thus stable Car-Parrinello propagation, the nuclear and electronic subsystems should be dynamically separated, in the sense that the difference between the lowest electron frequency $\omega_{\mathrm{e}}^{\min}$ and the highest phonon frequency $\omega_{\mathrm{n}}^{\max}$ should be large. But both $\omega_{\mathrm{n}}^{\max}$ and $E_{\mathrm{gap}}$ are quantities that are dictated by the physics of the system. Therefore, the only parameter to control adiabatic separation is the fictitious mass $\mu$. Decreasing $\mu$ not only shifts the electronic spectrum upwards on the frequency scale as desired, but also leads to an increase of the maximum electron frequency $\omega_{\mathrm{e}}^{\max}$. As the time step is inversely proportional to $\omega_{\mathrm{e}}^{\max}$, the larger $\omega_{\mathrm{e}}^{\max}$, the smaller time step. Hence we have to make a compromise on the control parameter $\mu$ [39].

As already discussed in Chapter 1, the experimental spectra of the dye/$TiO_2$ system are generally recorded at room temperature, and it is convenient to take into account the effects of thermal fluctuations. In the Car-Parrinello approach, this is achieved by introducing a thermostat into the system. For the simulations discussed in this thesis, the Nosé-Hoover thermostat is used [40–42]. In this method, Hoover extended the analysis of Nosé to derive a set of equations of motion

$$\begin{aligned} \dot{q} &= p / m \\ \dot{p} &= F(q) - \zeta p \end{aligned} \tag{2.22}$$

where $q$ and $p$ are representative of the coordinates and momenta of particles in a physical system, and $F(q)$ is the force which is derived from the interparticle

potentials. In this case the friction coefficient $\zeta$ is given by the first-order differential equation

$$\dot{\zeta} = \left[\sum p^2 / m - XkT\right] / Q \tag{2.23}$$

where $T$ is the specified temperature, $X$ is the number of degrees of freedom in the physical system, $k$ is Boltzmann's constant, and the parameter $Q$ determines the time scale of temperature fluctuation. The function $\dot{\zeta}$ can acquire a positive or negative sign if the instantaneous kinetic energy of the particle is higher or lower than $XkT$. This leads to damping or acceleration of the particle and thus to cooling or heating.

## 2.5 X-ray Photoelectron Spectroscopy (XPS)

X-ray photoelectron spectroscopy (XPS) is a widely used surface analysis method in many fields of study in physics and chemistry. It probes the energy distribution of electrons emitted from X-ray-irradiated compounds. Its relevance is based on the fact that even if the atomic core electrons are not involved in chemical bonding, their binding energy may change depending on the chemical environment of the atom. Hence it is convenient to characterize the chemical composition and local atomic bonding of surfaces.

XPS operates on the principle of the photoelectric effect. In the photoemission process, an atom absorbs a photo of a known energy ($h\nu$) resulting in ejection of a core level electron. Energy conservation for the photoemission process can be expressed as:

$$h\nu = BE + KE_{\text{det}}(e) + e\phi_{\text{det}} \tag{2.24}$$

where $h\nu$ is the energy of the incoming photo, $BE$ is the binding energy of the photoemitted core electron, $KE_{\mathrm{det}}(e)$ is the photoelectron kinetic energy, and $\phi_{\mathrm{det}}$ is the work function of the detector [43]. The binding energy is defined as the difference between the energy of the ionized system $E^{+}$ and that of ground state $E^{0}$:

$$BE = E^{+} - E^{0} \tag{2.25}$$

where $E^{+}$ is the energy of the ionized system and $E^{0}$ is that of the system in the ground state. As already mentioned the precise value of the binding energy is sensitive to the chemical environment such as surface potential, change in geometry, charge transfer etc. The resulting changes in the binding energy is called core level shift (CLS) or chemical shifts. The CLS can then be used to identify differences in chemical environment among atoms of the same species.

From DFT calculations there are two models to be used for the prediction of chemical shifts. One is the initial state approximation [43], which neglects all effects related to the relaxation of the valence and core electrons upon ionization of the core. This approximation can be used to describe CLS due to the change in the potential which the core electrons feel in different chemical environments, and only requires a ground state calculation. Another one is the $\Delta$SCF approach [43]. In contrast to the initial state approximation, it assumes that the valence electrons fully relax to the presence of the hole created at the core during the photoemission process. The core level energies are then calculated as a difference of total energies between the initial and final states of the system. The $\Delta$SCF approach involves the effects of valence relaxation after the core ionization, accounting for the screening of the core hole

created in the photoemission process. In addition, it is assumed that the valence electrons are in a pseudo ground state in the presence of the core hole, and that the geometry does not change after ionization. In this thesis the ΔSCF approach is adopted, and the binding energy $(BE)$ is computed using the Eq. (2.25). The energy of the ionized system, $E^+$, is computed using a pseudopotential generated including a core hole. Thus the CLS of an atom $i$ with respect to reference atom $j$ can be expressed by the following Eq. (2.29). The energy $E^0$ equals $E^0_{ref}$ if they are the ground state energies of the same system.

$$\mathrm{CLS}_i = BE_i - BE_{j(ref)} = (E^+_i - E^0) - (E^+_{j(ref)} - E^0_{ref}) = E^+_i - E^+_{j(ref)} \qquad (2.26)$$

In the case of the corannulene (see Chapter 5), for $E^+_{j(ref)}$, we used the weighted average of the system energies with a full core hole on the 1s level of every inequivalent C atoms in the molecules.

## 2.6 Optical Absorption

Absorption spectroscopy measures how well a sample absorbs or transmits electromagnetic radiation at a given range of photon frequencies. Different from photoemission, the excited electron is not removed from the sample, and it is merely lifted to an unoccupied state above the Fermi level. The electron stays within the vicinity of the created ion and feels the presence of the core hole. When a sample absorbs a phonon with energy $\omega$, an excitation with that particular energy is created. The different energy ranges mean different practicalities and the measurement techniques vary greatly. The commonly used techniques include UV-visible absorption (UV/Vis) and X-ray absorption (XAS). In XAS on a solid we observe that

differently from optical absorption the initial electron state is a dispersionless, narrow, and deeply bound core one. Thus the XAS can be described by single-electron approach, and this case will be discussed in Sec 2.7.

However, the description of optical absorption is beyond the single-electron approach, we have to consider a system described by a many-body Hamiltonian $H$, subjected to a time-dependent external perturbation $V_{\text{ext}}(t)$ [44]. The total Hamiltonian can be written as

$$H_{\text{tot}} = H + V_{\text{ext}}(t) \tag{2.27}$$

The linear coefficient linking the response of the system to the perturbation is the response function. In this context, the density-density linear response function $\chi$ is defined as

$$\delta\rho(\mathbf{r},t) = \int dt' \int d\mathbf{r}' \chi(\mathbf{r},\mathbf{r}',t-t') V_{\text{ext}}(\mathbf{r}',t') \tag{2.28}$$

where $\delta\rho$ is the first-order variation of the electron density, and $V_{\text{ext}}$ is the external perturbation. The function $\chi$ also represents the reducible polarizability already defined in Eq. (2.28), so the formalism of choice that has been adopted in this thesis is TDDFT.

The irreducible polarizability $P$ can be defined in a similar way:

$$\delta\rho(\mathbf{r},t) = \int dt' \int d\mathbf{r}' P(\mathbf{r},\mathbf{r}',t-t') V_{\text{tot}}(\mathbf{r}',t') \tag{2.29}$$

where $V_{\text{tot}}$ is the total screened potential, defined as the sum of the potentials of the external charge ($V_{\text{ext}}$) plus that of the induced one ($V_{\text{ind}}$). The reducible and irreducible polarizabilities satisfy the Dyson equation

$$\chi(\mathbf{r},\mathbf{r}',t-t') = P(\mathbf{r},\mathbf{r}',t-t') + \int d\mathbf{r}'' \int d\mathbf{r}''' P(\mathbf{r},\mathbf{r}',t-t') V_{\text{ee}}(\mathbf{r}''-\mathbf{r}''') \chi(\mathbf{r}''',\mathbf{r}',t-t') \tag{2.30}$$

where $V_{\text{ee}}$ is the Coulomb interaction.

In a finite system, $\chi$ yields the photoabsorption cross section along a direction $z$ ($\sigma_{zz}$), via

$$\sigma_{zz}(\omega) = \frac{4\pi\omega}{c} \operatorname{Im}\{\alpha_{zz}(\omega)\} \tag{2.31}$$

where $\operatorname{Im}\{\alpha_{zz}(\omega)\}$ is the imaginary part of the dynamical polarizability defined as:

$$\alpha_{zz}(\omega) = -\int d\mathbf{r} \int d\mathbf{r}' z \chi(\mathbf{r},\mathbf{r}',\omega) z' \tag{2.32}$$

Since the dynamical polarizability is a tensor, the spherically averaged photoabsorption cross section $\sigma$ can be written as:

$$\sigma(\omega) = \frac{4\pi\omega}{3c} \operatorname{Im}\{\operatorname{Tr}\,\alpha(\omega)\} \tag{2.33}$$

In this thesis, we used Liouville-Lanczos approach of the Quantum-ESPRESSO package to compute the optical absorption [45,46]. The main advantage of the Liouville-Lanczos approach to TDDFT is that it gives direct access to the observable spectrum without having to calculate individual eigenvectors in the continuum of the spectrum.

## 2.7 Near Edge X-ray Absorption Fine Structure Spectroscopy (NEXAFS)

Near Edge X-ray Absorption Fine Structure Spectroscopy (NEXAFS) also known as X-ray absorption near edge structure (XANES) is a type of absorption spectroscopy that refers to the features in the X-ray absorption spectra (XAS) due to the photo-absorption cross section for electronic transitions from an atomic core level to final unoccupied states in the energy region of 50/100 eV above the selected atomic core level energy. It is a particularly useful and effective technique for probing the surface chemistry and electronic structure of materials. In the case of adsorption of planar organic molecules, like polyaromatic hydrocarbons, it is possible to extract information regarding the orientation of the molecule on the substrate [47]. The NEXAFS $\pi^*$ resonances give information about the out-of-plane and $\sigma^*$ resonances regarding the in-plane orientations of the molecule.

To calculate a NEXAFS spectrum, it is essential to compute the absorption cross section. This may be computed by the Fermi golden rule as a sum of probabilities per unit of time of making a transition from an initial state to an unoccupied final state through an interaction Hamiltonian [48]. The key point of absorption cross section calculation lies in the solution of the Schrödinger equation for the final and initial states. In order to solve the Schrödinger equation, the approach depends on the localized or delocalized character of final states. Crystal field multiplet theory is employed to the calculation of localized final state with strong electron-electron interactions. If the final state is delocalized, multielectronic interactions are weak and single-electron approaches based on the DFT are usually adopted [49].

In a single-electron approach, the XAS cross section can be written as

$$\sigma(\omega) = 4\pi^2 \alpha_0 \hbar\omega \sum_f \left| M_{i\to f} \right|^2 \delta(E_f - E_i - \hbar\omega) \tag{2.34}$$

where $\hbar\omega$ is the photon energy, $\alpha_0$ is the fine-structure constant, and $M_{i\to f}$ is the transition amplitude between an initial core state $\left|\psi_i\right\rangle$ with energy $E_i$, localized on the absorbing atom site, and the final state $\left|\psi_f\right\rangle$ with energy $E_f$ [49].

By extending DFT to deal with excited states, the energy of the photon absorbed in a transition from the ground state to an excited one can be expressed as the total energy difference of the two states:

$$h\nu = E^{\text{tot}}(N; n_i = 0, n_f = 1) - E^{\text{tot}}(N; n_i = 1, n_f = 0) \tag{2.35}$$

where $E^{\text{tot}}(N; n_i = 1, n_f = 0)$ is the ground-state energy of the $N$-electron system, and $E^{\text{tot}}(N; n_i = 0, n_f = 1)$ is the total energy with one electron promoted from the initially occupied level $i$ to an empty level $f$. Due to the localized character of the core level, it is adequate to treat the hole wave function in the exciton statically. According to the transition-state method proposed by Slater, and extended by Janak, Eq. (2.35) can be rewritten in terms of the KS eigenvalues $\varepsilon_i$ and $\varepsilon_f$ at half filling,

$$h\nu = \varepsilon_f(N; n_i = 1/2, n_f = 1/2) - \varepsilon_i(N; n_i = 1/2, n_f = 1/2) \tag{2.36}$$

In this way, the screening effects up to second order in the occupation numbers can be included. However, this approach requires a separate calculation of the electronic structure of the system for each final-state orbital, which makes it impractical for generating a complete NEXAFS spectrum including the continuum part. To overcome this problem, Triguero et al.[50] proposed the so-called transition-potential

approach as an approximation to Slater's by removing half an electron from the final state

$$h\nu = \varepsilon_f(N-1/2; n_i = 1/2, n_f = 0) - \varepsilon_i(N-1/2; n_i = 1/2, n_f = 0) \qquad (2.37)$$

This approach is defined as the half core hole (HCH) approximation, and it works remarkably well in a wide range of systems. The HCH method is used in this thesis, where, we take into account the XSPECTRA code [51–53] of the Quantum-ESPRESSO platform [54] to compute the spectrum. The plane wave basis sets and pseudopotentials are used, and the transition matrix element is expressed by reconstructing the unoccupied wave functions in the core region by means of the projector augmented wave method. Then, by using the recursion method based on the Lanczos algorithm, the absorption cross section is expressed as a continued fraction.

# Chapter 3

# Magnetism in Graphene Functionalized by Aromatic Radical

*In this chapter we have shown that it is possible to introduce a band gap and magnetism into graphene by covalent adsorption of radicals. The functionalization effect is independent of the adsorption of radical species, and we obtained almost the same aromatic species as those in gas phase but anchored on a surface.*

## 3.1 Introduction

Graphene, the two-dimensional $sp^2$-hybridized carbon lattice, has attracted considerable attention from both the experimental and theoretical scientific communities. Because of its novel properties, such as exceptional thermal and mechanical ones, high electrical conductivity, graphene sheets have been proposed as a versatile material for many potential applications [5,6]. However, pristine graphene does not display intrinsic magnetism. Several procedures have been developed to induce magnetism in graphene. One is to create carbon vacancies [7–9] like nanoholes, where magnetism appears at the edge of the vacancy. Another one is to cut the two-dimensional graphene into finite systems with zigzag edges like one-dimensional nanoribbons or zero-dimensional quantum dots [56–58]. The disadvantages of the above processes are the following: (1) The integrity of the

graphene structure is destroyed by vacancies or by cutting it into nanosize sheets, where magnetism is inhomogeneously distributed. (2) In practical applications, nanoribbons need to be assembled, and the magnetic moments in the zigzag edges can be easily quenched in the assembly [59]. Magnetism can also be introduced by transition metal [60–61] or magnetic molecule adsorption [62]. Due to the strong d–d interactions, it is easy for transition metal atoms to form clusters [59], whereas the adsorption of the magnetic molecule such as $CrO_3$ only reflects the magnetism of the adsorbate [62]. All these methods are difficult to control. In addition, adsorption of hydrogen atoms onto graphene can induce $sp^2$–$sp^3$ rehybridization of the valence C orbitals, and thus results in a band gap and magnetism [59,63–69]. However, how to tune the electronic structure of functionalized graphene is still a topic of debate [68].

Recently, experimental studies have shown that the covalent attachment of aromatic radicals to pristine graphene can be used to tailor its electronic properties [70–74]. For example, a highly reactive free radical is produced by heating a diazonium salt, which attacks the $sp^2$ carbon atoms of graphene forming a covalent bond. In this way, it has been possible to decorate graphene with nitrophenyls [71] and this technique is well established for nanotube functionalization [75]. Similar to hydrogen functionalized graphene, this reaction transforms the hybridization state of carbon atoms from $sp^2$ to $sp^3$. Moreover, it determines a band gap and a remarkable decrease of conductivity [70,72]. In a more recent experimental study, a local diazonium modification of pristine graphene is demonstrated at the micrometer scale using scanning electrochemical cell microscopy [73]. In this study, the film density, the level of $sp^2$–$sp^3$ rehybridization and the extent of multilayer formation can be controlled. Additionally, Phenyl groups can also be attached to graphene in solution by photochemical methods [70,74]. As pointed out aromatic radicals form a covalent

bond with graphene and consequently are expected to modify its electronic properties more significantly than aromatic molecules. For the latter systems the weak molecule-surface interaction only determines the opening of a small gap [76]. Therefore, the functionalization of pristine graphene sheets with aromatic radicals is manageable and desirable. Additionally, Sánchez-Portal et al. investigated theoretically the electronic structure of covalently functionalized carbon nanotubes and graphene using density functional theory (DFT) calculations. They found that regardless of the particular adsorbate, a spin moment with value of 1.0 $\mu_B$ per molecule is induced, a result that is the induced magnetic properties are independent of the considered adsorbates.

In spite of the just mentioned experimental and theoretical studies, it is fundamental to understand how the covalent attachment of aromatic radicals modifies the electronic properties of graphene, as well as how they are influenced by the different species. In particular, magnetism could be induced in graphene by covalent bonding, as it is known it occurs with hydrogen. This raises the questions whether spin-polarization could be achieved by bonding of aromatic radicals, where the resulting magnetism would be distributed, and to what extent the properties of the bonded species would change upon adsorption.

To address these issues and to further contribute to the understanding of the aromatic organic adsorbate/graphene interaction, we have performed a theoretical study on adsorption of aromatic radicals onto graphene at low coverage. The basic idea is to attach one dehydrogenated aromatic radical, say methoxyphenyl, phenyl, and nitrophenyl, to pristine graphene. In this way, we span from an electron donor (the methoxy group in methoxyphenyl) to an electron acceptor (the nitryl group in nitrophenyl), while phenyl is an intermediate electron donor–acceptor system. By

using atomic hydrogen as a benchmark adsorbate, we are able to address the above questions by reporting the results of a numerical investigation on such systems.

## 3.2 Computational Method

The structural and electronic calculationss of aromatic radicals on graphene are based on DFT at the level of generalized gradient approximation (GGA) using the Perdew-Burke-Ernzerholf (PBE) functional [35] as implemented in the Quantum-ESPRESSO package [54]. A 5×5 graphene cell was used to avoid the lateral interaction between adsorbates. The Brillouin zone is sampled using a 6×6×1 Γ-centered *k*-point mesh for the relaxation of geometric structures and total energy calculations. To calculate the density of states, we adopt a 36×36×1 Γ-centered *k*-point grid. A vacuum space of 20 Å normal to the graphene plane is used to avoid interactions between two layers. The kinetic energy cutoff is set to 35 Ry, and the convergence of energy and force are $1\times10^{-6}$ Ry and 0.001 Ry per a.u., respectively. The accuracy of our procedure was tested by calculating the lattice constant of graphene; our calculated result of 2.463 Å is in very good agreement with the experimental value of 2.46 Å. We also computed the geometric structure of methoxybenzene in the gas phase, and obtaining results are in good agreement with the experimental ones [77].

## 3.3 Structural and electronic properties

### 3.3.1 Geometry and Adsorption Energy

In this section we investigate the structure of graphene interacting with an adsorbed aromatic species (*R*). The adsorption geometry is obtained by varying the

position of the center of mass of the radical with respect to the surface of pristine graphene and optimizing the full system. It is found that the optimal position of all adsorbed radicals is on top of a carbon atom (denoted as $A_0$; see Figure 3.1a) and perpendicular to the graphene plane. As shown in Figure 3.1b, the distortion of the graphene layer is significant, and the $A_0$ site carbon atom is lifted out of the graphene plane. We quantify the distortion by computing the height ($h$) of $A_0$ site carbon atom over the nearest-neighbor $B$-site carbon atoms. A vertical displacement from pristine graphene is also observed for surrounding atoms, but this is smaller (0.21 Å at most) and rapidly decays to zero as distance from the $A_0$ site increases. In Figure 3.1b, we further define the radical/$A_0$ bond length, $d_{AC}$, and the radical–$A_0$–$B$ bond angle, θ. In addition, we define the adsorption energy ($E_{ads}$) as

$$E_{ads} = E(R/\overline{g}) - E(g) - E(R) \tag{3.1}$$

where $E(g)$, $E(R)$, and $E(R/\overline{g})$ are the energy of pristine graphene, the energy of the adsorbate, and the total energy of the full system, respectively.

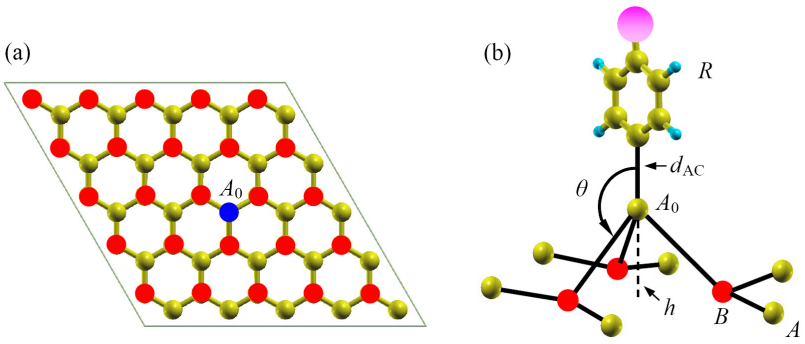


Figure 3.1: Top view of the supercell of (a) a 5×5 graphene structure. Yellow/red dots are the $A$/$B$ sites, the blue dot indicates the $A_0$ site atom. (b) Overhead view of the local distortion around $A_0$. The pink ball indicates the H atom in phenyl being replaced by donor or acceptor groups in this study.

Table 3.1: Structural and energetic properties of the adsorbates. The properties listed are the height ($h$) of the $A_0$ carbon atom, the angle (θ), and the adsorbate–carbon distance ($d_{AC}$) defined in Figure 1b, and the adsorption energy ($E_{ads}$)

| Adsorbate | $h$ (Å) | θ (°) | $d_{AC}$ (Å) | $E_{ads}$ (eV) |
|---|---|---|---|---|
| Hydrogen | 0.341, 0.357[a] | 103.0 | 1.132, 1.140[a] | −0.81, −0.84[b] |
| Methoxyphenyl | 0.417 | 107.1 | 1.589 | −0.32 |
| Phenyl | 0.417 | 107.3 | 1.594 | −0.26 |
| Nitrophenyl | 0.419 | 107.5 | 1.592 | −0.29 |

[a] Ref. 67 , [b] Ref. 65.

The structural properties and adsorption energies are summarized in Table 3.1 for hydrogen and the different aromatic species. The aromatic radicals distort the graphene sheet by a greater amount than hydrogen, while their adsorption energies are smaller than that of hydrogen. For each radical, the heights ($h$) and $d_{AC}$ are similar, and the bond angles (θ) are about 107°, which are closer to the angle (109.5°) of the $sp^3$ hybridization than that obtained by adsorbing hydrogen. The relatively small adsorption energy values do not imply a weak interaction: indeed, $E_{ads}$ includes a large energy cost to deform the graphene lattice, which can be estimated as deformation energy $E(\bar{g}) - E(g) = 0.96\,\text{eV}$ for methoxyphenyl adsorbed on graphene, where $E(\bar{g})$ is the energy of the deformed graphene. The adsorption of methoxyphenyl on deformed graphene hence releases adsorption energy of 1.28 eV, which is consistent with a covalent bond. Also the radical–graphene distance (~1.6 Å) is shorter than that for typical van der Waals (vdW) coupled systems. Thus the vdW interaction is not considered in this system. As all adsorption energies are negative

we are confident that adsorption is stable. Since the properties of aromatic adsorbed radicals on graphene are similar, in the following sections we only discuss those of methoxyphenyl in more detail due to its experimental interest. It is also worth to note that methoxyphenyl has the largest adsorption energy of the aromatic radicals considered, while phenyl has the smallest one in agreement with opposite radical-surface distances $d_{AC}$.

### 3.3.2 Electronic Structure

We compute the electronic structure of the radical/graphene system using DFT at the Kohn-Sham level. This can be considered as the zero-order approximation to the many body approach [78,79]. As of graphene, it has been shown that neglecting quasiparticle effects yields to underestimate the Fermi velocity (by 17%) [80] in the ±2 eV energy window around the Fermi level, without affecting the zero band gap. In addition, regarding the affinity and ionization energy of the adsorbed radicals, their precise values are not relevant for the current discussion of magnetism. For pristine graphene, the $p_z$ orbitals are perpendicular to the plane of the carbon ring and combine to form an extensive π-bonding network. The resulting delocalized π-electrons lead to a metallic and nonmagnetic 2D sheet. The calculated electronic band and total density of states (DOS) of the radical/graphene structures are shown in Figure 3.2, where they are compared to those of the pristine graphene. We can see that the adsorption of the radical significantly alters the graphene electronic structure. Instead of the Dirac cones of graphene, a gap opens up. The majority and minority band degeneracy is broken, and the total magnetic moment is 1.0 $\mu_B$ for each adsorbed aromatic species. Furthermore, radical adsorption generates two

spin-dependent midgap bands just below and above the Fermi energy of pristine graphene, and the magnetic moment is due to those midgap states.

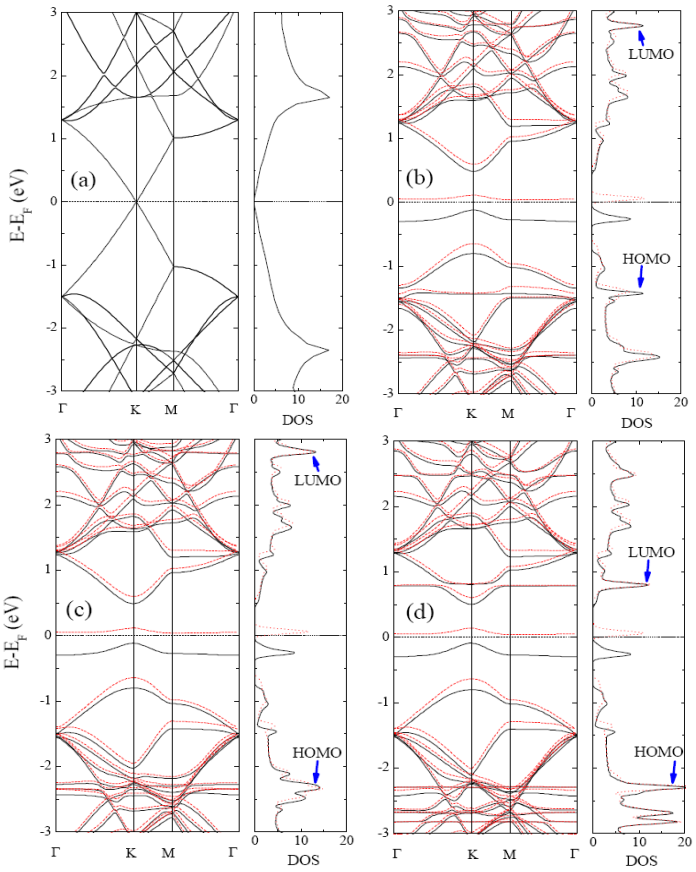


Figure 3.2: Band structure and total DOS for (a) graphene, (b) methoxyphenyl/graphene, (c) phenyl/graphene, and (d) nitrophenyl/graphene. In (b), (c), and (d), the solid and dashed curves represent the majority and minority spin populations, respectively.

Table 3.2: Calculated band gap (indirect) for midgap states and the direct gap at the K point between majority spin band and minority spin ones. All values in eV

| Adsorbate | Midgap | Majority spin | Minority spin |
|---|---|---|---|
| Hydrogen | 0.23 | 1.22 | 1.24 |
| Methoxyphenyl | 0.16 | 1.29 | 1.24 |
| Phenyl | 0.16 | 1.29 | 1.24 |
| Nitrophenyl | 0.13 | 1.31 | 1.25 |

To quantify which extent the adsorption of aromatic radicals modifies the band gap of *R*/graphene, we calculated the band gap for the midgap states and the majority spin and minority spin bands, and the results are listed in Table 3.2. Note that the energy separation between midgap states is smaller for the radical/graphene system than for the hydrogen/graphene one, while the differences of band gaps for various radical species are almost negligible. Thus we remark that compared with the hydrogen/graphene system the adsorption of aromatic radicals reduces the band gap, but changing their functionalization results into a minor effect. From Figure 3.2b–d, we can also see that the alignment of molecular orbitals [the highest occupied molecular orbital (HOMO) and the lowest unoccupied molecular orbital (LUMO) vs Fermi level] varies consistently for the different adsorbed molecules (see arrows), and all midgap states lie at about the same energy. To further understand this effect, we show the total DOS in Figure 3a1 together with the projected DOS (PDOS) on graphene (Figure 3.3a2), methoxyphenyl (Figure 3.3a3) and the DOS of methoxybenzene in Figure 3.3a4. Our results show that the two midgap states are contributed by graphene orbitals, not by methoxyphenyl ones. The two sharp features in the PDOS of graphene at about zero energy are absent in that of the methoxyphenyl. Due to the interaction with the graphene, the DOS of adsorbed methoxyphenyl is broadened, but the relative position of the peaks is consistent with that of methoxybenzene in gas phase (see Figure 3.3a3–a4). To further investigate the effect of adsorption on the HOMO and LUMO molecular states, in Figure 3.3 b1–b2 we compare the HOMO and LUMO wavefunctions of free methoxybenzene with the energy-integrated local density of states (ILDOS) corresponding to ranges

($E_{min}$, $E_{max}$) around the HOMO and LUMO of the adsorbed methoxyphenyl, defined as:

$$\mathrm{ILDOS}(\mathbf{r}) = \int_{E_{\min}}^{E_{\max}} \sum_{n\mathbf{k}} \omega_{\mathbf{k}} \left|\psi_{n\mathbf{k}}(\mathbf{r})\right|^2 \delta(E - \varepsilon_{n\mathbf{k}}) dE \qquad (3.2)$$

where $\omega_{\mathbf{k}}$ is the weight of points, and $\psi_{n\mathbf{k}}(\mathbf{r})$ and $\varepsilon_{n\mathbf{k}}$ are the eigenfunctions and eigenvalues of the full system, respectively. It is found that the molecular orbitals of methoxyphenyl are little affected by adsorption. These results suggest that the midgap states are independent of the alignment of the molecular orbitals, that the adsorbed radical nearly preserves the gas phase electronic properties and that the extended aromatic system of graphene is not disrupted by the interaction with graphene. Interestingly, it implies that the net result of the radical adsorption is to get almost the same aromatic species as those in the gas phase but anchored on a surface.

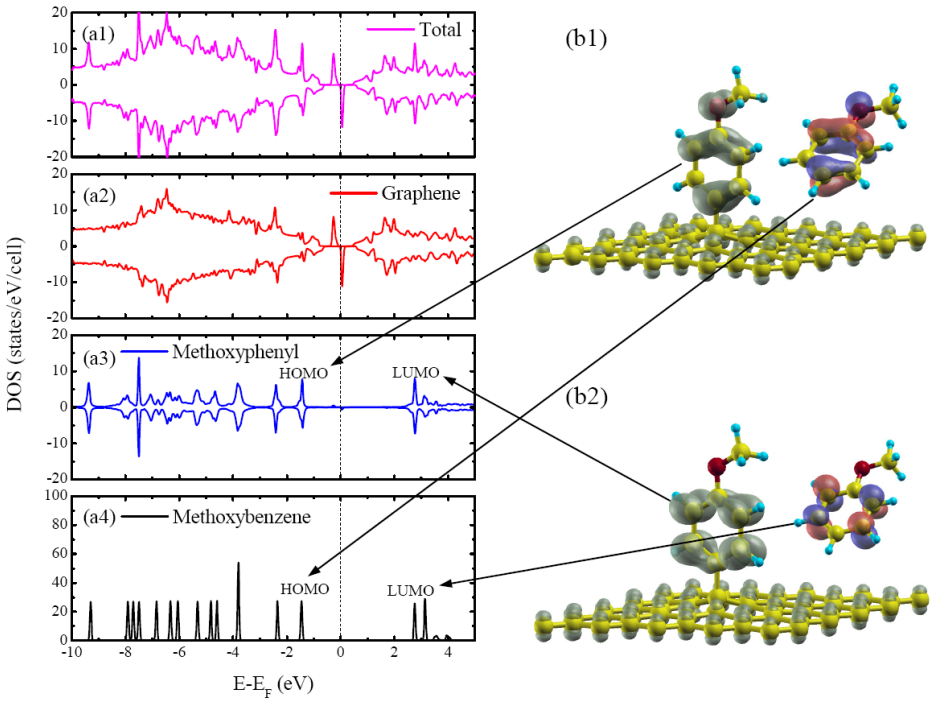


Figure 3.3: (a1) DOS for the full methoxyphenyl/graphene system. The PDOS on (a2) the graphene states and (a3) the methoxyphenyl states. (a4) The DOS of methoxyphenyl in the gas state. (b1 and b2) Illustration of the ILDOS of the HOMO and LUMO of methoxyphenyl/graphene and HOMO–LUMO of free methoxybenzene.

## 3.4 Magnetic Properties

To investigate magnetic properties, in this section we visualize the distribution of spins in the graphene sheet. In Figure 3.4a we plot the spin density of methoxyphenyl/graphene, i.e., $\Delta\rho=\rho_\alpha-\rho_\beta$ where $\rho_\alpha$ and $\rho_\beta$ are the electron densities corresponding to the majority and minority spin populations, respectively. It is found that the induced magnetic moments are mainly localized on the *B*-site carbon atoms closer to the adsorbate. In addition, we note that the spin density is opposite, albeit weaker, at *A*-site carbon atoms: the overall magnetic moment of *B*-site carbon atoms amounts to 1.72 $\mu_B$, while that of *A*-site carbon atoms is −0.79 $\mu_B$, suggesting an anti-ferromagnetic tendency in the graphene sheet. These results are very general and similar to those of the spin polarization of adsorbed H in Figure 3.4b. To exclude finite-size effects in the observed magnetization, we consider a larger 10×10 supercell in Figure 3.4c (taking here adsorbed H for sake of simplicity), where an equivalent spin distribution can be observed. This also highlights that the effect of the adsorbed species on the spin polarization is local, with the magnetic moments gradually decreasing to zero as the distance from the $A_0$-site increases, with atom-projected magnetic moments reported in Figure 3.4d. Note that, although not influencing the spin distribution, the concentration of adsorbates *x* indeed influences the band gap which decreases with an approximate $\sqrt{x}$ dependence as found for C-atom vacancies in graphene as $x \to 0$ [82]. For H/graphene in the 10×10 supercell, we computed an energy difference of 0.06 eV for the two midgap states, and values of 0.51 and 0.53 eV for majority and minority spin band gaps (to be compared to values in Table 3.2). However, a very different spin density distribution is found in the non-covalent adsorption system [83] in which an isolated tetracyano-*p*-quinodimethane molecule is adsorbed on graphene, and the induced

spin density is localized on the molecule, not on graphene. The adsorbed molecule retains a magnetic moment of 0.4 $\mu_B$. We also studied another non-covalent adsorption system namely pyridine physisorbed on graphene [84]. In that work, we observed that the system remains non-magnetic upon molecular adsorption, and the Dirac point of graphene is fixed sat the Fermi level. These discrepancies signal the different character of magnetism between covalent and non-covalent molecular adsorption on graphene. Moreover, we recall that other covalent bound systems such as oxygen on graphene induce a band gap without spin polarization.

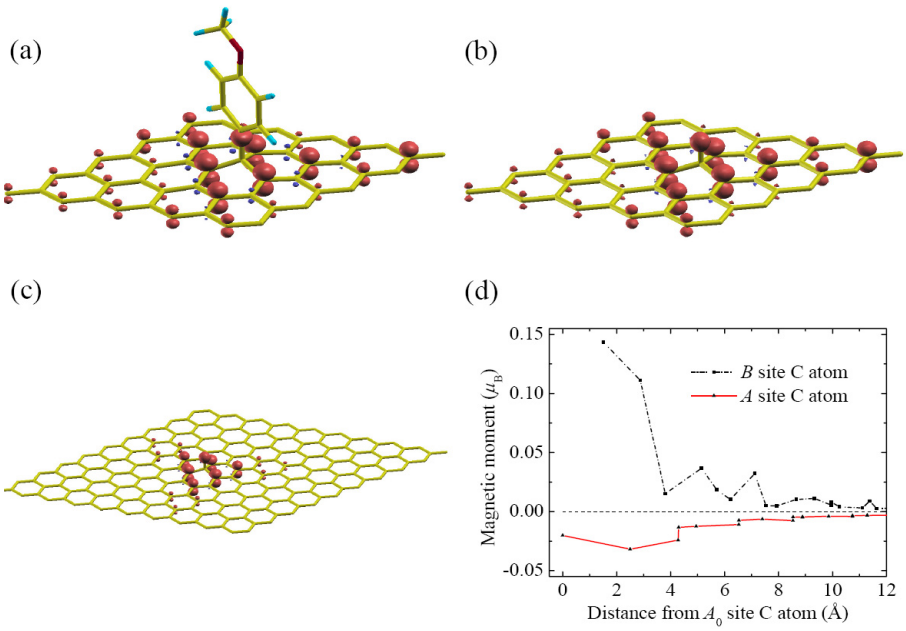


Figure 3.4: Calculated spin density $\Delta\rho$ for (a) methoxyphenyl/graphene and (b) H/graphene in the 5×5 unit cell. (c) and (d) report the spin density and atom-projected magnetic moments as a function of distance from the $A_0$-site for H adsorbed in a 10×10 unit cell

To understand the modification of the electronic structure of pristine graphene which produces magnetism in graphene, we plot the DOS projected on the $p_z$ orbital of the $A_0$ site carbon atom for pristine graphene and methoxyphenyl/graphene systems (see dash-dot and solid lines in Figure 3.5, respectively). As the $A_0$ carbon

atom is bound to the radical, its $p_z$ resonances are shifted to lower energies spanning from −9.0 eV to −4.0 eV. This suggests that one of the $p_z$ orbitals is no longer available to take part in the π band system, leaving the electrons in the *B*-site carbon atoms unpaired, which leads to nonzero magnetism. Differently from magnetism in extended systems, conventionally attributed to d- or f-electrons, in this case 2p states are at the origin of magnetism. In addition, the inst of Figure 3.5 shows the bond charge defined as the electron density of the total system minus that of graphene and that of the adsorbed radical. We can see that the charge is concentrated at the bond between the $A_0$ carbon atom and methoxyphenyl, which verifies the interaction between the radical and graphene has covalent character.

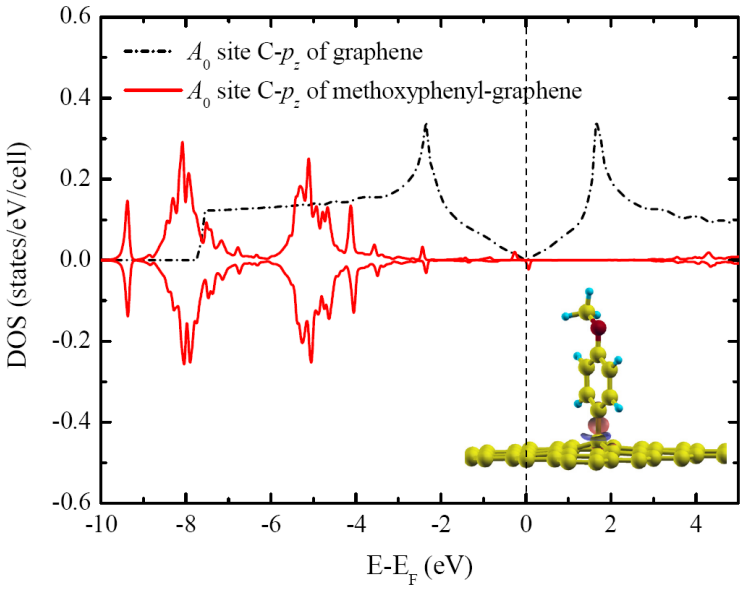


Figure 3.5: PDOS for the $p_z$ orbital on an $A_0$ site carbon atom (dashed line) and on methoxyphenyl/graphene (solid line). The inset shows the induced bonding charge density, showing the isosurface at 0.011 $e^{-}Å^{-3}$. Red: electron accumulation; blue: electron depletion.

Moreover, it has to be mentioned that the lattice distortion shown in Figure 3.1b plays an important role in decoupling the $p_z$ orbital of the $A_0$ carbon atom from the π

system. However, this effect alone is not sufficient to induce the observed magnetism. We artificially displaced the structure of pristine graphene to the adsorbed-induced configuration ($\overline{g}$), and computed the band structure and DOS for this distorted structure. Our calculations show that a gap in graphene (0.14 eV) opens up, but the system remains spin degenerate (see Figure 3.6). Thus only adsorption determines magnetism as explained.

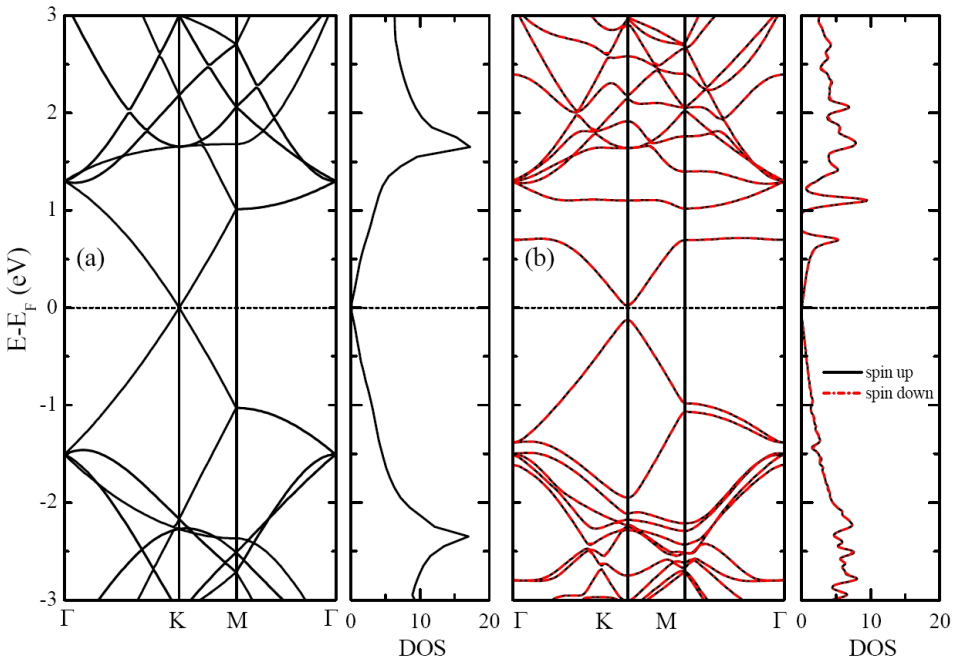


Figure 3.6: Band structure and total DOS for (a) graphene, (b) artificially distorted structure of pristine graphene to the methoxyphenyl adsorbed-induced configuration ($\overline{g}$).

The magnetic properties of multiple adsorbates on carbon allotropes such as nanotubes and graphene have been the subject of several investigations [65,87,88]. From them and our own results for the bench mark system H/graphene, it is generally found that the spin moment induced by the covalent functionalization is independent of the type of adsorbate [87], but depends on the relative adsorbate population bound at $A$ ($N_A$) and $B$ ($N_B$) sublattices, with $|N_A - N_B|\,\mu_B$ giving the total magnetization of

the system [65,88]. As for adsorption energies, once a first species is linked to a C atom, adsorption of a second one preferentially occurs at nearby atoms of the other sublattice, resulting hence in a paramagnetic state [65,87].

## 3.5 Conclusions

In this chapter, we report a computational study of covalent adsorption of aromatic radicals onto graphene. Our results show that the adsorption of an aromatic radical generates two spin-dependent midgap states located around the Fermi energy which induce magnetic moments in graphene. Similarly to the hydrogen/graphene system, the adsorption of an aromatic radical can modify the band of the system and introduce a gap, but this effect is almost independent of the functionalization of the aromatic radical. Due to the interaction between the radical and graphene, we find that the carbon atom on the adsorption site is lifted out of the graphene plane, and its $p_z$ orbital is removed from the $\pi$ system band, leaving the $p_z$ orbitals in the other sublattice unpaired, which leads to nonzero magnetism. It is worth emphasizing that the net result of the radical adsorption is to have nearly the same aromatic species as those in gas phase but anchored on a surface. We also observe that, differently from the case of radicals investigated here, adsorption of an aromatic molecule on graphene is much less effective in modifying graphene properties and certainly does not determine any magnetic properties. The integrity of the structure and a fairly homogeneously distributed magnetism makes graphene functionalized with aromatic radicals attractive for further experimental studies and spintronic applications.

# Chapter 4

# Modeling the Structure and Absorption Spectrum of Dye-Sensitized $TiO_2$

*In this chapter we have presented a comprehensive periodic DFT-TDDFT study of dye/$TiO_2$ models of dye-sensitized solar cells. We observed that finite temperature effects are small but not negligible. In particular, the changes of atomic geometry induced by thermal fluctuations modify the position of the molecular levels around the $TiO_2$ valence band edge.*

## 4.1 Introduction

Dye-sensitized solar cells (DSSCs) represent an effective approach to the direct conversion of sunlight to electrical energy at low cost and with high efficiency [90–92]. DSSCs (12%–15% of efficiency) are constituted by covalent bonding between organic or transition metal-based organometallic dye molecules and a semiconductor, generally a metal oxide such as $TiO_2$ [93]. Among a variety of dyes, catechol adsorbed on $TiO_2$ has received considerable attention in recent years as a prototypical model for DSSCs [14–22]. The acid hydroxy functionalities of catechol can be used to anchor it on a $TiO_2$ surface to ensure strong coupling and device stability. Moreover, the highest occupied molecular orbital (HOMO) energy level of

anchored catechol lies in the band gap of $TiO_2$ [14–17], hence reducing the optical gap and allowing for an efficient dye-substrate electron injection. Another prototypical dye is isonicotinic acid [24–26]. It has a carboxyl functionality which is used to couple with $TiO_2$ surface. Similarly to catechol, the HOMO energy level of adsorbed isonicotinic acid is also within the $TiO_2$ gap. Isonicotinic acid is an electron poor aromatic molecule due to both the substitution of a carbon with the more electronegative nitrogen atom in the aromatic ring and the presence of an electron withdrawing carboxylic substituent, whereas catechol is an electron rich aromatic molecule thanks to the electron donating capabilities of hydroxyl groups. Due to these different electronic properties, the energy level of the lowest unoccupied molecular orbital (LUMO) of the isolated isonicotinic acid is 1.0 eV lower than that of free catechol as the HOMO is taken as a reference (see Figure 4.1).

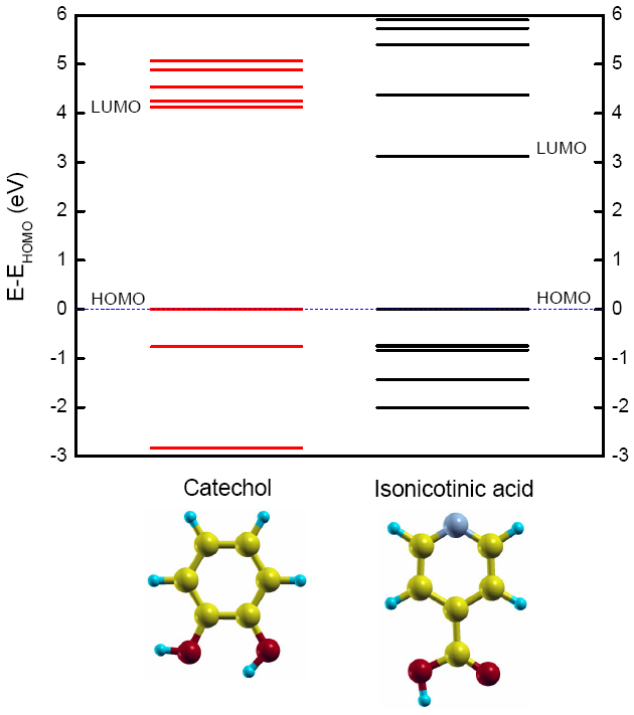


Figure 4.1: Kohn-Sham energies for the optimized structures of the gas phase catechol and isonicotinic acid molecules.

Several recent theoretical studies have utilized density functional theory (DFT) and time dependent DFT (TDDFT) [3] methods to investigate the adsorption of catechol [27–31] and isonicotinic acid [24–26] on $TiO_2$ surfaces. One is a comparative investigation of catechol and isonicotinic acid on $TiO_2$ rutile (110) which was performed by Risplendi et al. [16] using hybrid B3LYP functional calculations. In that study, the geometries, adsorption energies and electronic structures have been investigated extensively; however, the optical spectra has not. Experimentally, catechol-sensitized $TiO_2$ nanoparticles [94] show an absorption band at ~430 nm (~2.88 eV) that is attributed to the excitation from the catechol HOMO orbital in the $TiO_2$ band gap to the conduction band of the nanoparticle [95]. Moreover, since $TiO_2$ nanoparticles generally prefer the metastable anatase phase rather than the thermodynamically stable rutile form [96–100], it is desirable to model the absorption spectrum not only on rutile but also on anatase $TiO_2$, especially on the most frequently exposed anatase (101) surface [101]. In another study, the electronic structures of several dyes including catechol, either free or adsorbed on $TiO_2$ were analyzed by Sánchez-de-Armas et al., and the optical absorption spectra were calculated using TDDFT [31]. The calculated spectra for the free dyes agree well with experiment [102]; however, a small $(TiO_2)_9$ cluster was used to simulate the absorption spectra of dye-sensitized $TiO_2$ [31]. To provide a more reasonable description of the electronic structure and of the optical absorption spectrum, an extended model such as a surface slab is more appropriate. Furthermore, since experimental absorption spectra are generally recorded at room temperature [103], it is important to take into account the effects of thermal fluctuations, usually not included in those theoretical studies [16,31].

In this chapter, we compare the finite temperature optical spectra of catechol and isonicotinic acid on the $TiO_2$ anatase (101) and rutile (110) surfaces. To describe finite temperature effects, we perform first principles molecular dynamics (MD) simulations, select several snapshots along the MD trajectory, and calculate the optical absorption spectrum of each snapshot using TDDFT. In addition, to extend the prototypical dye on $TiO_2$ towards more realistic materials for application, we also studied two more complex species, namely PTCDI and PTCDA adsorbed on the $TiO_2$ rutile (110) surface. Our main concerns are listed as follows. (1) How does the atomic motion affect the electronic structure and the optical absorption spectrum of dye-sensitized $TiO_2$? (2) What is the relationship between the electronic structure and the absorption spectrum? (3) What is the difference between dye-sensitized anatase (101) and rutile (110)? (4) Can adsorption of PTCDI (PTCDA) induce sensitization as we know it occurs with catechol?

## 4.2 Computational details

Our calculations were performed within DFT using the Perdew-Burke-Ernzerholf (PBE) functional [35] and the plane wave pseudopotential scheme. The Quantum-ESPRESSO package [54] was used to perform all calculations. Electron-ion interactions were described by ultrasoft pseudopotentials, and Valence states included the Ti 3s, 3p, 3d and 4s states, the 2s, 2p states of C, O, and N, and H 1s state. Plane-waves basis set cutoffs for the smooth part of the wave functions and the augmented density were 30 and 300 Ry, respectively. K-point sampling was restricted to the Γ point. Optical absorption spectra were computed by TDDFT (see Sec. 2.3 of Chapter 2) using the Liouville-Lanczos approach [45,46]. First principles molecular dynamics (MD) simulations were performed within the Car-Parrinello (CP)

approach [4] (see Sec. 2.4 of Chapter 2). In MD simulations, a time step of 0.194 fs and a fictitious electronic mass of 400 atomic units (amu) were used. The ionic temperatures were controlled by means of a Nosé thermostat [40–42] (see Sec. 2.4 of Chapter 2).

To model the surface, we used the periodically repeated slab geometry [104,105]. The anatase (101) surface was modeled with three layers of oxide (~9.5 Å thick). For the 1×1 surface, a p(3×1) surface supercell was used, with 108 atoms and a surface area of 11.34×10.31 $Å^2$. For the rutile (110) surface, we adopted a four layer slab (~12.5 Å thick), and a p(3×2) surface cell with 144 atoms and a surface area of 8.86×13.03$Å^2$. For PTCDI(PTCDA)/rutile system, a p(6×1) surface supercell was used, with 144 atoms and a surface area of 17.78×6.47 $Å^2$. For both surfaces, the vacuum region between facing slabs was 10 Å wide. To check the adequacy of such a choice, the adsorption of dissociated catechol was calculated using vacuum sizes of 10 Å and 20 Å. A difference in adsorption energy of only 0.01 eV was found between the two cases.

## 4.3 Catechol adsorbed on the anatase (101) surface

In this section we first investigate the adsorption geometry of catechol on anatase (101). We find that dissociative adsorption is highly favored, and that the dissociated catechol is bonded to the surface through the bonds between its two deprotonated OH groups and surface $Ti_{5c}$ atoms (see Figure 4.2a). Two protons resulting from the dissociation are transferred to two neighboring surface $O_{2c}$ sites on the left and right, and the molecular phenyl-like ring is slightly tilted towards the surface. This configuration agrees well with previous experimental and theoretical studies

[27,94,103,106,107]. In order to evaluate the stability of our system we calculated the dye adsorption energy ($E_{ads}$) as follows

$$E_{ads} = E(\text{dye/TiO}_2) - E(\text{TiO}_2) - E(\text{dye}), \quad (4.1)$$

where $E(\text{dye/TiO}_2)$, $E(\text{TiO}_2)$, and $E(\text{dye})$ are the total energies of the chemisorbed system, the clean $TiO_2$ slab, and the isolated molecular dye, respectively. The adsorption energy for catechol/anatase is $E_{ads}$ = −0.72 eV, which is in good agreement with previous DFT calculations (−0.70 eV) [27].

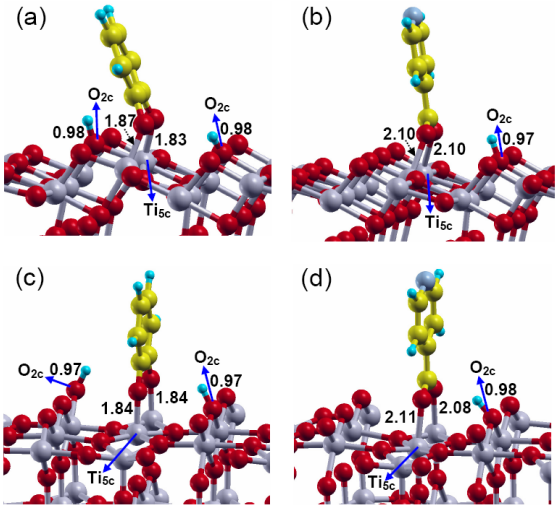


Figure 4.2: Optimized geometries of (a) catechol/anatase $TiO_2$(101), (b) isonicotinic acid/anatase $TiO_2$(101), (c) catechol/rutile $TiO_2$(110), (d) isonicotinic acid/rutile $TiO_2$(110). Relevant bond distances are indicated (Å). O atoms are red, Ti atoms are light gray, C atoms are yellow, and H atoms are blue. This notation is used throughout this chapter.

Then Figure 4.3 shows the time evolution of the bond distances between the two oxygen (O*) atoms of the adsorbed catechol and the surface $Ti_{5c}$ atoms of anatase (101) during a MD simulation at 300 K. Note that the bond distances between O* atoms and the surface $Ti_{5c}$ atoms oscillate around ~ 1.85 Å which is the average of the two $Ti_{5c}$–O* bond lengths (1.87 Å and 1.83 Å shown in Figure 4.2a). Moreover,

the adsorbed catechol swings back and forth around an axis passing along the two O* atoms, thus showing alternate molecular orientations during the simulation.

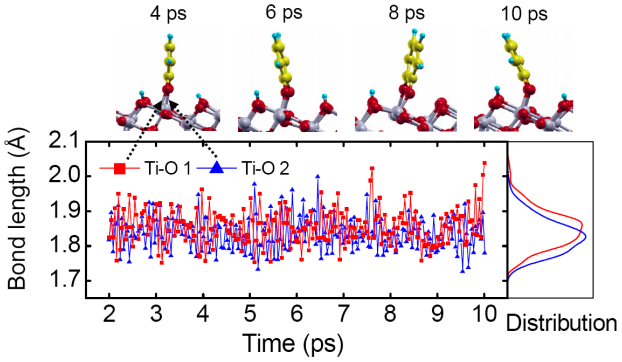


Figure 4.3: Time evolution of the bond distances between the O* atoms of the adsorbed catechol and the surface $Ti_{5c}$ atoms of anatase (101) during a MD simulation at 300 K. Selected snapshots during the simulation are also shown.

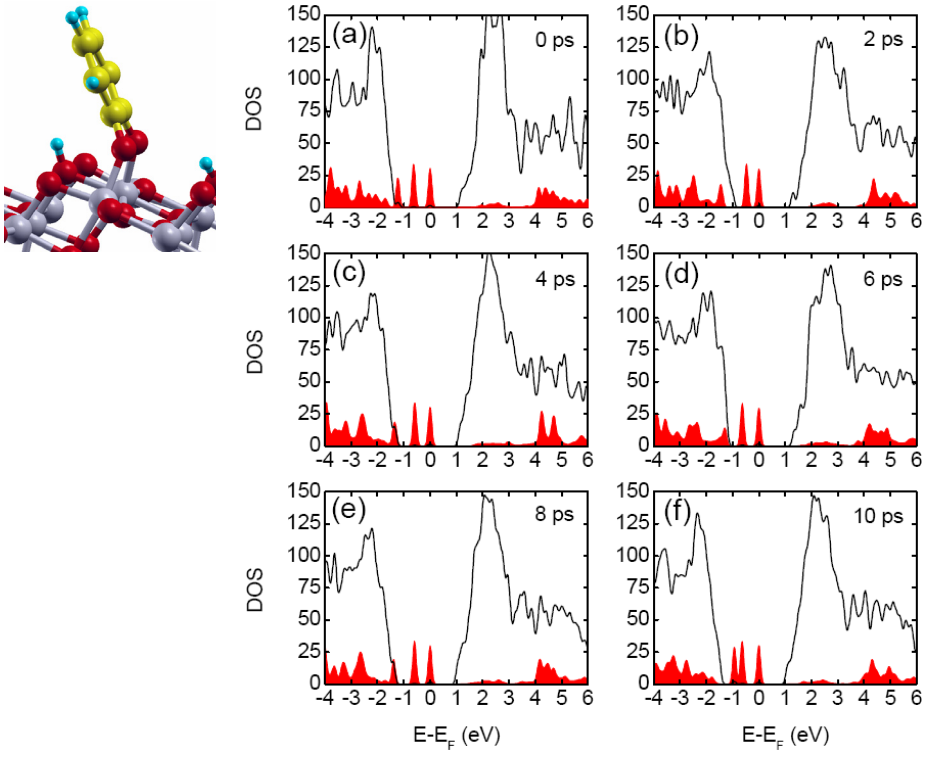


Figure 4.4: Projected density of states (PDOS) for: (a) the ground state structure, and (b–f) selected snapshots of catechol/anatase during a 300 K MD simulation. The solid black curve (red shaded area) is the PDOS for $TiO_2$ (catechol). For better clarity, the PDOS of catechol has been multiplied by 3.

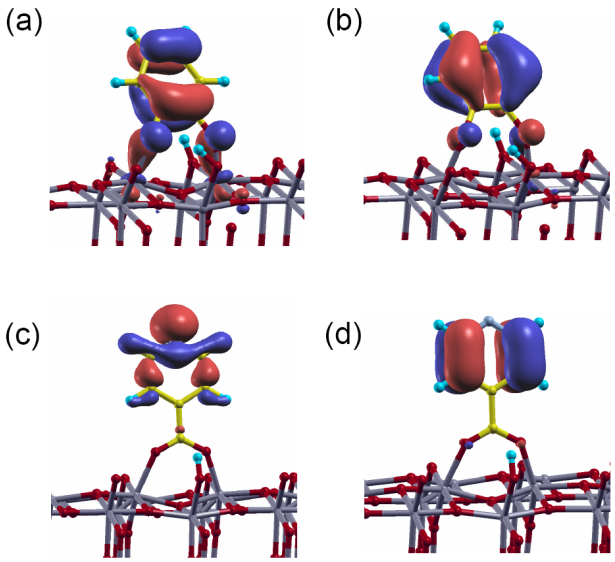


Figure 4.5: Contour plots of: (a) HOMO of catechol/anatase, (b) HOMO−1 of catechol/anatase, (c) HOMO of isonicotinic acid/anatase, (d) HOMO−1 of isonicotinic acid/anatase. The optimized (T= 0K) geometries are used in all cases.

We next analyze the electronic states at the catechol/anatase interface, especially the states with energies close to the $TiO_2$ valence and conduction band edges (VBE and CBE, respectively). We plotted the projected DOS (PDOS) of the optimized structure and selected snapshots along the MD trajectory in Figure 4.4. The snapshots were sampled every 2 ps after the initial thermalization to separate them enough to represent uncorrelated configurations of the dye/$TiO_2$ system. For each structure, we show the PDOS for the $TiO_2$ slab and the adsorbed catechol. In this work we use the notation HOMO, HOMO−1, HOMO−2, etc to represent the states of the adsorbed dye. For the optimized (T = 0 K) structure (Figure 4.4a), the HOMO, HOMO−1, and HOMO−2 energies lie in the band gap of $TiO_2$, and the ground state wavefunction of HOMO and HOMO−1 are plotted in Figure 4.5. As shown in Figure 4.4b–f, the energy levels of the HOMO and HOMO−1 always fluctuate in the band gap of $TiO_2$ during the MD simulation, whereas the energy level of the HOMO−2 is

sometimes above and other times below the $TiO_2$ VBE. Thus a significant effect of thermal fluctuations is to change the position of the HOMO−2 level around the $TiO_2$ VBE. Apart from the gap states, which have clear catechol character, it is also interesting to study the distribution of the other states contributed by catechol, in particular the empty ones. The unoccupied electronic structure of catechol/anatase can be divided into two main categories: $TiO_2$-related states at lower energy, i.e. close to the CBE, and states that are closely related to free-catechol at higher energy. The two sets of unoccupied states occur at about the same energy for the various snapshots, suggesting that thermal fluctuation have less effect on the unoccupied electronic structure of catechol/anatase than on the occupied one.

The calculated optical absorption spectra of catechol/$TiO_2$ are plotted in Figure 6 in which they are compared to those of the clean surface. We observe that the onset of absorption of catechol/anatase in the optimized structure is red-shifted compared to clean $TiO_2$ (see Figure 4.6a1−a2), which is in agreement with experiment [94,103], but the shift is much smaller than the experimental one [94,103]. Moreover, for comparison, the computed absorption spectrum of free catechol is also shown in Figure 4.6a1; a peak appears at ~ 4.5 eV, in good agreement with experiment [102] as well as with previous calculations [31]. From Figure 4.6b–f, we find that the catechol-induced shift of the absorption threshold changes from one snapshot to the other, indicating that thermal fluctuations affect the optical properties to a great degree. For the ground state (Figure 6a) and the snapshot at 10 ps (Figure 4.6f), the HOMO−2 lies in the band gap of $TiO_2$ and has predominant catechol character. In these cases, the hybridization between catechol and $TiO_2$ is relatively weak, and a very small shift in the absorption edge position is obtained (Figure 4.6a,f). By contrast, for the snapshot at 2 ps (Figure 4.6b), 4 ps (Figure 4.6c), 6 ps (Figure 4.6d),

and 8ps (Figure 4.6e), the HOMO−2 is below the $TiO_2$ VBE. As the snapshot displays a HOMO−2 state that lies very close to the VBE of $TiO_2$ (e.g. at 4 ps, 6 ps, and 8 ps), the hybridization between catechol and $TiO_2$ is strong, and correspondingly we obtain a more pronounced red shift in the absorption edge position. However, if the HOMO−2 is well below the $TiO_2$ VBE, as for the snapshot at 2 ps, the energy of the electronic transition to the conduction band is larger, and consequently the red shift of the absorption is smaller.

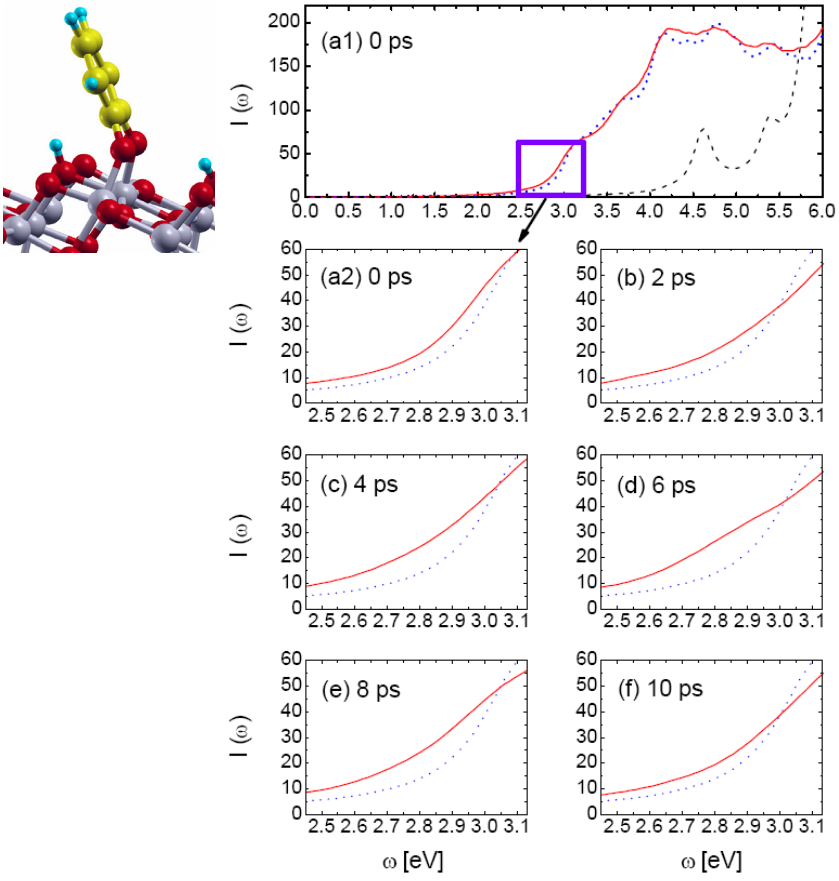


Figure 4.6: Absorption spectrum for: (a1,a2) the ground state, and (b–f) selected snapshots of catechol/anatase along a 300 K MD simulation. The dotted blue (solid red) curve is the absorption spectra for clean anatase $TiO_2$ (catechol/anatase), and the dashed black curve in (a1) is the absorption spectrum of the gas phase catechol molecule.

## 4.4 Isonicotinic acid adsorbed on the anatase (101) surface

Differently from catechol, which prefers to adsorb in dissociated form, for isonicotinic acid/anatase the non-dissociative monodentate configuration is energetically more favorable than the dissociative bidendate one (Figure 4.2b). However, regardless of the more favorable adsorption energy, the molecule in the monodentate configuration desorbed from the surface during the MD simulation. Thus we only discuss the bidentate configuration in this section. In this structure, the dissociated isonicotinic acid is attached to the surface through the oxygens (O*) of the carbonyl group which are bound to two surface $T_{5c}$ atoms. The bond lengths between the surface $Ti_{5c}$ atoms and O* are 2.10 Å (see Figure 4.1b), thus longer than those of catechol/anatase (1.83 and 1.87 Å), while the adsorption energy is −0.60 eV, whose magnitude is 0.12 eV smaller than that of catechol/anatase. Similarly to catechol, the adsorbed isonicotinic acid sways back and forth around an axis along the two O* atoms during MD simulation.

Figure 4.7 shows the calculated PDOS and absorption spectra of selected snapshots along the MD trajectory at T = 300 K. Unlike catechol, in the optimized structure of isonicotinic acid/anatase, only the HOMO and HOMO−1 energies lie in the gap of anatase $TiO_2$, and the main effect of thermal fluctuations is to change the position of the HOMO−1 level around the $TiO_2$ VBE. The ground state wavefunction of HOMO and HOMO−1 are also displayed in Figure 4.5. Additionally, the empty states are quite different from those of catechol. States of adsorbed isonicotinic acid coexist with $TiO_2$-related states at lower energy relative to the CBE, and the LUMO shows a stronger coupling with substrate states, leading to a wide structure in the DOS in the energy range from 2 to 3.5 eV in Figure 4.7a1. As shown in Figure 4.7b1 and especially in Figure 4.7c1, during the MD simulation the DOS contribution by

the LUMO of adsorbed isonicotinic acid is transferred closer to the CBE. This can be compared to the case of catechol (see Figure 4.4), where the position of the LUMO-induced features are fixed at an energy of ~ 3 eV above the CBE, suggesting that thermal fluctuations have a more pronounced effect on the unoccupied electronic structure of isonicotinic acid/anatase than on that of catechol/anatase.

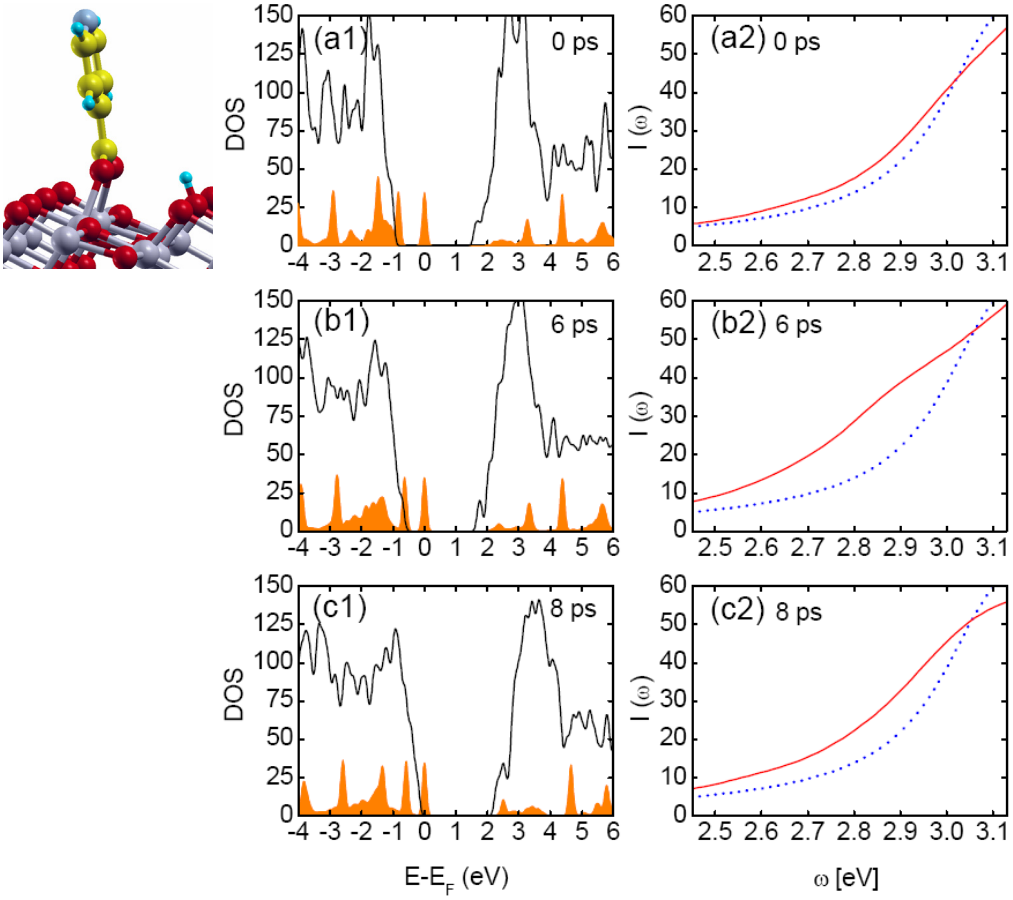


Figure 4.7: PDOS (left) and absorption spectrum (right) for (a) the ground state, and (b) and (c) selected snapshots during a MD simulation of bidentate isonicotinic acid on anatase (101). In the left panels, the solid black curves and orange shaded areas are the PDOS of $TiO_2$ and isonicotinic acid, respectively. For better clarity, the PDOS of isonicotinic acid has been multiplied by 3. In the right panels, the dotted blue and solid red curves are the absorption spectrum of clean anatase $TiO_2$ and isonicotinic acid/anatase, respectively.

From Figure 4.7a2−c2, we observe that similar to catechol, the absorption threshold of isonicotinic acid/$TiO_2$ is red-shifted compared to that of the clean $TiO_2$ surface, and the red shift varies during the MD simulation. For the ground state, the HOMO−1 lies in the gap of $TiO_2$ and has predominant isonicotinic acid character (Figure 4.7a1), thus the hybridization between the adsorbate and $TiO_2$ is relatively weak, and the shift in the absorption edge position is very small (Figure 4.7a2). However, for the snapshot at 6 ps, since the HOMO−1 already overlaps with the $TiO_2$ valence band (Figure 4.7b1), the hybridization between isonicotinic acid and $TiO_2$ is enhanced, leading to a more significant red shift of the absorption spectrum (Figure 4.7b2). But when the HOMO−1 is deeper below the $TiO_2$ VBE (Figure 4.7c1), the energy for the optical electronic transitions increases, hence a less effective sensitization results are obtained (Figure 4.7c2).

## 4.5 Rutile (110) and comparison to anatase (101)

For both catechol and isonicotinic acid on the rutile (110) surface, dissociative adsorption is highly favored, resulting in the bidentate configurations shown in Figure 4.2c,d. As on anatase (101), the dissociated catechol (isonicotinic acid) is attached to rutile (110) by the bond between the oxygen (O*) of its hydroxyl groups (carbonyl group) and two $Ti_{5c}$ atoms, but unlike on anatase (101) in this case the adsorbate is almost perpendicular to the surface. The $Ti_{5c}$–O* bond lengths are similar to those of catechol (isonicotinic acid)/anatase. However, among the four geometries in Figure 4.2, we obtain the smallest magnitude of the adsorption energy (−0.45 eV) for catechol/rutile, and the largest one (−0.82 eV) for isonicotinic acid/rutile. During the MD simulation, the adsorbed dye also sways with respect to an axis along the two O* atoms and shows alternate molecular orientations.

The calculated PDOS and absorption spectra for the ground state structures of catechol and isonicotinic acid on rutile are plotted in Figure 4.8 and Figure 4.9, respectively, whereas analogous results for various snapshots along the corresponding MD simulations are shown in Figure 4.10–Figure 4.13. In comparison to anatase (101) (Figure 4.8b,d and Figure 4.9b,d), a shoulder in the PDOS appears near the $TiO_2$ VBE (see Figure 4.8a,c), and the absorption threshold occurs at lower energy than on anatase (see Figure 4.9a,c). For catechol/rutile, the onset of the absorption shows a very small red-shift compared to that of the clean rutile surface (Figure 4.9a and Figure 4.11), while the absorption of isonicotinic acid/rutile is even slightly blue-shifted in comparison to that of clean rutile $TiO_2$ (Figure 4.9c and Figure 4.13), which is opposite to what found for isonicotinic acid/anatase (Figure 4.9d). To make closer contact with experiments, in Figure 4.9a–d we also plot the dye/$TiO_2$ absorption spectra obtained from the average over the different snapshots of each simulation. It appears that thermal fluctuations tend to enhance the absorption in the low energy tail with a more pronounced effect on anatase than on rutile (see the insets of Figure 4.9a–d).

Furthermore, to summarize our results and compare the alignments of the molecular levels with the $TiO_2$ band edges, in Table 4.1 we list the energy differences between HOMO and HOMO−1 energies in the gap and the VBE of the clean $TiO_2$ surface. For both dyes, the molecular states of dye/rutile are closer to the VBE than those of dye/anatase. This is consistent with the relative alignments of the rutile and anatase band edges proposed by Scanlon et al [108]. On the other hand, comparing different dyes, the HOMO and HOMO−1 states of adsorbed isonicotinic acid are closer to the VBE than those of catechol. This is probably related to the pinning of catechol's HOMO−2 to the VBE, which is observed on both the anatase

(101) and rutile (110) surfaces. We further comment that there is no clear correlation between these energy level alignments and the adsorption energies in Table 4.1.

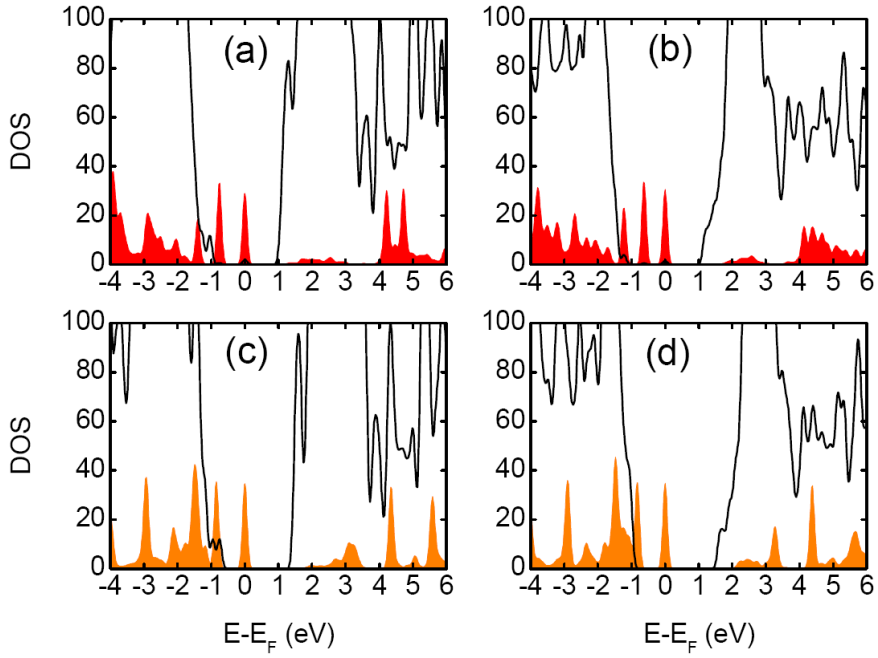


Figure 4.8: PDOS of (a) catechol/rutile, (b) catechol/anatase, (c) isonicotinic acid/rutile, (d) isonicotinic acid/anatase. The solid black curves are the PDOS of $TiO_2$, and the red (orange) shaded areas are the PDOS for catechol (isonicotinic acid). The PDOS of catechol and isonicotinic acid have been multiplied by 3.

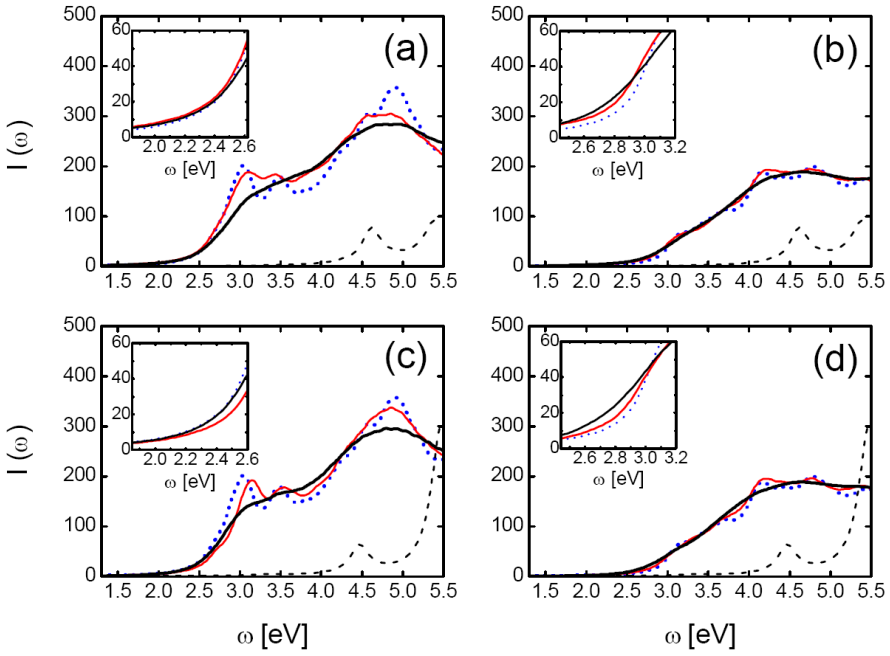


Figure 4.9: Absorption spectra of (a) catechol/rutile, (b) catechol/anatase, (c) isonicotinic acid/rutile, (d) isonicotinic acid/anatase. The dotted blue (solid red) curves are the absorption spectra for the ground state (T = 0 K) of clean $TiO_2$ (dye/$TiO_2$), while the thick solid black curves are the absorption spectra at T = 300 K, obtained from the average over the various snapshots of each dye/$TiO_2$ MD simulation. The dashed black curves are the absorption spectra of the free catechol (a,b) and isonicotinic acid (c,d) molecules. The insets of (a), (b), (c), and (d) show the corresponding absorption spectra in the low energy tail.

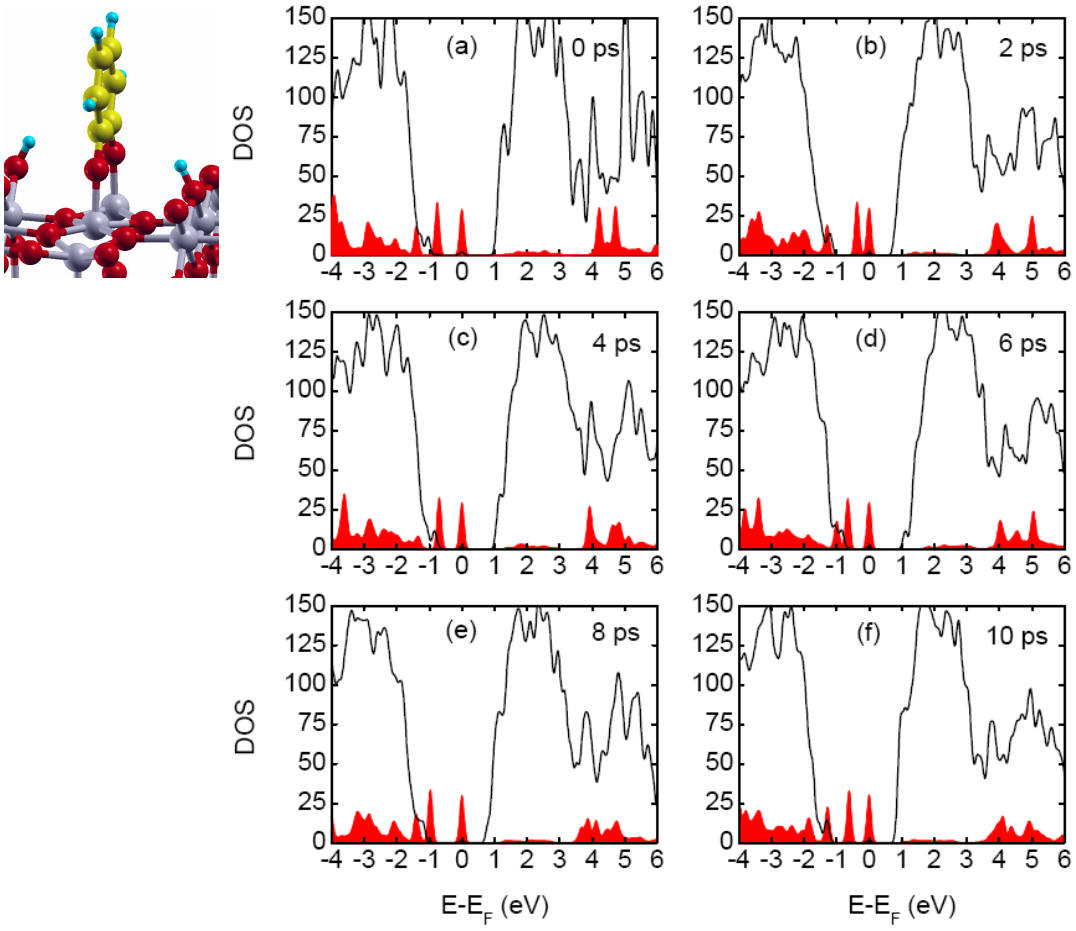


Figure 4.10: Projected density of states (PDOS) for: (a) the ground state structure, and (b–f) selected snapshots of catechol/rutile during a 300 K MD simulation. The solid black curve (red shaded area) is the PDOS for $TiO_2$ (catechol). For better clarity, the PDOS of catechol has been multiplied by 3.

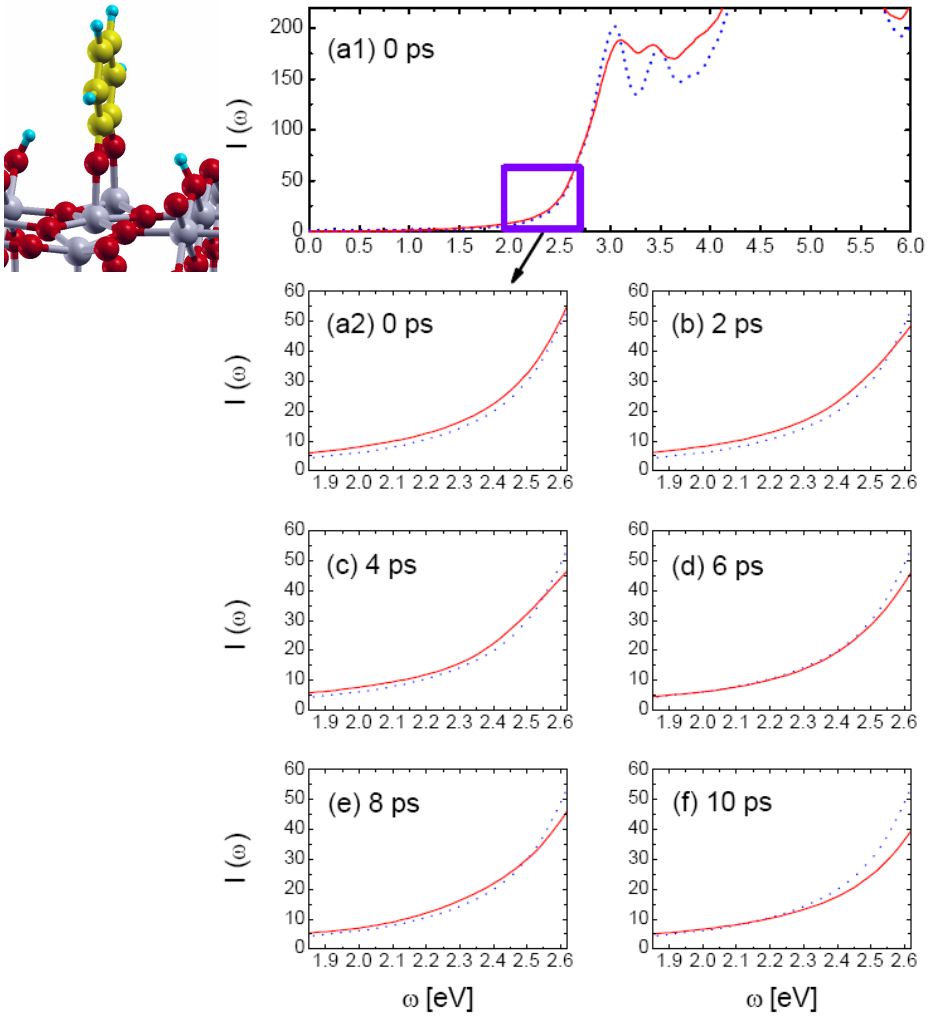


Figure 4.11: Absorption spectrum for: (a1,a2) the ground state, and (b–f) selected snapshots of catechol/rutile along a 300 K MD simulation. The dotted blue (solid red) curve is the absorption spectra for clean rutile $TiO_2$ (catechol/rutile).

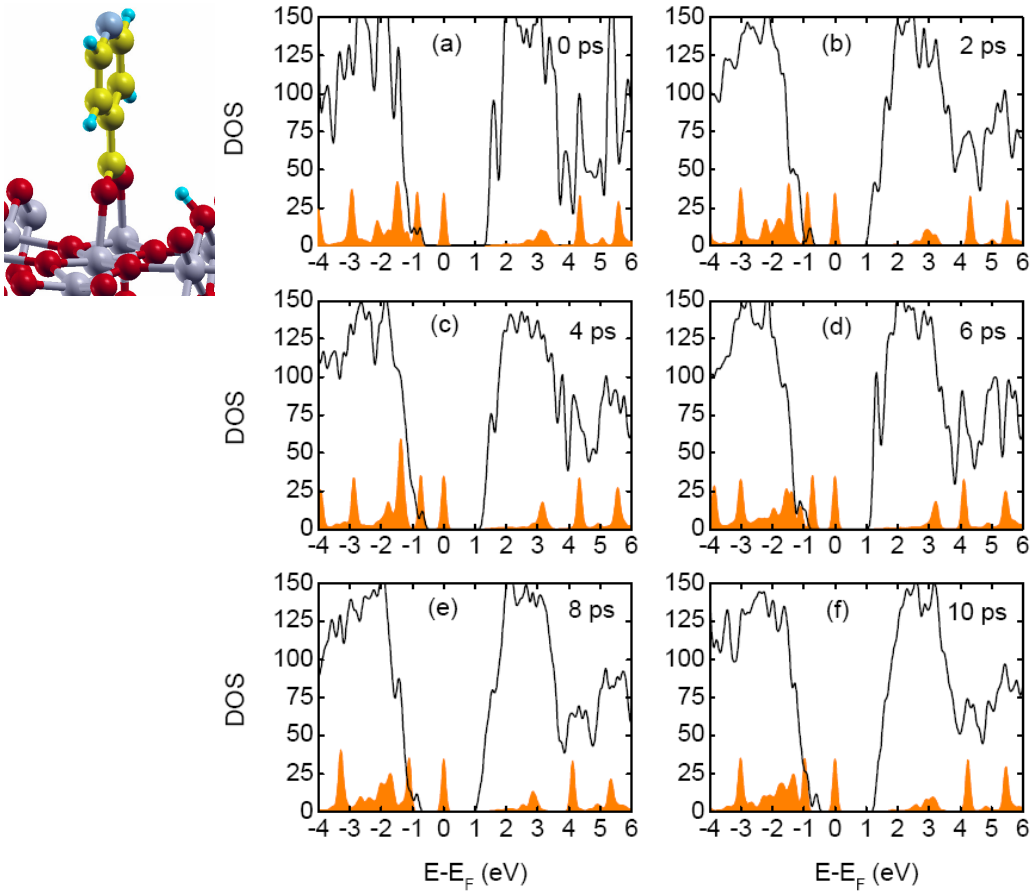


Figure 4.12: Projected density of states (PDOS) for: (a) the ground state structure, and (b–f) selected snapshots of isonicotinic acid/rutile during a 300 K MD simulation. The solid black curve (orange shaded area) is the PDOS for $TiO_2$ (isonicotinic acid). For better clarity, the PDOS of isonicotinic acid has been multiplied by 3.

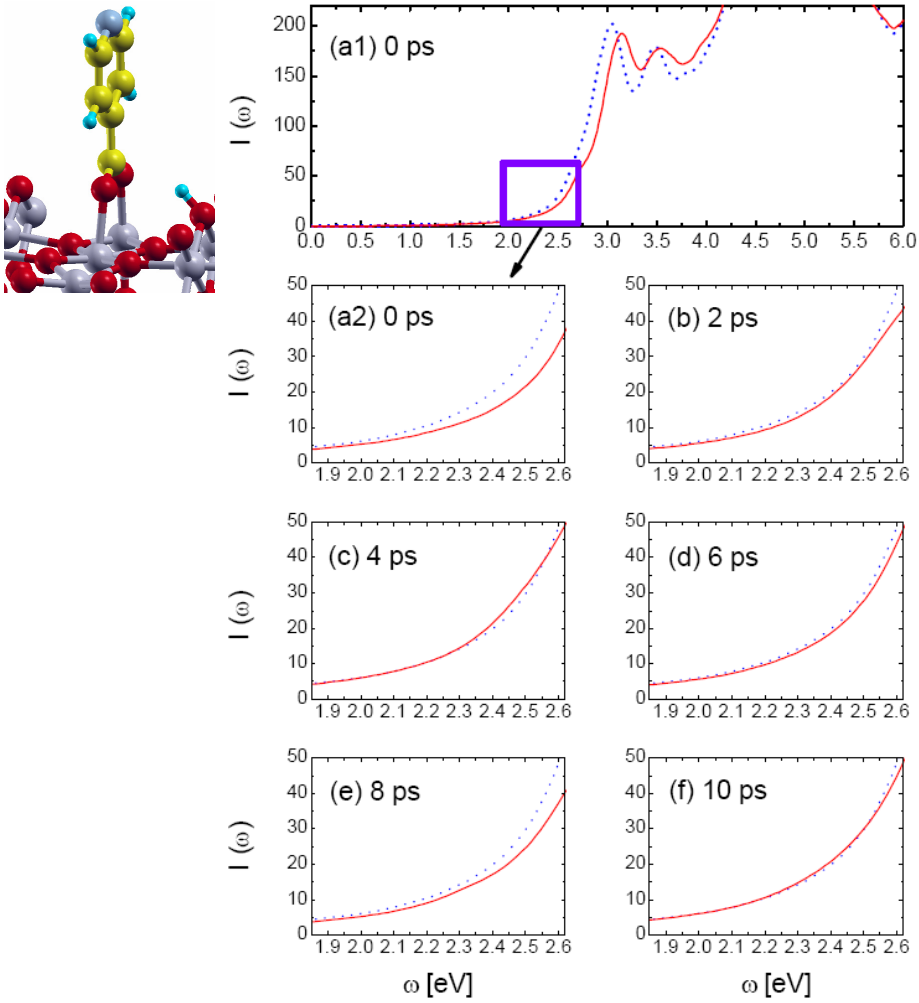


Figure 4.13 Absorption spectrum for: (a1,a2) the ground state, and (b–f) selected snapshots of isonicotinic acid/rutile along a 300 K MD simulation. The dotted blue (solid red) curve is the absorption spectra for clean rutile $TiO_2$ (isonicotinic acid/rutile).

Table 4.1: Energy differences between mid-gap states (HOMO and HOMO−1) and valence band edge (VBE) ($E_{HOMO}-E_{VBE}$, $E_{HOMO-1}-E_{VBE}$, in eV), and adsorption energy $E_{ads}$ (eV) for the configurations given in Figure 4.2. We determined the energy of the VBE (EVBE) on the clean surfaces, using the O 2s level as a common reference for the clean and sensitized

| configurations | $E_{HOMO}-E_{VBE}$ | $E_{HOMO-1}-E_{VBE}$ | $E_{ads}$ |
|---|---|---|---|
| catechol/anatase | 1.48 | 0.85 | −0.72 |
| isonicotinic acid/anatase | 1.04 | 0.21 | −0.60 |
| catechol/rutile | 1.10 | 0.34 | −0.45 |
| isonicotinic acid/rutile | 0.78 | 0.03 | −0.82 |

## 4.6 Benchmarking with previous TDDFT and many body studies

Considering a great amount of research reported in recent years, it is interesting to compare our results to those of previous studies [16,17,31]. Risplendi et al. [16] investigated different adsorption modes of catechol and isonicotinic acid onto the rutile $TiO_2$ (110) surface within a hybrid DFT framework. For both adsorbates, they found that a dissociated bidentate configuration is favored, that in the most stable configuration, the HOMO of both adsorbates lies in the energy gap of $TiO_2$, and the HOMO of adsorbed catechol is a delocalized $\pi$ orbital, while the HOMO of isonicotinic acid corresponds to a $\sigma$ orbital. All these findings are in agreement with our results. Sánchez-de-Armas et al. reported a DFT-TDDFT study of the electronic structure and the optical response of various dyes, free and bound to a $(TiO_2)_9$ cluster [31]. In that study, the calculated spectrum of free catechol agrees well with ours. For

catechol adsorbed on the $(TiO_2)_9$ cluster, however, they obtained a wide absorption band at lower energy, which is not present in the experimental spectrum. Additionally, those authors did not report the spectrum of the bare $(TiO_2)_9$ cluster, so that it is not possible to infer the effect of the sensitization due to the dye adsorption.

A limitation of our approach is the use of PBE Kohn-Sham (KS) eigenvalues to evaluate the alignment of the molecular levels relative to the $TiO_2$ band edges. The use of PBE may also explain why the effect of $TiO_2$ sensitization (especially the catechol induced red-shift of the anatase absorption) appears to be underestimated with respect to the experiment [94,103]. However, the limitations of the Kohn-Sham description of the DOS do not shake the conclusion that the sensitization is improved by enhancing the hybridization between the dye and $TiO_2$ states, as observed during our molecular dynamics simulations. In our case, the alignment of the hybridizing orbital of catechol (HOMO−2) with the $TiO_2$ VBE depends on the geometry, and the highest orbitals (HOMO−1 and HOMO) experience the same dependence. In this respect, we note that a recent $G_0W_0$ calculation [17] for catechol on rutile (110) shows that the HOMO−1 energy of the adsorbed catechol overlaps the valence band and thus its energy is lower than in our results (the HOMO is still found to be at higher energy than the VBE in Ref.17). Our analysis of the molecular dynamics induced hybridization and its implication for the sensitization could be applied to such state, given its similar energy dependence on thermal fluctuations.

## 4.7 PTCDI (PTCDA) adsorbed on rutile (110)

In this section, we start with a discussion of the absorption spectrum of PTCDI and PTCDA in gas phase. The spectrum of PTCDI calculated by adiabatic PBE approximation (APBE) is given in Figure 4.14a with red line, while that by

independent particle random phase approximation (IP-RPA) is shown with a blue line. Note that the first feature of spectrum by APBE is in good agreement with experimental result. Furthermore, the energy position of the first feature of spectrum by IP-RPA equals to the energy difference between HOMO and LUMO, which suggests that the first feature is due to the transition from HOMO to LUMO. However, the features below the first one in the experimental spectrum are due to the vibronic effects which are not considered in our simulation. The spectra of PTCDA (Figure 4.14b) are similar to that of PTCDI.

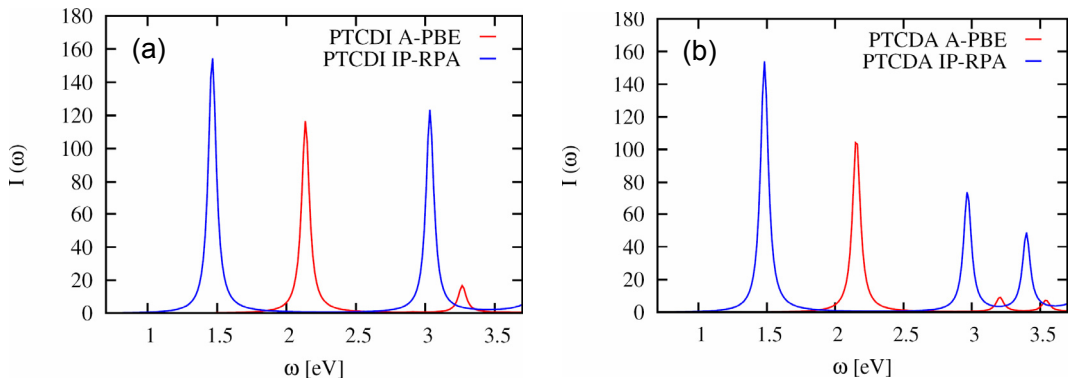


Figure 4.14: Absorption spectrum for (a) PTCDI (b) PTCDA in gas phase.

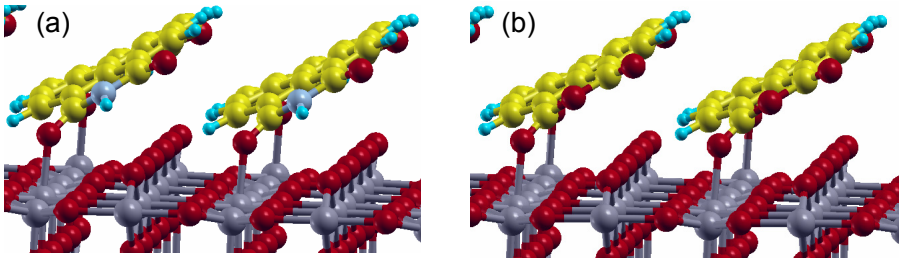


Figure 4.15: Optimized geometries of (a) PTCDI/rutile $TiO_2$ (110), (b) PTCDA/rutile $TiO_2$ (110).

Our adsorption geometry studies of PTCDI and PTCDA on rutile (110) show that two oxygen (O*) atoms of the molecule attach to $Ti_{5c}$ ones of the surface in a roof

tile configuration. The optimized structures are shown in Figure 4.15. The two $Ti_{5c}$–O* bond lengths of PTCDI/rutile are 2.15 Å, which is shorter than those of PTCDA/rutile (2.23 Å). To check the stability of these systems, we computed the adsorption energy ($E_{ads}$). The adsorption energy for PTCDI/rutile is $E_{ads} = -3.35$ eV, whose magnitude is 0.42 eV larger than that of PTCDA/rutile (−2.93 eV). In comparison to the case of catechol/rutile, the adsorption energy of PTCDI (PTCDA)/rutile is much larger than that of catechol/rutile.

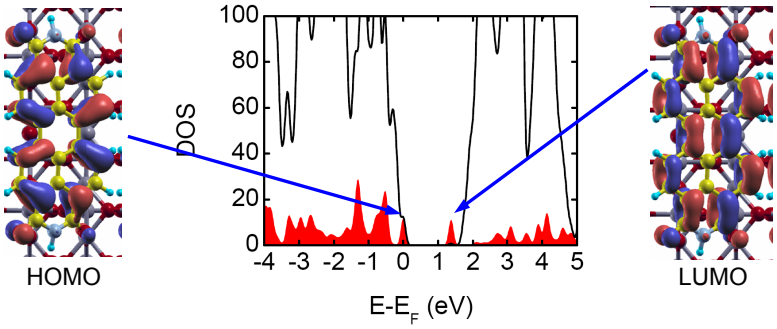


Figure 4.16: Projected DOS for PTCDI/rutile $TiO_2$ (110) as well as the wavefunction for HOMO and LUMO.

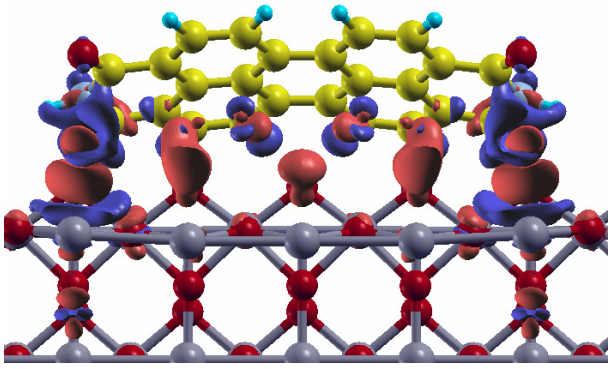

Figure 4.17: Bonding charge density for PTCDI/rutile $TiO_2$ (110). Red: electron accumulation; blue: electron depletion.

Due to the similarity between PTCDI and PTCDA, we focus on PTCDI/$TiO_2$ in the following discussion. Figure 4.16 shows the projected density of states (PDOS)

and the wavefunctions of HOMO and LUMO for PTCDI/rutile system. Differently with the catechol/rutile, the HOMO energy level of anchored PTCDI is very close to the valence band edge (VBE) of $TiO_2$, whereas the LUMO energy level lies in the band gap of $TiO_2$. From the wavefunctions shown in Figure 4.16, we note that the HOMO and LUMO are almost completely localized on the adsorbed PTCDI. We further calculate the bond charge (defined as the electron density of the total system minus that of $TiO_2$ slab and that the adsorbed dye), and the result is shown in Figure 4.17. That charge is concentrated at the bond between the O* of adsorbed PTCDI and $Ti_{5c}$ ones of the surface, which suggests that the interaction between the PTCDI and $TiO_2$ has covalent character.

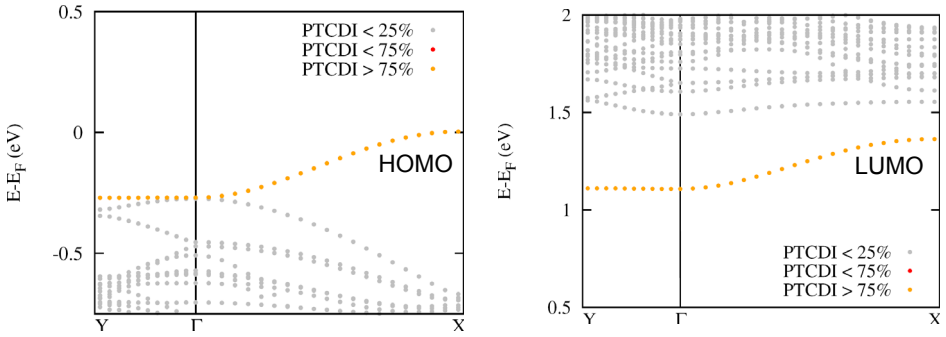


Figure 4.18: Projected band structure for PTCDI/rutile $TiO_2$ (110). The color point gives the molecular weight on given eigenfunction.

Moreover, we compute the projected band structure of PTCDI/rutile which is shown in Figure 4.18. The different color dots indicate the molecular weight on the given eigenfunction. Here, the orange point (PTCDI>75%) represents molecule, and the grey point (PTCDI<25%) denotes substrate. We observe that at different ***k*** points the HOMO and LUMO states are always dominated by PTCDI ones (see Figure 4a–b). Additionally, along Y direction, the coupling between molecules is weak because the molecules are far from each other (see Figure 4.15), thus almost no

dispersion is found. On the other hand, along X direction (see Figure 4.15), due to the $\pi$–$\pi$ interaction, the coupling between molecules is stronger, leading to a pronounced dispersion.

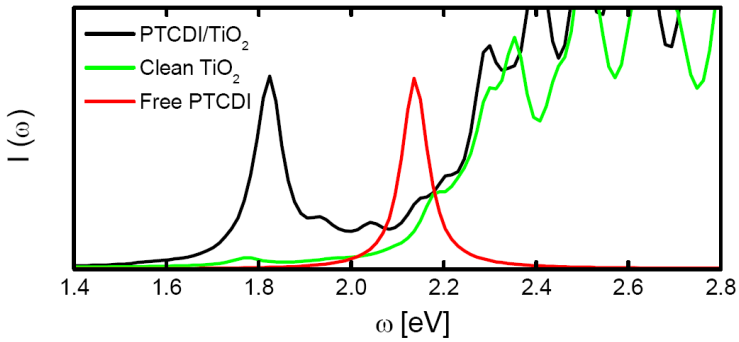


Figure 4.19: Absorption spectrum for PTCDI/rutile $TiO_2$ (110).

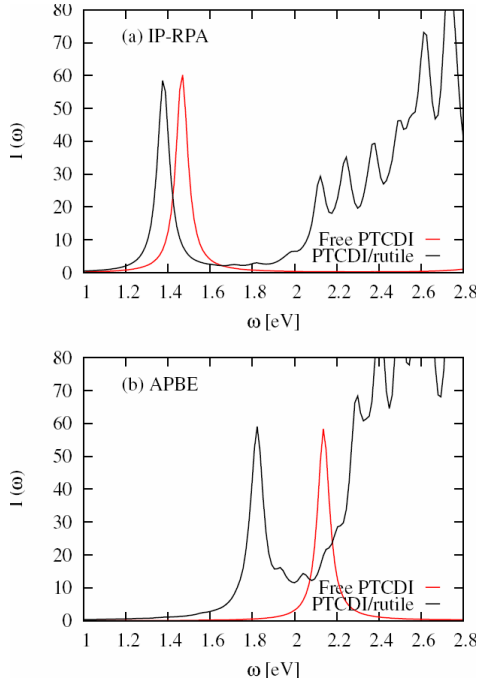


Figure 4.20: Absorption spectra computed by (a) IP-RPA and (b) APBE.

The calculated optical absorption spectra of dye/rutile are shown in Figure 4.19, where they are compared to those of clean surface and isolated dyes. Compared to

catechol/rutile, these molecules induce a more pronounced sensitization effect with a substantial red-shift of the first peak of the dye/$TiO_2$ absorption relative the free dye. To understand this red-shift, we redo the calculation of spectrum at IP-RPA level, and the computed spectrum is compared with APBE result in Figure 4.20. From Figure 4.20a, we note that the magnitude of red-shift at IP-RPA is 0.1 eV which equal to the HOMO-LUMO gap difference between isolated dye and dye/rutile system. This suggests that the red-shift is due to the HOMO-LUMO gap reduction at IP-RPA level. Thus one could conclude that the molecule induced sensitization origins from the HOMO-LUMO gap reduction and APBE effect.

## 4.8 Conclusions

In this chapter, we studied the adsorption of catechol and isonicotinic acid on the $TiO_2$ anatase (101) and rutile (110) surfaces by means of first-principles molecular dynamics simulations and time-dependent density functional calculations. Our results show that finite temperature effects are small but not negligible for catechol- and isonicotinic acid-sensitized $TiO_2$ system. In particular the changes of atomic geometry induced by thermal fluctuations modify the position of the molecular levels around the $TiO_2$ valence band edge. For the anatase (101) surface, the alignment of the molecular levels with the $TiO_2$ valence band edge has a significant effect on the absorption spectrum. For rutile (110), instead, the adsorption of catechol and isonicotinic acid induces only a minor sensitization. The sensitization of anatase (101) by catechol and isonicotinic acid can be enhanced by increasing the hybridization between the adsorbed dye and $TiO_2$ states. In comparison to catchol and isonicotinic acid, PTCDI and PTCDA determine a more pronounced sensitization effect with a

substantial red-shift of the first peak of the dye/$TiO_2$ absorption relative to the free dye.

# Chapter 5

# Corannulene on Ag(111)

*In this chapter the unoccupied molecular orbitals of corannulene were investigated by experimental and simulated electron core-level spectroscopy. From our calculation of the intrinsic dichroism resulting from the corannulene curvature and polarization dependent NEXAFS measurement of the unoccupied molecular orbitals, the tilting of molecules from the surface will be discussed in detail.*

## 5.1 Introduction

The curved poly- and heteroaromatic molecules attract interest due to the possibility that heteromolecular convex-to-concave facing shapes [109–111] may improve the coupling between $\pi$–electron clouds, hence the intermolecular electron transport, like reported for a few shape-matching heteromolecular systems [112,113]. The interaction of open geodesic polyarenes with substrates may further enhance and stabilize the convex-to-concave heteromolecular coupling [110]. On the other hand, buckybowl aromatic molecules have been shown to transfer chiral enantioselectivity to an albeit achiral surface [114]. In this aspect, corannulene ($C_{20}H_{10}$), the simplest bucky-bowl fullerene fragment, displays the most intriguing behavior when deposited on crystalline surfaces due to its $C_{5v}$ symmetry that can not match any crystal symmetry.

Corannulene can be regard as a slice of the top 20 carbon atoms of $C_{60}$ fullerene, with a central pentagon ring and the 10 peripheral carbon atoms capped with hydrogen atoms [32,33]. From the electronic point of view, the corannulene bond lengths suggest significant delocalization in the system. For instance, acceptance of four electrons makes corannulene more electron-rich per carbon atom than the commonly used electron acceptor $C_{60}$. A practical synthetic route rendered corannulene to be available for comprehensive studies, which has also proposed its utilization in a wide range of applications [34]. Indeed, corannulene has been independently reported to be an excellent material for electron conductivity purposes [115–119], and its electron-accepting properties can be tuned through functionalization of the $C_{20}H_{10}$ bowl, eventually favoring a bow-in-bowl coupling which facilitates intermolecular electron hopping [120].

Recently, a few scanning tunneling microscopy (STM) and photoemission experiments have been performed to study corannulene adsorbed on the Cu(111) and Cu(110) surfaces [110,125,126]. A general trend can be rationalized, where molecules adsorb with their concavity pointing upward in order to maximize the overlap between the $\pi^*$ system of one of the aromatic rings with the charge density of the metal substrate. The symmetry of the substrate ultimately dictates the specific adsorption geometry, much similarly to the case of $C_{60}$. On the Cu(111) close compact surface, corannulene faces the substrate with an hexagon, hence its normal axis is tilted with respect to the surface, and it forms a hexagonal 2D lattice [126]. On the rectangular Cu(110) unit cell, 2D ordered domains are formed by adsorption on a carbon-carbon bond at the rim of the central pentagon, again yielding a slightly tilted geometry [110,125]. Direct adsorption on the pentagon ring has been only observed for isolated molecules or in disordered areas [126]. In fact, the mismatch

between the $C_{5v}$ molecular symmetry and whatever crystalline substrate is always relieved by molecular tilting in 2D ordered phases [127]. Moreover, a periodic two-dimensional supramolecular surface exhibits a restricted set of lattice symmetries, and thus not all molecular point group symmetries can be maintained exclusively in a tilting array. The structure of the monolayer, in turn, affects the electronic and optical properties of thin films [128–135].

Additionally, Core-level spectroscopy and in particular X-ray absorption has proved as a useful tool to analyze the unoccupied states of adsorbed molecules. The near-edge x-ray absorption fine structure spectroscopy (NEXAFS) analysis of corannulene may also serve as a tool to understand the spectra of fullerene isomers, like $C_{60}$[136] and $C_{82}$[137] where atomic contributions in terms of local C environments was presented. Unoccupied states of corannulene have also been recently studied by optical absorption within a theoretical GW+BSE framework.

Having the possibility to rationalize the photoemission and NEXAFS spectra of molecule adsorbed on surfaces will be extremely important to comprehend the interactions, the atoms involved in the bonding and interplay of different mechanisms required in the formation of the electronic structure and the behavior of the system. In this thesis, I have investigated the occupied and unoccupied density of state of corannulene by first principles simulations based on density functional theory (DFT) combined the experimental analysis by Dr. Andrea Goldoni using photoemission and NEXAFS. By adsorbing one monolayer of molecules on Ag(111) we can distinguish molecular states with and symmetry thanks to a small title angle. Full understanding of the unoccupied molecular orbitals is provided by our theoretical analysis and the corresponding simulations of XPS and NEXAFS spectra for isolated molecules.

## 5.2 Experimental Interface Morphology

The experiments were carried out by Dr. Andrea Goldoni and his group at Elettra Sincrotrone, Trieste, Italy. The Ag(111) surface was cleaned by repeated Ar+ sputtering at 1.5 keV at room temperature for 30 minutes, followed by thermal annealing up to 700 K. Surface cleanness before deposition has been checked by means of X-ray photoelectron spectroscopy (XPS) and high-energy electron diffraction.

C1s has been measured at $h\nu$ = 515 eV with an overall resolution of 300 meV, while the valence band photoemission has been taken at $h\nu$ = 140 eV with and energy resolution of 100 meV. Near-edge X-ray absorption fine structure (NEXAFS) was taken in the energy reange 280–320eV with a resolution of 80 meV.

Corannulene molecules have been evaporated from a well-degassed boron nitrate crucible at about 410 K. The rate has been calibrated by means of a quartz microbalance and verified by XPS. At substrate room temperature, corrannulene forms a saturation layer on the Ag(111) surface at a thickness of ~2.5 Å, which we define as 1 monolayer (ML) coverage. At the low deposition rates considered here, 0.1–0.2 Å /min, we have not observed the condensation of next layer molecules. This points either to extremely high mobility of molecules, hence forming widely spaced 3D clusters which escape detection by surface sensitive XPS technique, or to a very small sticking coefficient due to the mismatch between the first layer molecular orientation and that of the molecular crystal planes in the natural direction of growth. Such a behavior has been reported also for other polyconjugated hydrocarbons of similar size, e.g. perylene on $TiO_2$ (110) [139].

## 5.3 Computational details

Our calculations are performed within DFT under the generalized gradient approximation of Perdew Burke Ernzerhof (PBE) [35]. Pseudopotentials and plane-wave basis sets were used to model isolated molecules by taking sufficiently large periodically reported supercells. All calculations are carried out with the Quantum-ESPRESSO package [54]. We previously found that an orthorhombic supercell with 11 Å of vacuum space between replicated species is sufficient to converge the results [139], thus it was used to perform geometry optimizations for the neutral molecules with norm conserving pseudopotentials and a plane-wave cutoff of 90 Ry. The dependence on the initial state was evaluated by determining the core level shifts (CLS) between inequivalent carbon atoms. Following Ref. [140], the CLS was determined by the total energy differences between calculations with a C pseudopotential generated with a 1s full core hole (FCH) at the various sites. To determine NEXAFS, we have taken the transition-potential (TP-DFT) approach proposed by Triguero et al [50,141] and introduced in Chapter 2. In this method, one performs a self-consistent calculation of the effective Kohn-Sham potential with half-core-hole (HCH) occupation of the initial-state 1s orbital and typically neglects the fractional occupation of the final state (hence the system has charge of +0.5e). In this work, a HCH pseudopotential was used, and the explicit calculation of the unoccupied orbitals was avoided following a Lanczos techniques as implemented in the xspectra code [51] of Quantum-Espresso. This setup allows us to estimate efficiently the spectrum as well as in the continuum energy region, where details of transition to $\sigma^*$ states can be used to determine the azimuthal orientation [47,139] of the molecules and has been validated by the comparison to experiments in a variety of cases.[52,53,139] We also performed explicit calculation of few unoccupied states

to identify the molecular orbitals involved in specific transitions at the lower energies, and these orbitals were eventually projected onto the ones of corannulene in the ground state to highlight the modification of the electronic structure by the core hole.

A ball-stick model of corannulene is shown in Figure 5.1, where the C–C bond lengths are reported. These are in excellent agreement to previous studies [142,143]. The molecule has three inequivalent C species, which we label C1 (5×), C2 (5×), and C3 (10×) starting from the center. These inequivalent C species will be considered as initial state for the 1s core-level excitation.

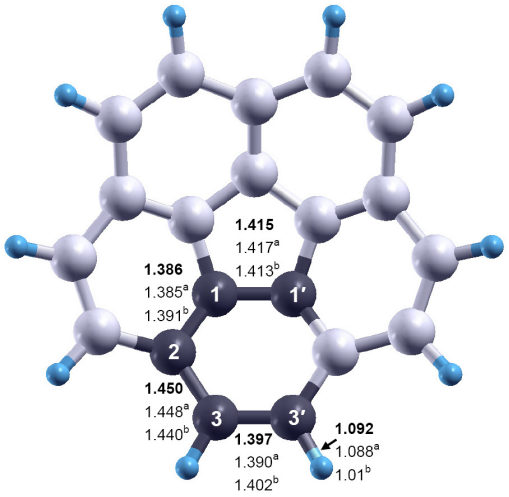


Figure 5.1: Ball-stick model of corannulene. Large and small spheres indicate C and H atoms, respectively. Bond lengths in Å are also indicated: bold numbers show our results, compared with literature data from (a) Hedberg et al., and (b) Hanson and Nordman.

## 5.4 Core level and valence photoemission

Figure 5.2 shows the C 1s photoemission spectrum of 1 ML corannulene on Ag (111). Note that a single feature centered at a binding energy (BE) of about 284.9±0.1 eV, and it is clearly skewed towards the higher BE side. This effect is attributed to the proximity of molecules to the metallic substrates, which is also reflected in the valence band spectrum shown in Figure 5.3, together with those

measured on the clean Ag(111) and the gas-phase spectrum. From Figure 5.3, we find that the molecular states can clearly be identified in the monolayer valence band, in particular the peak at ~3.2 eV binding energy. In comparison to the gas phase spectrum, it indicates that such feature stems from HOMO and HOMO−1 orbitals (both doubly degenerate). Conversely, a broad band is observed at higher energies. A small charge transfer from the metal surface to the corannulene molecule is observed in the UPS spectra, as witnessed by the small increase of the density of states close to the Fermi edge (see the inset), which is consistent with the relatively low electron affinity of corannulene (about 0.5±0.1eV [144]). However, the HOMO-states display a significant interaction with the Ag (111). This is reflected in the fact that the corannulene HOMOs are shifted to higher BE with respect to the gas phase molecule, and the molecules are not thermally desorbed from the surface but undergoes decomposition above 490–510 K, accompanied by the formation of a carbon layer and desorption of hydrogen gas.

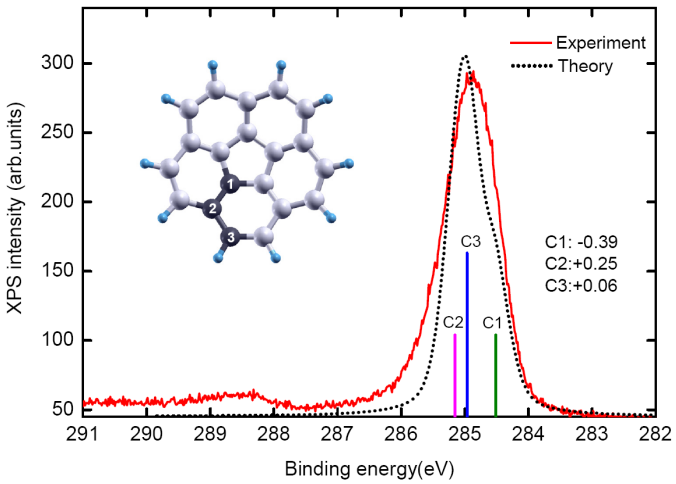


Figure 5.2: XPS spectrum of corannulene measured for 1 ML on Ag(111) with photo energy *hv*=515 eV (red solid line), compared to the simulated one (black dotted line). Vertical sticks numbered as in the inset show individual contributions from the three inequivalent atoms. The dashed line is obtained by broadening them with a pseudo-Voigt profile (50% Gaussion plus 50% Lorentzian both having full width at half maximum of 0.5 eV). The theoretical spectrum is aligned to 284.9 eV.

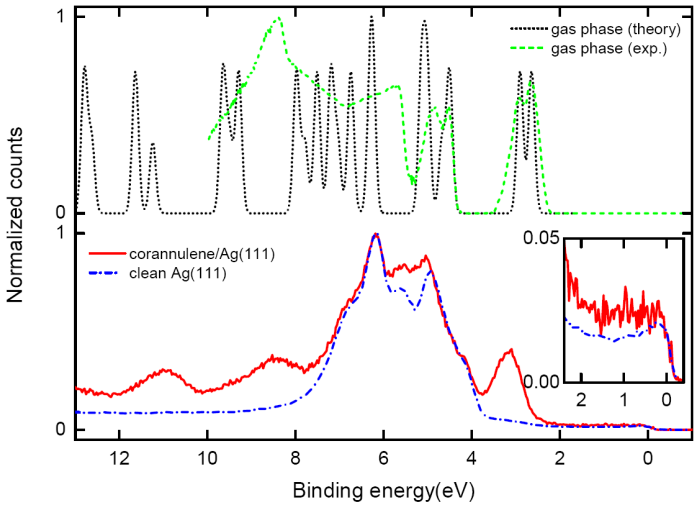


Figure 5.3: Vaslence band spectrum for corannulene on Ag(111) (red solid line) compared to clean Ag(111) (blue dash-dotted line). The inset enlarges the region around the Fermi edge. A gas phase photoemission spectrum (green dashed line) is also shown together with the DFT density of states for the free molecule (black dotted line).

Returning to the XPS spectrum in Figure 5.2, the small peak at 3.3±0.1 eV higher BE corresponds to shake-up satellite associated with the photoelectron energy loss for exciting a HOMO–LUMO transition. From the measured spectrum, the individual contributions by the three C species are unresolved. Instead, theoretical analysis can be used to determine the relative shifts between core level binding energies. We found that the most-abundant peripheral carbon atom C3 has intermediate BE, while the central C1 is at 0.45 eV lower BE than C3 and the intermediate C2 at 0.19 eV higher BE. The lower binding energy of the C1 atom with respect to C2 is consistent with predictions for fullerenes [137,140]. These results are further confirmed by comparing them with an additional calculation with the PBE0 hybrid functional [146]: the differences in BE between the two approaches are no larger than 0.02 eV. Overall, the simulated spectral width given by broadening

individual contributions with a pseudo-Voigt profile is consistent with experiments, also considering that the high-energy tail falls outside the scope of the current analysis and that theoretical analysis is performed for isolated molecules. The major discrepancy between calculations for the isolated molecules and measurements at 1ML/Ag(111) is associated with the larger weight measured in the spectral feature at low binding energy. The corresponding relative shift of some atomic contributions could be attributed to a different electron screening from the substrate of the same type carbon atoms, as originated by a tilting of the molecular axis with respect to the surface normal. In particular, the peripheral atoms C3 would probe a larger height difference in a tilted configuration, thus shifting the weight of the main XPS spectrum towards lower binding energy.

## 5.5 NEXAFS

The NEXAFS spectra measured for 1 ML of corannulene/Ag(111) at p- and s-polarizations are shown in Figure 5.4, where they are compared to our calculations for the isolated molecule. By comparing Figure 5.4a and Figure 5.4b for transverse magnetic (closely p-polarization) and transverse electric (s-polarization) scattering geometries, we observe very different relative intensities of the spectral features for the two polarizations, showing that the first resonances (to orbitals of $\pi^*$ symmetry) are strongly enhanced in p-polarization with respect to resonances at higher energy (typically of $\sigma^*$ symmetry). Accordingly, the spectra for p-polarization can be compared with calculation with the electric field parallel to the molecular axis and for s-polarization with the electric field perpendicular to it.

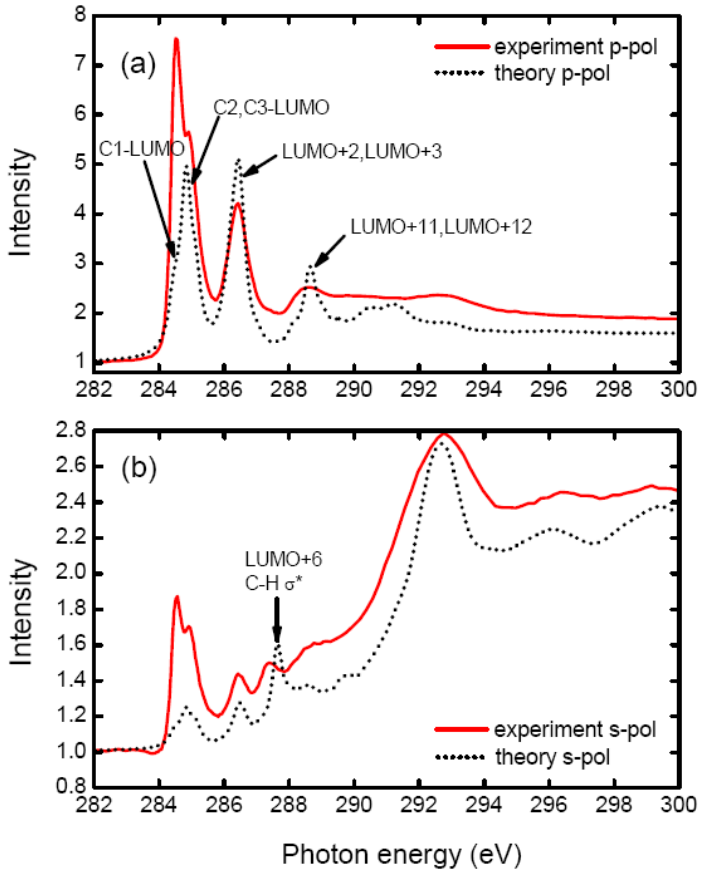


Figure 5.4: Comparison between NEXAFS spectrum of one monolayer of corannulene on Ag(111) (red solid line) and simulations for gas phase corannulene (black dotted line). Panel (a): experiments in p-polarization compared to simulations with photo electric field parallel to the five-fold molecular axis. Panel (b): s-polarization, compared to simulations averaged in the plane orthogonal to the molecular axis. Notice the different scale in the intensity axis of the two panels. The theoretical spectra are shifted by 289.5 eV to align to the experimental LUMO features.

Assuming a closely planar molecule, the ratio of the $\pi^*$-symmetry LUMO intensity in the opposite polarizations (~0.14) allows to estimate an average molecular tilt angle $\gamma \sim 28 \pm 2°$ according to the relationship $I_{TE} / I_{TM} = 1/2 \tan^2 \gamma$ [147]. Actually this value averages the effective tilting angle of the main molecular axis and the intrinsic convexity of the molecules, which results in a curvature of the

LUMO state as depicted in Figure 5.5. To quantify this effect and its influence on the NEXAFS LUMO resonance, we calculated the local projection of LUMO wavefunction $\Psi_{\mathrm{LUMO}}$ over the $2p$ atomic wavefunctions, $P_\nu = \left|\langle \Psi_{\mathrm{LUMO}} \mid 2p_\nu \rangle\right|^2$, with $\nu = z$ (parallel to the molecular axis) and $\nu = x, y$ (perpendicular to it), summed over the C1, C2, and C3 atom species. This allows us to evaluate the local slanting of the LUMO as $\theta = \arctan\left(\sqrt{P_{xy} / P_z}\right)$. The results shown in the table of Figure 5.5 indicate that a largest slanting of the LUMO is found at C2 atom, corresponding to an angle $\theta = 25°$ from the molecular axis. The LUMO slanting at the central C1 and peripheral C3 atoms, while lower, still amounts to $\theta \geq 18°$ from the molecular axis. Thus the average angle of the $\pi$ state is $\theta \approx 20°$ from the main molecular axis. When applying the Stöhr analysis to the theoretical NEXAFS simulations of an isolated molecule at zero tilt angle (Figure 5.4), we obtain a $23°$ contribution to the NEXAFS dichroism purely resulting from the molecular curvature. From comparison with the experimental value, we can reasonably assume that most of the molecules are oriented with their aromatic rings moderately tilted with respect to the surface by $\sim 5°$ on the average. Even considering a possibly smaller curvature of corannulene when adsorbed on Ag(111), our analysis points to a geometrical configuration where neither the pentagon ring nor a hexagon one directly faces the Ag atoms underneath, at variance with the case of the Cu(111) substrate, where hexagons directly face the surface (corresponding to a tilt angle of $20°$) [126].

Since our theoretical spectra are in excellent agreement with the experimental ones, we are able to interpret the measurements by means of the numerical analysis. The spectrum in p-polarization shows the first most prominent feature at about 285 eV being splitted 0.4 eV apart into two peaks of similar intensity, whereas

calculations for the isolated molecule rather predict a most pronounced second component as due to the contribution of both C2 and C3 type atoms (5 and 10 atoms respectively). Within an initial state analysis, which is ubiquitously true for LUMO analysis, the peak splitting can be explained in terms of major differences of binding energy among C3 peripheral atoms due to the different distance from the surface of a tilted molecule, thus increasing the prominence of the low energy component. This analysis is in full agreement with the observed shape of the C1s photoemission peak, where the detection of a peak splitting is prevented by the core level linewidth (intrinsically broader than NEXAFS LUMO resonances). The second, less intense feature of the spectrum in p-polarization lies at 286.4 eV. It can not be resolved in the specific contributions from the different C types either in measured or in the computed spectra. A third weaker and broader structure is observed close to the ionization threshold at ~288.6 eV both in the experiments and in the simulations, with resolution overly enhanced in the latter.

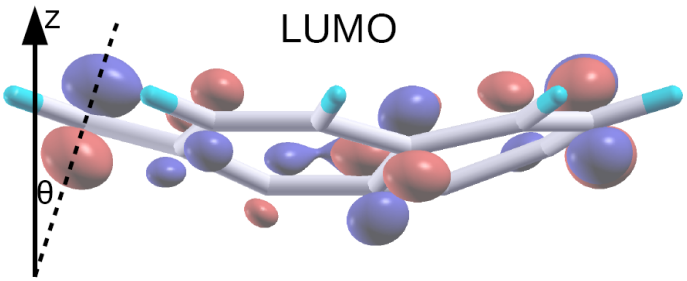


| | Pz | Pxy | θ |
|---|---|---|---|
| C1 | 17% | 2% | 19° |
| C2 | 15% | 3% | 25° |
| C3 | 52% | 6% | 18° |

Figure 5.5: Side view of the LUMO of gas phase corannulene and schematics of the local slanting of the $\pi$ state (here shown at a peripheral C3 atom). The stable reports the amplitude of the LUMO wavefunction over the 2*p* components, aligned along the molecular axis ($P_z$) and perpendicular to it ($P_{xy}$), and the effective angle formed by the LUMO with the z-axis at the various C sites.

Then we focus on the spectrum in s-polarization. It shows a relatively large residual intensity in the region of resonances due to the combination of molecular

convexity and tilt, whereas only the convexity is accounted for the residual contribution in the simulations. At slightly higher energy, instead, we can observe the peak at 287.4 eV, which displays opposite dichroism with respect to the $\pi^*$-symmetry LUMO and whose position is remarkably well reproduced by simulations at 287.6 eV. As we will see in better detail hereafter, this structure can be associated with the C–H bonds. Moreover, in the region of the continuum resonances, we observe three broad features with $\sigma^*$-symmetry (at about 293.0, 296.5, and 299.5 eV, respectively). The comparison with the simulated spectra highlights the adequateness of the theoretical approach which is able to capture with high accuracy their occurrence, energy spacing, and relative intensity.

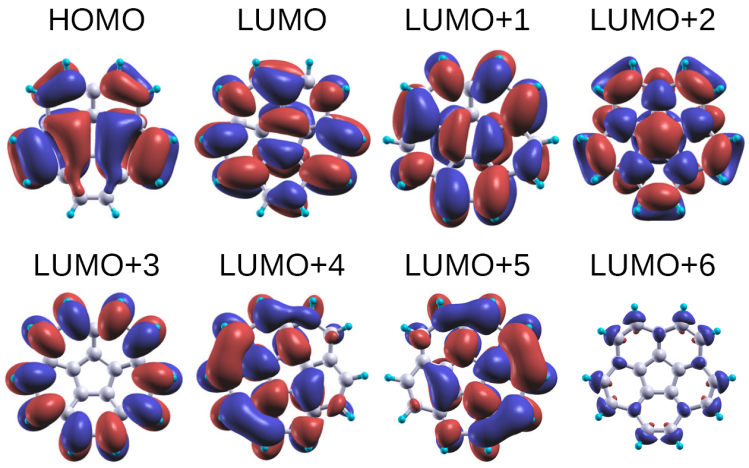


Figure 5.6: Molecular orbitals of gas phase corannulene. LUMO/LUMO+1 and LUMO+4/LUMO+5 are degenerate.

We next analyze the NEXAFS spectra in more detail. To this purpose, it is useful to recall the molecular orbitals of ground state corannulene in the gas phase, which have been computed at the Kohn-Sham PBE level and are shown in Figure 5.6. Their eigenvectors and Kohn-Sham eigenvalues are comparable to the ones in the literature [138]. Interestingly, the LUMO and LUMO+1 states are degenerate, as well as

LUMO+4 and LUMO+5. The lowest-lying state with symmetry is the LUMO+6 which involves the C–H bonds.

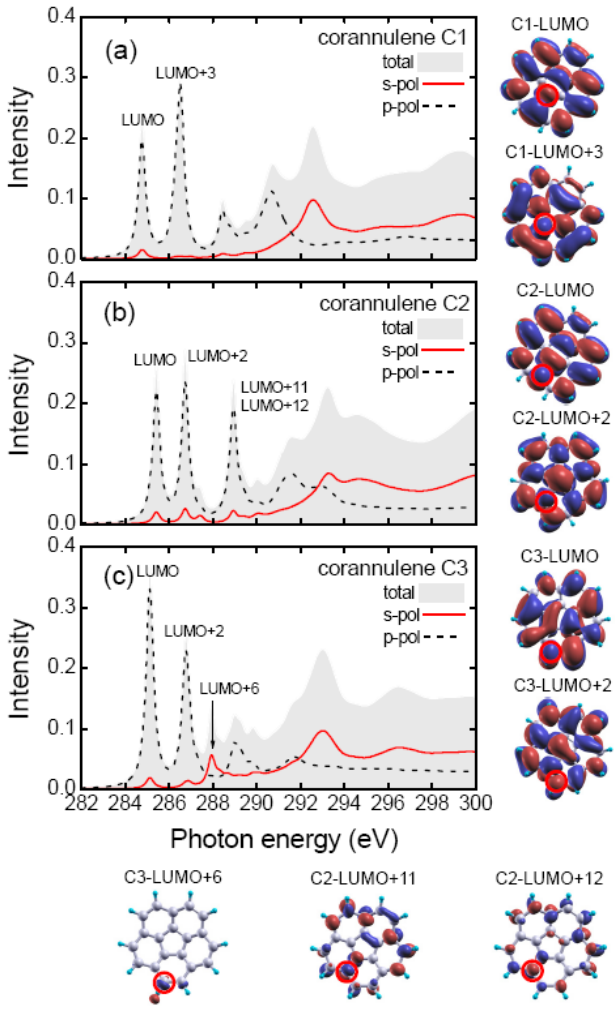


Figure 5.7: Panels (a), (b), and (c) show the contributions to the NEXAFS spectrum computed for the inequivalent C1, C2, and C3 species, respectively. The gray shaded area marks (three times) the average contribution, whereas the black dashed line correspond to the spectrum taken in p-polarization and the red solid line to that in s-polarization. On the right we depict the final-state orbitals for the first two spectral features, computed with the half-core-hole at the atom indicated with the red circle. The bottom line depicts, from left to right: the LUMO+6 orbital contributing to the $\sigma^*$ peak from C3; the LUMO+11 and LUMO+12 producing the overly sharp peak at 288.6 eV in the spectrum from C2. The theoretical spectra are shifted by 289.5 eV as in Figure 5.4.

Figure 5.7a–c show the simulated NEXAFS spectra for the inequivalent C1, C2, and C3 species. Note that all C species contribute to the first two peaks visible in p-polarization. The first one involves a final-state orbital which was computed with the half-core-hole and is mostly described in terms of ground state LUMO and LUMO+1 orbitals combined so as to maximize the amplitude on the excited atom; these states are shown in Figure 5.7 with labels as "C*n*-LUMO" (where we indicate the atom with core hole by C*n*). As can be seen in Figure 5.7a–c, the 1s LUMO contribution by C3 atoms is at an energy intermediate between those of C1 and C2, resulting in the structureless feature in the simulated spectrum at variance with the measured one (see Figure 5.4). As recalled in Section 5.4, in case of XPS analysis such mild discrepancy would be mitigated by considering a different screening of C3 atoms, which would shift leftwards part of the C3 contribution. The orthogonal combination of LUMO and LUMO+1, which vanishes at C*n*, bears no contribution to the spectrum. Thus the next peak is given by higher orbitals: for C1, by the excited C1-LUMO+3 shown in Figure 5.7, where we notice that this derives from a combination of the ground state LUMO+4/+5; for C2 and C3, by the excited C2-LUMO+2 and C3-LUMO+2, where the five-fold symmetry of the unperturbed LUMO+2 can still be recognized. The third feature (288.6 eV), which is much sharp in the theoretical spectrum in p-polarization, is instead mainly given by the C2 carbon atom, where it results from transition to two molecular orbitals, namely the C2-LUMO+11 and C2-LUMO+12 (see Figure 5.7). A relatively lower contribution by similar orbitals is also seen for the C1 and C3 atoms. The sharpness of their contribution is apparently overemphasized by the calculation. This can be understood by recalling that the theoretical description by a KS-GGA approach becomes problematic for states lying close to the vacuum level. There, the overestimated

electron affinity produces bond electron states which should instead be resonances within the continuum of unbound energy levels, as demonstrated in the analysis of NEXAFS spectra for pentacene [47]. Moving next to the NEXAFS simulated for the s-polarization, we can still see the signature of most structures considered so far, as the molecules is not perfectly planar. However, the first truly $\sigma^*$ orbital corresponds to the C3-LUMO+6 depicted in Figure 5.7, and relates to the C-H band for the excited C3 atom.

## 5.6 Conclusions

In this chapter, we investigated the unoccupied molecular orbitals of corannulene ($C_{20}H_{10}$) by the TP-DFT approach. In this study, and we collaborated with the experimental group of Dr. Andrea Goldoni at ELETTRA, Trieste, Italy who deposited a monolayer of such molecules on Ag (111), and measured XPS and NEXAFS. From our calculation of the intrinsic dichroism resulting from the corannulene curvature and polarization dependent NEXAFS measurement of the unoccupied molecular orbitals, we find molecules to be oriented at a small tilt angle of ~5 from the surface. The molecular tilting results in different electron screening of the core hole in XPS. The corresponding core level shifts broaden the C 1s photoemission peak and produce a splitting of the NEXAFS LUMO resonance, which is strongly contributed by all the C atoms. Higher energy transitions involve different molecular orbitals depending on the excited C atom. The lowest-lying state with σ symmetry, observed at 287.4 eV, relates to the C–H bonds.

# Chapter 6

# Conclusions

In this thesis we used Ab initio DFT methods to study organic molecules adsorbed on technologically relevant surfaces. We considered different system of interest.

We first investigated the adsorption of aromatic radicals on graphene. Our results show that the adsorption of such moiety, like phenyl, also functionalized with donor or acceptor groups generates a band gap and two spin-dependent mid-gap states located around the Fermi energy of pristine graphene, which cause a net magnetic moment. When one carbon atom of graphene is bound to the radical, the $p_z$ orbital of this atom is removed from the $\pi$ system band, leaving the orbitals in the other sublattice unpaired, which leads to nonzero magnetism. While the alignment of the energy resonant states of the adsorbate could be effectively changed by the functional groups in phenyl, the band gap of the full system and the midgap states resulted nearly independent of such modifications. This could be a way to magnetize graphene without strongly perturbing its lattice structure as it occurs by transition metal impurities [60].

Then we studied the adsorption of catechol and isonicotinic acid on the $TiO_2$ anatase (101) and rutile (110) surfaces by first-principles molecular dynamics simulations and the TDDFT method. We showed that thermal fluctuations induce changes in the position of the molecular levels around the $TiO_2$ valence band edge. In

particular, for the anatase (101) surface, the fluctuations of the alignment of the molecular levels with the $TiO_2$ valence band edge has an important effect on the absorption spectrum, while, for the rutile (110) surface, the same molecules induce only a minor effect. We extended this work towards more complex molecules, such as PTCDA and PTCDI adsorbed on the $TiO_2$ rutile (110) surface. These two species induce a more significant sensitization effect.

Finally we presented a thorough investigation of the unoccupied electronic states of corannulene adsorbed on Ag(111) combining our theoretical results with experiments based on photoemission and NEXAFS for a monolayer of molecules. The adsorption angle is deduced from the NEXAFS dichroism, by subtracting the intrinsic contribution owing to the molecular curvature as evaluated by ab initio calculations. We find an angle of ~5° at variance with the larger tilting earlier found on the Cu(111) surface where corannulene faces the substrate with an hexagon. Adsorption at a small tilt angle further allows us to determine the symmetry of the molecular orbitals of corannulene, identifying the spectral features. Surface-induced screening for atoms equivalent but for different heights influences the core-level shifts and determines the shape of the LUMO NEXAFS resonance. The excellent agreement between computed and measured spectra confirms the results and provides a validation of our investigation protocol for the study of polyaromatic molecules on surfaces.

# Appendix A

# Quantum Espresso

Quantum Espresso (QE) stands for Quantum Open Source Package for Research in Electronic structure Simulation and Optimization. It is an open source software distribution of packages used for running DFT based simulations to perform self-consistent electronic structure calculations, structure relaxations, molecular dynamics calculations, and materials modeling [54]. The Kohn-Sham (KS) equation is solved self-consistently for a set of fixed nuclear positions. Plane wave basis sets are used to represent the system wavefunctions. The ionic potential (nucleus+core electrons) is provided by the pseudopotential (PP). PPs could be Norm-conserving, Ultrasoft or Projected Augmented Wave (PAW) type. The LDA, GGA, hybrid functions and van der Waal's corrected functions are available [54]. Like in most DFT codes periodic boundary conditions are used also here, i.e the unit cell is repeated in all the three directions as in a crystal. To do calculations of isolated molecules, a large unit cell is to be used. And if one needs to simulate for example a slab, the unit cell employed should be larger only in one particular direction in which the interaction is to be minimized.

Iterative diagonalization is performed by using Davidson or conjugate gradient method in order to solve the KS equation. Self-consistency is achieved via the

modified Broyden method of. Finally, the structural optimizations are performed by using the Broyden-Fletcher-Goldfarb-Shanno (BFGS) quasi-Newton algorithm [54].

# Appendix B

# Molecular Orbital Projected Density of States (MOPDOS)

The contributions from the orbitals of the free molecule to the density of states of an adsorbed system can be determined by performing the Molecular Orbital Projected Density of Sates (MOPDOS) [84]. The procedure to compute the same, as we have implemented in moleculardpos.x within Quantum ESPRESSO is described here. In more general terms, one can analyze the electronic structure of a given system named "A" (here, the molecule/substrate interface) in terms of the energy levels of a part of it named "B" (here, the molecule). This approach may also be used to analyze a complex molecule in terms of its subunits, or a different electronic configuration (say, A is the molecule with a core-level excitation while B is the same but in the ground state as did to study excitation of corannulene, see Chapter 5).

If we indicate by $\left|\psi^{A}_{n_a\mathbf{k}}\right\rangle$ the eigenvectors of system A and by $\varepsilon^{A}_{n_a\mathbf{k}}$ its eigenvalues (same for system B), where **k** is the k-vector in the Brillouin zone with weight $\omega_{\mathbf{k}}$, the MOPDOS of system A, projected onto the $n_b$-th orbital of system B and evaluated at the energy *E* reads:

$$MOPDOS_{n_b}(E) = \sum_{n_a\mathbf{k}} \omega_{\mathbf{k}} \left|\left\langle \psi^{B}_{n_b\mathbf{k}} \middle| \psi^{A}_{n_a\mathbf{k}} \right\rangle\right|^2 \delta(E - \varepsilon^{A}_{n_a\mathbf{k}}) \qquad \text{(B.1)}$$

The eigenstates are computed by separate pw.x calculations (in the PWscf package of Quantum Espresso) for A and B; for consistency, the same unit cell and **k** sampling should be used. A shortcoming of the plane wave representation is that direct evaluation of the overlap integral $\left|\left\langle \psi^B_{n_b\mathbf{k}} \middle| \psi^A_{n_a\mathbf{k}} \right\rangle\right|^2$ requires handing the full states for the two systems, which can be computationally demanding already for a moderately large unit cell. Our implementation instead goes through a more efficient local basis set representation of the system. Let us indicate by $\left|\phi^{nlm}_I\right\rangle \equiv \left|\phi_\nu\right\rangle$ , with $\nu = (I,n,l,m)$ , the atomic wavefunction of atom $I$ with quantum numbers $n, l,$ and $m$. The number of such states, $N_\phi$, is generally much smaller than that of plane wave making the calculations more manageable.

Hence we can approximate the eigenfunctions in terms of this local basis set:

$$\left|\psi^A_{n_a\mathbf{k}}\right\rangle \approx \sum_\nu P^A_{n_a\mathbf{k},\nu} \left|\phi_\nu\right\rangle \tag{B.2}$$

$$\left|\psi^B_{n_a\mathbf{k}}\right\rangle \approx \sum_\nu P^B_{n_b\mathbf{k},\nu} \left|\phi_\nu\right\rangle \tag{B.3}$$

where the coefficients *P* are the complex projections of the KS eigenstates onto the local basis, $P^A_{n_a\mathbf{k},\nu} = \left\langle \phi_\nu \middle| \psi^A_{n_a\mathbf{k}} \right\rangle$ and similarly for B. The above expressions are approximate since the local basis set does not span completely the original Hilbert space (see, e.g., the "spilling") but this is often of no concern to a qualitative analysis. Within Quantum ESPRESSO, the coefficients *P* are computed by the projwfc.x code in a standard calculation of the DOS projected onto atomic orbitals and are stored in the file atomic_proj.xml. The execution of projwfc.x has to be performed for systems A and B separately.

The orbital overlaps in Eq. (B.1) are eventually computed from Eqs (B.2) and (B.3) as :

$$\left\langle \psi^{B}_{n_b\mathbf{k}} \middle| \psi^{A}_{n_a\mathbf{k}} \right\rangle = \sum_{\nu} (P^{B}_{n_b\mathbf{k},\nu})^{*} P^{A}_{n_a\mathbf{k},\nu} \tag{B.4}$$

Notice that the index in the summation should identify the same atomic state in the two systems for the local orbitals which are common for the two systems only. If system B is a subsystem of A, we have $N^{A}_{\phi} > N^{B}_{\phi}$ and the summation running over $N^{B}_{\phi}$ states. In all cases, the fraction of atomic states to be used can be specified in input by appropriate variables

(i_atmwfc_beg_full/part and i_atmwfc_end_full/part) such that:

(i_atmwfc_end_full) – (i_atmwfc_beg_full) + 1 = $N^{A}_{\phi}$ and

(i_atmwfc_end_part) – (i_atmwfc_beg_part) + 1 = $N^{B}_{\phi}$

# Bibliography


1 P. Hohenberg and W. Kohn. In homogeneous electron gas. *Physical Review*, 136: B864–871, 1964.

2 W. Kohn and L. J. Sham. Self-Consistent Equations Including Exchange and Correlation Effects. *Physical Review*, 140:A1133–1138, 1965.

3 G. Onida, L. Reining, and A. Rubio. Electronic excitations: density-functional versus many-body Green's function approaches. *Reviews of Modern Physics*, 74: 601–659, 2002.

4 R. Car and M. Parrinello. Unified Approach for Molecular Dynamics and Density-Functioinal Theory. *Physical Review Letters*, 55: 2471–2474, 1985.

5 K. S. Novoselov, A. K. Geim, S. V. Morozov, D. Jiang, Y. Zhang, S. V. Dubonos, I. V. Grigorieva, A. A. Firsov. Electric Field Effect in Atomically Thin Carbon Films. *Science*, 306: 666–669, 2004.

6 V. Georgakilas, M. Otyepka, A. B. Bourlinos, V. Chandra, N. Kim, K. C. Kemp, P. Hobza, R. Zboril, and K. S. Kim. Functionalization of Graphene: Covalent and Non-Covalent Approaches, Derivatives and Applications. *Chemical Reviews*, 112: 6156–6214, 2012.

7 B. Huang, F. Liu, J. Wu, B. L. Gu, and W. Duan. Suppression of spin polarization in graphene nanoribbons by edge defects and impurities. *Physical Review B*, 77: 153411, 2008.

8 J. J. Palacios and J. Fernández-Rossier. Vacancy-induced magnetism in graphene and graphene ribbons. *Physical Review B*, 77: 195428, 2008.

9 O. V. Yazyev and L. Helm. Defect-induced magnetism in graphene. *Physical*

*Review B*, 75: 125408, 2007.

10 M. Garnica, D. Stradi, S. Barja, F. Calleja, C. Díaz, M. Alcamí, N. Martín, A. L. Vázquez de Parga, Fernando Martín, and R. Miranda. Long-range magnetic order in a purely organic 2D layer adsorbed on epitaxial graphene. *Nature Physics*, 9: 368–374, 2013.

11 E. J. G. Santos, A. Ayuela, and D. Sánchez-Portal. Universal magnetic properties of $sp^3$-type defects in covalently functioinalized graphene. *New Journal of Physics*, 14: 043022, 2012.

12 L. Kavan, M. Grätzel, S. E. Gilbert, C. Klemenz, and H. J. Scheel. Electrochemical and Photoelectrochemical Investigation of Single-Crystal Anatase. *Journal of the American Chemical Society*, 118: 6716–6723, 1996.

13 U. Diebold, The surface science of titanium dioxide. *Surface Science Reports*, 48: 53–229, 2003.

14 S. G. Abuabara, L. G. C. Rego, and V. S. Batista. Influence of Thermal Fluctuations on Interfacial Electron Transfer in Functionalized $TiO_2$ Semiconductors. *Journal of the American Chemical Society*, 127: 18234–18242, 2005.

15 S.-C. Li, J.-G. Wang, P Jacobson, X.-Q. Gong, A. Selloni, and U. Diebold. Correlation between Bonding Geometry and Band Gap States at Organic-Inorganic Interfaces: Catechol on Rutile $TiO_2$ (110). *Journal of the American Chemical Society*, 131: 980–984, 2009.

16 F. Risplendi, G. Cicero, G. Mallia, and N. M. A. Harrison. Quantum-Mechanical Study of the Adsorption of Prototype Dye Molecules on Rutile-$TiO_2$ (110): A Comparison between Catechol and Isonicotinic Acid. *Physical Chemistry Chemical Physics*, 15: 235–243, 2013.

17 D. J. Mowbray and A. Migani. Using $G_0W_0$ Level Alignment to Identify Catechol's Structure on $TiO_2$ (110). *Journal of Physical Chemistry C*, 119: 19634–19641, 2015.

18 S.-C. Li, Y. Losovyj, and U. Diebold. Adsorption-Site-Dependent Electronic Structure of Catechol on the Anatase $TiO_2$ (101) Surface. *Langmuir*, 27: 8600–8604, 2011.

19 S.-C. Li, L.-N. Chu, X.-Q. Gong, and U. Diebold. Hydrogen Bonding Controls the Dynamics of Catechol Adsorbed on a $TiO_2$ (110). *Science*, 328: 882–884, 2010.

20 S. Rangan, J.-P. Theisen, E. Bersch, and R. A. Bartynski. Energy Level Alignment of Catechol Molecular Orbitals on ZnO (1120) and $TiO_2$ (110) surfaces. *Applied Surface Science*, 256: 4829–4833, 2010.

21 A. Calzolari, A. Ruini, and A. Catellani. Surface Effects on Catechol/Semiconductor Interfaces. *Journal of Physical Chemistry C*, 116: 17158–17163, 2012.

22 W. R. Duncan and O. V. Prezhdo. Electronic Structure and Spectra of Catechol and Alizarin in the Gas Phase and Attached to Titanium. *Journal of Physical Chemistry B*, 109: 365–373, 2005.

23 W. R. Duncan and O. V. Prezhdo. Theoretical Studies of Photoinduced Electron Transfer in Dye-Sensitized $TiO_2$. *Annual Review of Physical Chemistry*, 58: 143–184, 2007.

24 P. Persson, S. Lunell, and L. Ojamäe. Electronic Interactions between Aromatic Adsorbates and Metal Oxide Substrates Calculated from First Principles. *Chemical Physics Letters*, 364: 469–474, 2002.

25 M. Nilsing, P. Persson, and L. Ojamäe. Anchor Group Influence on

Molecule-Metal Oxide Interfaces: Periodic Hybrid DFT Study of Pyridine Bond to $TiO_2$ via Carboxylic and Phosphonic Acid. *Chemical Physics Letters*, 415: 375–380, 2005.

26 G. Fratesi, C. Motta, M. I. Trioni, G. P. Brivio, and D. Sánchez-Portal. Resonant Lifetime of Core-Excited Organic Adsorbates from First Principles. *Journal of Physical Chemistry C*, 118: 8775–8782, 2014.

27 L.-M. Liu, S.-C. Li, H. Cheng, U. Diebold, A. Selloni. Growth and Organization of an Organic Molecular Monolayer on $TiO_2$: Catechol on Anatase (101). *Journal of the American Chemical Society*, 133: 7816–7823, 2011.

28 K. L. Syres, A. G. Thomas, W. R. Flavell, B. F. Spencer, F. Bondino, M. Malvestuto, A. Preobrajenski, M. Grätzel. Adsorbate-Induced Modification of Surface Electronic Structure: Pyrocatechol Adsorption on the Anatase $TiO_2$ (101) and Rutile $TiO_2$ (110) Surfaces. *Journal of Physical Chemistry C*, 116: 23515–23525, 2012.

29 G. Giorgi, J.-i. Fujisawa, H. Segawa, K. Yamashita. Unraveling the adsorption Mechanism of Aromatic and Aliphatic Diols on the $TiO_2$ surface: A Density Functional Theory Analysis. *Physical Chemistry Chemical Physics*, 15: 9761–9767, 2013.

30 R. Sánchez-de-Armas, M. A. San-Miguel, J. Oviedo, A. Márquez, J. F. Sanz. Electronic Structure and Optical Spectra of Catechol on $TiO_2$ Nanoparticles from Real Time TD-DFT Simulations. *Physical Chemistry Chemical Physics*, 13: 1506–1514, 2011.

31 R. Sánchez-de-Armas, J. Oviedo, M. A. San-Miguel, J. F. Sanz. Direct vs Indirct Mechanisms for Electron Injection in Dye-Sensitized Solar Cells. *Journal of Physical Chemistry C*, 115: 11293–11301, 2011.

32 W. E. Barth and R. G. Lawton. Dibenzo [*ghi,mno*] fluoranthene. *Journal of the American Chemical Society*, 88: 380–381, 1966.

33 Y.-T. Wu and J. S. Siegel. Aromatic Molecular-Bowl Hydrocarbons: Synthetic Derivatives, Their Structures, and Physical Properties. *Chemical Reviews*, 106: 4843–4867, 2006.

34 A. M. Butterfield, B. Gilomen, and J. S. Siegel. Kilogram-Scale Production of Corannulene. *Organic Process Research and Development*, 16: 664–676, 2012.

35 J. P. Perdew, K. Burke, and M. Ernzerhof. Generalized Gradient Approximation Made Simple. *Physical Review Letters*, 77: 3865–3868, 1996.

36 J. P. Perdew and Y. Wang. Accurate and simple analytic representation of the electron-gas correlation energy. *Physical Review B*, 45: 13244–13249, 1992.

37 S. Grimme. Semiempirical GGA-Type Density Functional Constructed with a Long-Range Dispersion Correction. *Journal of Computational Chemistry*, 27: 1787–1799, 2006.

38 E. Runge and E. K. U. Gross. Density-Functional Theory for Time-Dependent Systems. *Physical Review Letters*, 52: 997–1000, 1984.

39 D. Marx and J. Hutter. *Ab Initio Molecular Dynamics: Basic Theory and Advanced Methods*. Cambridge University Press, 2009.

40 S. Nosé. A Molecular Dynamics Method for Simulations in the Canonical Ensemble. *Molecular Physics*, 52: 255–268, 1984.

41 W. G. Hoover, A. J. C. Ladd, and B. Moran. High-Strain-Rate Plastic Flow Studied via Nonequilibrium Molecular Dynamics. *Physical Review Letters*, 48: 1818–1820, 1982.

42 W. G. Hoover. Canonical Dynamics: Equilibrium Phase-Space Distributions. *Physical Review A*, 31: 1695–1697, 1985.

43 S. García-Gil, A. García, and P. Oredejón. Calculation of Core Level Shifts within DFT Using Pseudopotentials and Localized Basis Sets. *European Physical Journal B*, 85: 239, 2012.

44 M. A. L. Marques, N. T. Maitra, F. M. S. Nogueira, E. K. U. Gross. *Fundamentals of Time-Dependent Density Functional Theory*. Springer-Verlag Berlin Heidelberg, 2012.

45 D. Rocca, R. Gebauer, Y. Saad, and S. Baroni. Turbo Charging Time-Dependent Density-Functional Theory with Lanczos Chains. *Journal of Chemical Physics*, 128: 154105, 2008.

46 O. B. Malcıoğlu, R. Gebauer, D. Rocca, and S. Baroni. TurboTDDFT-A Code for the Simulation of Molecular Spectra Using the Liouville-Lanczos Approach to Time-Dependent Density-Functional Perturbation Theory. *Computer Physics Communications*, 52: 255–268, 1984.

47 G. Fratesi, V. Lanzilotto, L. Floreano, and G. P. Brivio. Azimuthal Dichroism in Near-Edge X-ray Absorption Fine Structure Spectra of Planar Molecules. *Journal of Physical Chemistry C*, 117: 6632–6638, 2013.

48 C. Brouder. Angular Dependence of x-ray Absorption Spectra. *J. Phys.: Condens. Matter*, 2: 701–738, 1990.

49 M. Taillefumier, D. Cabaret, A.-M. Flank, and F. Mauri. X-ray absorption near-edge structure calculations with the pseudopotentials: application to the *K* edge in diamond and $\alpha$-quartz. *Physical Review B*, 66: 195107, 2002.

50 L. Triguero, L. G. M. Pettersson, and H. Ågren. Calculations of near-edge x-ray-absorption spectra of gas-phase and chemisorbed molecules by means of density-functional and transition-potential theory. *Physical Review B*, 58: 8097–8110, 1998.

51 C. Gougoussis, M. Calandra, A. P. Seitsonen, and F. Mauri. First-principles calculations of x-ray absorption in a scheme based on ultrasoft pseudopotentials: From $\alpha$-quartz to high-$T_c$ compounds. *Physical Review B*, 80: 075102, 2009.

52 A. Baby, G. Fratesi, S. R. Vaidya, L. L. Patera, C. Africh, L. Floreano, and G. P. Brivio. Anchoring and bending of pentacene on Aluminum (001). *Journal of Physical Chemistry C*, 119: 3624–3633, 2015.

53 A. Baby, H. Lin, G. P. Brivio, L. Floreano, and G. Fratesi. Core-level spectra and molecular deformation in adsorption: V-shaped pentacene on Al (001). *Beilstein Journal of Nanotechnology*, 6: 2242–2251, 2015.

54 P. Giannozzi, S. Baroni, N. Bonini, M. Calandra, R. Car, C. Cavazzoni, D. Ceresoli, G. L. Chiarotti, M. Cococcioni, I. Dabo, A. Dal Corso, S. de Gironcoli, S. Fabris, G. Fratesi, R. Gebauer, U. Gerstmann, C. Gougoussis, A. Kokalj, M. Lazzeri, L. Martin-Samos, N. Marzari, F. Mauri, R. Mazzarello, S. Paolini, A. Pasquarello, L. Paulatto, C. Sbraccia, S. Scandolo, G. Sclauzero, A. P. Seitsonen, A. Smogunov, P. Umari, and R. M. Wentzcovitch. QUANTUM ESPRESSO: a modular and open-source software project for quantum simulations of materials. *Journal of Physics: Condensed Matter*, 21: 395502, 2009.

55 S. Choi, B. W. Jeong, S. Kim, and G. Kim. Monovacancy-induced magnetism in graphene bilayers. *Journal of Physics: Condensed Matter*, 20: 235220, 2008.

56 L. Pisani, J. A. Chan, B. Montanari, and N. M. Harrison. Electronic structure and magnetic properties of graphitic ribbons. *Physical Review B*, 75: 064418, 2007.

57 M. Topsakal, H. Sevinçli, and S. Ciraci. Spin confinement in the superlattices of graphene ribbons. *Applied Physics Letters*, 92: 173118, 2008.

58 J. Fernández-Rossier and J. J. Palacios. Magnetism in Graphene Nanoislands. *Physical Physics Letters*, 99: 177204, 2007.

59 J. Zhou, Q. Wang, Q. Sun, X. S. Chen, Y. Kawazoe, and P. Jena. Ferromagnetism in Semihydrogenated Graphene Sheet. *Nano Letters*, 9: 3867–3870, 2009.

60 H. Sevinçli, M. Topsakal, E. Durgun, and C. Ciraci. Electronic and magnetic properties of 3d transition-metal atom adsorbed graphene and graphene nanoribbons. *Physical Review B*, 77: 195434, 2008.

61 I. Zanella, S. B. Fagan, R. Mota and A. Fazzio, Electronic and Magnetic Properties of Ti and Fe on Graphene. *Journal of Physical Chemistry C*, 112: 9163–9167, 2008.

62 I. Zanella, S. Guerini, S. B. Fagan, J. Mendes Filho, and A. G. Souza Filho. Chemical doping-induced gap opening and spin polarization in graphene. *Physical Review B*, 77: 073404, 2008.

63 D. C. Elias, R. R. Nair, T. M. G. Mohiuddin, S. V. Morozov, P. Blake, M. P. Halsall, A. C. Ferrari, D. W. Boukhvalov, M. I. Katsnelson, A. K. Geim, and K. S. Novoselov. *Science*, 323: 610–613, 2009.

64 R. Galog, B. Jorgensen, L. Nisson, M. Andersen, E. Rienks, M. Bianchi, M. Fanetti, E. Lagsgaard, A. Baraldi, S. Lizzit, Z. Sljivancanin, F. Besenbacher, B. Hammer, T. G. Pedersen, P. Hofmann, and L. Hornekar. *Nature Materials*, 9: 315–319, 2010.

65 S. Casolo, O. M. Løvvik, R. Martinazzo, and G. F. Tantardini. Understanding adsorption of hydrogen atoms on graphene. *Journal of Chemical Physics*, 130: 054704, 2009.

66 P. Chandrachud, B. S. Pujari, S. Haldar, B. Sanyal, and D. G. Kanhere. A systematic study of electronic structure from graphene to graphane. *Journal of Physics: Condensed Matter*, 22: 465502, 2010.

67 J. L. Cheng, C. Salazar, and J. E. Sipe. Optical properties of functionalized graphene. *Physical Review B*, 88: 045438, 2013.

68 H. Gao, L. Wang, J. Zhao, F. Ding, and J. Lu. Band Gap Tuning of Hydrogenated Graphene: H Coverage and Configuration Dependence. *Journal of Physical Chemistry C*, 8: 3236–3242, 2011.

69 R. Martinazzo. *In Handbook of Graphene Science*. CRC press, Londan, UK, 2014, in press.

70 V. Georgakilas, M. Otyepka, A. B. Bourlinos, V. Chandra, N. Kim, K. C. Kemp, P. Hobza, R. Zboril, and K. S. Kim. Functionalization of Graphene: Covalent and Non-Covalent Approaches, Derivatives and Applications. *Chemical Reviews*, 112: 6156–6214, 2012.

71 A. Sinitskii, A, Dimiev, D. A. Corley, A. A. Fursina, D. V. Kosynkin, and J. M. Tour. Kinetics of Diazonium Functionalization of Chemically Converted Graphene Nanoribbons. *ACS Nano*, 4: 1949–1954, 2010.

72 S. Niyogi, E. Bekyarova, M. E. Itkis, H. Zhang, K. Shepperd, J. Hicks, M. Sprinkle, C. Berger, C. N. Lau, W. A. deHeer, E. H. Conrad, and R. C. Haddon. Spectroscopy of Covalently Functionalized Graphene. *Nano Letters*, 10: 4061–4066, 2010.

73 P. M. Kirkman, A. G. Güell, A. S. Cuharuc, and P. R. Unwin. Spatial and Temporal Control of the Diazonium Modification of $sp^2$ Carbon Surfaces. *Journal of the American Chemical Society*, 136: 36–39, 2014.

74 H. Liu, S. Ryu, Z. Chen, M. L. Steigerwald, C. Nuckolls, and L. E. Brus. Photochemical Reactivity of Graphene. *Journal of the American Chemical Society*, 131: 17099–17101, 2009.

75 P. Salice, E. Fabris, C. Sartorio, D. Fenaroli, V. Figà, M. P. Casaletto, S. Cataldo,

B. Pignataro, and E. Menna. An insight into the functionalisation of carbon nanotubes by diazonium chemistry: Towards a controlled decoration. *Carbon*, 74: 73–82, 2014.

76 C.-H. Chang, X. Fan, L.-J. Li, and J.-L. Kuo. Band Gap Tuning of Graphene by Adsorption of Aromatic Molecules. *Journal of Physical Chemistry C*, 116: 13788–13794, 2012.

77 O. Desyatnyk, L. Pszczółkowski, S. Thorwirth, T. M. Krygowski, and Z. Kisiel. The rotational spectra, electric dipole moments and molecular structures of anisole and benzaldehyde. *Physical Chemistry Chemical Physics*, 7: 1708–1715, 2005.

78 A. Aryasetiawan and O. Gunnarsson. The *GW* method. *Rep. Prog. Phys.*, 61: 237–312, 1998.

79 G. Fratesi, G. P. Brivio, and L. G. Molinari. Many-body method for infinite nonperiodic systems. *Physical Review B*, 69: 245113, 2004.

80 P. E. Trevisanutto, C. Giorgetti, L. Reining, M. Ladisa, and V. Olevano. Ab Initio GW Many-Body Effects in Graphene. *Physical Review Letters*, 101: 226405, 2008.

81 A. Qaiumzadeh, K. Jahanbani, and R. Asgari. Spin polarization dependence of quasiparticle properties in graphene. *Physical Review B*, 85: 235428, 2012.

82 R. Martinazzo, S. Casolo, and G. F. Tantardini. Symmetry-induced band-gap opening in graphene superlattices. *Physical Review B*, 81: 245420, 2010.

83 M. Garnica, D. Stradi, S. Barja, F. Calleja, C. Daz, M. Alcam, N. Martn, A. L. Vázquez de Parga, F. Martn, and R. Miranda. Long-range magnetic order in a purely organic 2D layer adsorbed on epitaxial graphene. *Nature Physics*, 9: 368–374, 2013.

84 A. Ravikumar, A. Baby, H. Lin, G. P. Brivio, G. Fratesi. Femtomagnetism in graphene induced by core level excitation of organic adsorbates. *Scientific Reports*, 6: 24603, 2016.

85 K.-Y. Lian, Y.-F. Ji, X.-F. Li, M.-X. Jin, D.-J. Ding, and Y. Luo. Big Bandgap in Highly Reduced Graphene Oxides. *Journal of Physical Chemistry C*, 117: 6049–6054, 2013.

86 P. Löwdin. *Journal of Chemical Physics*, 18: 365–375, 1950.

87 E. J. G. Santos, D. Sánchez-Portal and A. Ayuela. Magnetism of covalently functionalized carbon nanotubes. *Applied Physics Letters*, 99: 062503, 2011.

88 I. V. Lara, I. Zanella, A. G. Souza Filho, and S. B. Fagan. Influence of concentration and position of carboxyl groups on the electronic properties of single-walled carbon nanotubes. *Physical Chemistry Chemical Physics*, 16: 21602–21608, 2014.

89 E. H. Lieb. Two Theorems on the Hubbard Model. *Physical Review Letters*, 62: 1201–1204, 1989.

90 B. O'Regan, M. Grätzel. A low-cost, High-Efficiency Solar Cell Based on Dye-Sensitized Colloidal $TiO_2$ Films. *Nature*, 353: 737–740, 1991.

91 M. Grätzel. Recent Advances in Sensitized Mesoscopic Solar Cells. *Accounts of Chemical Research*, 42: 1788–1798, 2009.

92 A. Hagfeldt, G. Boschloo, L. Sun, L. Kloo, H. Pettersson. Dye-Sensitized Solar Cells. *Chemical Reviews*, 110: 6595–6663, 2010.

93 L. Zhang and J. M. Cole. Anchoring Groups for Dye-Sensitized Solar Cells. *ACS Applied Materials and Interfaces*, 7: 3427–3455, 2015.

94 J. Moser, S. Punchihewa, P. P. Infelta, and M. Grätzel. Surface Complexation of Colloidal Semiconductors Strongly Enhances Interfacial Electron-Transfer Rates.

*Langmuir*, 7: 3012–3018, 1991.

95 P. Persson, R. Bergström, and S. Lunell. Quantum Chemical Study of Photoinjection Processes in Dye-Sensitized $TiO_2$ Nanoparticles. *Journal of Physical Chemistry B*, 104: 10348–10351, 2000.

96 H. Z. Zhang and J. F. Banfield. Thermodynamics analysis of phase stability of nanocrystalline titania. *Materials Chemistry*, 8: 2073–2076, 1998.

97 M. R. Ranade, A. Navrotsky, H. Z. Zhang, J. F. Banfield, S. H. Elder, A. Zaban, P. H. Borse, S. K. Kulkarni, G. S. Doran, H. J. Whitfield. Energetics of Nanocrystalline $TiO_2$. *Proc. Natl. Acad. Sci. U. S. A.*, 99: 6476–6481, 2002.

98 G. Li, L. Li, J. Boerio-Goates, B. F. Woodfield. High Purity Anatase TiO2 Nanocrystals: Near Room-Temperature Synthesis, Grain Growth Kinetics, and Surface Hydration Chemistry. *Journal of the American Chemical Society*, 127: 8659–8666, 2005.

99 A. S. Barnard, P. Zapol, and L. A. Curtiss. Modeling the Morphology and Phase Stability of $TiO_2$ Nanocrystals in Water. *Journal of Chemical Theory and Computation*, 1: 107–116, 2005.

100 A. S. Barnard and L. A. Curtiss. Prediction of $TiO_2$ Nanoparticle Phase and Shape Transitions Controlled by surface Chemistry. *Nano Letters*, 5: 1261–1266, 2005.

101 S. D. Burnside, V. Shklover, C. Barbé, P. Comte, F. Arendse, K. Brooks, and M. Grätzel. Self-Organization of $TiO_2$ Nanoparticles in Thin Films. *Chemistry of Materials*, 10: 2419–2425, 1998.

102 Y. Wang, K. Hang, N. A. Anderson, and T. Lian. Comparison of Electron Transfer Dynamics in Molecule-to-Nanoparticle and Intramolecular Charge Transfer Complexes. *Journal of Physical Chemistry B*, 107: 9434–9440, 2003.

103 I. A. Janković, Z. V. Šaponjić, M. I. Čomor, and J. M. Nedeljković. Surface Modification of Colloidal $TiO_2$ Nanoparticles with Bidentate Benzene Derivatives. *Journal of Physical Chemistry C*, 113: 12645–12652, 2009.

104 G. P. Brivio and M. I. Trioni. The Adiabatic Molecule-Metal Surface Interaction Theoretical Approaches. *Reviews of Modern Physics*, 71: 231–265, 1999.

105 G. P. Brivio, G. Butti, S. Caravati, G. Fratesi, and M. I. Trioni. Theoretical approaches in adsorption: alkali adatom investigations. *Journal of Physics: Condensed Matter*, 19: 305005, 2007.

106 P. A. Connor, K. D. Dobson, and A. J. McQuillan. New Sol-Gel Attenuated Total Reflection Infrared Spectroscopic Method for Analysis of Adsorption at Metal Oxide Surface in Aqueous Solutions. Chelation of $TiO_2$, $ZrO_2$, and $Al_2O_3$ Surfaces by Catechol, 8-Quinolinol, and Acetylacetone. *Langmuir*, 11: 4193–4195, 1995.

107 P. Z. Araujo, C. B. Mendive, L. A. G. Rodenas, P. J. Morando, A. E. Regazzoni, M. A. Blesa, D. Bahnemann. FT-IR-ATR as a tool to probe photocatalytic interfaces. *Colloids Surf., A*, 265: 73–80, 2005.

108 D. O. Scanlon, C. W. Dunnill, J. Buckeridge, S. A. Shevlin, A. J. Logsdail, S. M. Woodley, C. R. A. Catlow, M. J. Powell, R. G. Palgrave, I. P. Parkin, G. W. Watson, T. W. Keal, P. Sherwood, A. Walsh, and A. A. Sokol. *Nature Materials*, 12: 798–801, 2013.

109 A. Sygula, F. R. Fronczek, R. Sygula, P. W. Rabideau, M. M. Olmstead. A Double Concave Hydrocarbon Buckycatcher. *Journal of the American Chemical Society*, 129: 3842–3843, 2009.

110 W. Xiao, D. Passerone, P. Ruffieux, K. Aït-Mansour, O, Gröning, E. Tosatti, J. S. Siegel, and R. Fasel. *Journal of the American Chemical Society*, 130: 4767–4771,

2008.

111 A. S. Filatov, M. V. Ferguson, S. N. Spisak, B. Li, C. F. Campana, M. A. Petrukhina. Bowl-Shaped Polyarenes as Concave-Convex Shape Complementary Hosts for $C_{60}$- and $C_{70}$-Fullerenes. *Crystal Growth and Design*, 14: 756–762, 2014.

112 P. Vilmercati, C. Castellarin-Cudia, R. Gebauer, P. Ghosh, S. Lizzit, L. Petaccia, C. Cepek, R. Larciprete, A. Verdini, L. Floreano, A. Morgante, A. Goldoni. Mesoscopic Donor-Acceptor Multilayer by Ultrahigh-Vacuum Codeposition of Zn-Tetraphenyl-Porphyrin and $C_{70}$. *Journal of the American Chemical Society*, 131: 644–652, 2008.

113 T. Schiros, G. Kladnik, D. Prezzi, A. Ferretti, G. Olivieri, A. Cossaro, L. Floreano, A. Verdini, C. Schenck, M. Cox, A. A. Gorodetsky, K, Plunkett, D. Delongchamp, C. Nuckolls, A. Morgante, D. Cvetko, and L. Kymissis. Donor-Acceptor Shape Matching Drives Performance in Photovoltaics. *Advanced Energy Materials*, 3: 894–902, 2013.

114 W. Xiao, K.-H. Ernst, K. Palotas, Y. Zhang, E. Bruyer, L. Peng, T. Greber, W. Hofer, L. Scott, R. Fasel. Microscopic origin of chiral shape induction in achiral crystals. *Nature Chemistry*, 8: 326–330, 2016.

115 I. V. Kuvychko, S. N. Spisak, Y.-S. Chen, A. A. Popov, M. A. Petrukhina, S. H. Strauss, O. V. Boltalina. A buckybowl with a Lot of Potential: $C_5$-$C_{20}H_5(CF_3)_5$. *Angew. Chem. Int. Ed.*, 51: 4939–4942, 2012.

116 B. M. Schmidt, S. Seki, B. Topolinski, K. Ohkubo, S. Fukuzumi, H. Sakurai, D. Lentz. *Angew. Chem. Int. Ed.*, 51: 4939–4942, 2012.

117 I. V. Kuvychko, C. Dubceac, S. H. M. Deng, X.-B. Wang, A. A. Granovsky, A. A. Popov, M. A. Petrukhina, S. H. Strauss, O. V. Boltalina, $C_{20}H_4(C_4F_8)_3$: A

Fluorine-Containing Annulated Corannulene that Is a Better Electron Acceptor Than $C_{60}$. *Angew. Chem. Int. Ed.*, 52: 7505–7508, 2013.

118 B. M. Schmidt, B. Topolinski, M. Yamada, S. Higashibayashi, M. Shionoya, H. Sakurai, D. Lentz. Electronic Properties of Trifluoromethylated Corannulenes. *Chem. -Eur. J.*, 19: 13872–13880, 2013.

119 L. K. San, T. T. Clikeman, C. Dubceac, A. A. Popov, Y.-S. Chen, M. A. Petrukhina, S. H. Strauss, O. V. Botalina. Corannulene Molecular Rotor with Flexible Perfluorobenzyl Blades: Synthesis, Structure and Properties. *Chem. -Eur. J.*, 21: 9488–9492, 2015.

120 R. Chen, R.-Q. Lu, K. Shi, F. Wu, H.-X. Fang, Z.-X. Niu, X.-Y. Yan, M. Luo, X.-C. Wang, C.-Y. Yang, X.-Y. Wang, B. Xu, H. Xia, J. Pei, X.-Y. Cao. Corannulene derivatives with low LUMO levels and dense convex-concave packing for n-channel organic field-effect transistors. *Chem.Commun.*, 51: 13768–13771, 2015.

121 S. Sanyal, A. K. Manna, S. K. Pati. Functioinal Corannulene: Diverse Structures, Enhanced Charge Transport, and Tunable Optoelectronic Properties. *ChemPhysChem*, 15: 885–893, 2014.

122 A. Sygula and S. Saebø. π–π Stacking of Curved Carbon Networks: The Corannulene Dimer. *Int. J. Quantum Chem*, 109: 65–72, 2009.

123 K. Narita, S. Okada. Geometric and electronic structures of corannulene polymers: Ultra narrow graphene ribbons with corrugation and topological defects. *Chemical Physics Letters*, 650: 76–81, 2016.

124 O. I. Obolensky, V. V. Semenikhina, A. V. Solov'yov, W. Greiner. Interplay of Electrostatic and van der Waals Forces in Coronene Dimer. *Int. J. Quantum Chem*, 107: 1335–1343, 2007.

125 M. Parschau, R. Fasel, K.-H. Ernst, O. Gröning, L. Brandenberger, R. Schillinger, T. Greber, A. Seitsomen, Y.-T. Wu, J. Siegel. Buckybowls on Metal Surfaces: Symmetry Mismatch and Enantiomorphism of Corannulene on Cu(110). *Angew. Chem. Int. Ed.*, 46: 8258–8261, 2007.

126 L. Merz, M. Parschau, L. Zoppi, K. Baldridge, J. Siegel, K.-H. Ernst. Reversible Phase Transitions in a Buckybowl Monolayer. *Angew. Chem. Int. Ed.*, 48: 1966–1969, 2009.

127 T. Bauert, L. Merz, D. Bandera, M. Parschau, J. S. Siegel, K.-H. Ernst. Building 2D Crystals from 5-Fold-Symmetric Molecules. *Journal of the American Chemical Society*, 131: 3460–3461, 2009.

128 L. Zoppi, L. Martin-Samos, K. K. Baldridge. Effect of Molecular Packing on Corannulene-Based Materials Electroluminescence. *Journal of the American Chemical Society*, 133: 14002–14009, 2011.

129 G. Valenti, C. Bruno, S. Rapino, A. Fiorani, E. A. Jackson, L. T. Scott, F. Paolucci, M. Marcaccio. Intense and Tunable Electrochemiluminescence of Corannulene. *Journal of Physical Chemistry C*, 114: 19467–19472, 2010.

130 J. Mack, P. Vogel, D. Jones, N. Kaval, A. Sutton. The development of corannulene-based blue emitters. *Org. Biomol. Chem.*, 5: 2448–2452, 2007.

131 L. Kobryn, W. P. Henry, F. R. Fronczek, R. Sygula, A. Sygula. Molecular clips and tweezers with corannulene pincers. *Tetrahedron Letters*, 50: 7124–7127, 2009.

132 G. Sandi, R. E. Gerald, L. G. Scanlon, C. S. Johnson, R. J. Klingler, J. W. Rathke. Molecular orbital and Li-7 nmr investigation of the influence of curved lattices in lithium intercalated carbon anodes. *J. New Mater. Electrochem. Syst.*, 3: 13–19, 2000.

133 H. Yokoi, Y. Hiraoka, S. Hiroto, D. Sakamaki, S. Seki, H. Shinokubo. Nitrogen-embedded buckybowl and its assebly with $C_{60}$. *Nature Communications.*, 6: 8215, 2015.

134 A. V. Zabula, A. S. Filatov, S. N. Spisak, A. Y. Rogachev. M. A. Petrukhina. A Main Group Metal Sandwich: Five Lithium Cations Jammed Between Two Corannulene Tetraanion Decks. *Science*, 333: 1008–1011, 2011.

135 Q. Xie, E. Perez-Cordero, and L. Echegoyen. Electrochemical Detection of $C_{60}^{6-}$ and $C_{70}^{6-}$: Enhanced Stability of Fullerides in Solution. *Journal of the American Chemical Society*, 114: 3978–3980, 1992.

136 J. Qi, W. Hua, B. Gao. Theoretical study of two $I_h$-symmetry-breaking $C_{60}$ isomers and their chlorinated species in core-excited and ground states. *Chemical Physics Letters*, 539–540: 222–228, 2012.

137 B. Gao, L. Liu, C. Wang, Z. Wu, Y. Luo. Spectral identification of fullerene $C_{82}$ isomers. *Journal of Chemical Physics*, 127: 164314, 2007.

138 Y. Noguchi, O. Sugino. Symmetry breaking and excitonic effects on optical properties of defective nanographenes. *Journal of Chemical Physics*, 142: 064313, 2015.

139 G. Fratesi, V. Lanzilotto, S. Stranges, M. Alagia, G. P. Brivio, L. Floreano. High resolution NEXAFS of perylene and PTCDI: a surface science approach to molecular orbital analysis. *Physical Chemistry Chemical Physics*, 16: 14834–14844, 2014.

140 E. Pehlke, M. Scheffler. Evidence for Site-Sensitive Screening of Core Holes at the Si and Ge (001) Surface. *Physical Review Letters*, 71: 2338–2341, 1993.

141 M. Leetmaa, M. Ljungberg, A. Lyubartsev, A. Nilsson, L. Pettersson. Theoretical approximations to X-ray absorption spectroscopy of liquid water and

ice. *J. Electron Spectrosc. Relat. Phenom.*, 177: 135–157, 2010.

142 J. C. Hanson, C. E. Nordman. The Crystal and Molecular Structure of Corannulene, $C_{20}H_{10}$. *Acta Crystallogr. B*, 32: 1147–1153, 1976.

143 L. Hedberg, K. Hedberg. P.-c. Cheng, L. T. Scott. Gas-Phase Molecular Structure of Corannulene, $C_{20}H_{10}$. An Electron-Diffraction Study Augmented by ab Initio Normal Coordinate Calculations. *Journal of Physical Chemistry A*, 104: 7689–7694, 2000.

144 G. Chen, R. G. Cooks, E. Corpuz, L. T. Scott. Estimation of the Electron Affinities of $C_{60}$, Corannulene, and Coronene by Using the Kinetic Method. *J. Am. Soc. Mass Spectrom.*, 104: 619–627, 1996.

145 A. Bassan, M. Nyberg, Y. Luo. Identifying isomers of $C_{78}$ by means of x-ray spectroscopy. *Physical Review B*, 65: 165402, 2002.

146 C. Adamo, V. Barone. Toward reliable density functional methods without adjustable parameters: The PBE0 model. *Journal of Chemical Physics*, 110: 6158, 1999.

147 J. Stöhr. *NEXAFS Spectroscopy*. Springer-Verlag Berlin Heidelberg, 1992: Vol. 25.

148 A. Matsuura, N. Thrupp, X. Gonze, Y. Pouillon, G. Bruant, G. Onida. The ETSF: An e-Infrastructure That Bridges Simulations and Experiments. *Comput. Sci. Eng.*, 14: 22–32, 2012.

# Acknowledgements

In this acknowledgements section, I first thank Prof. Gian Paolo Brivio, my supervisor for giving me the opportunity to do this research work, for his constant motivation and guidance throughout my Ph.D. I can not express my sincere gratitude enough to my co-supervisor, Dr. Guido Fratesi, who gave me systematic training to do scientific computer simulations and analyze the results. I am grateful for his immense patience at numerous hard times, for helping me and clearing all my doubts. I am indebted to Prof. Annabella Selloni who was my collaborator during my secondment in Princeton University, USA for her constant help and support during my stay there. Many thanks to the members of my group at the University of Milano-Bicocca, Italy: Anu Baby, Abhilash Ravikumar, Moritz Muller, Aldo Ugolotti and my colleagues at Princeton University, USA: Sencer Selcuk, Xiao Shi, Ji-Ming Sun, and Hsin-Yu Ko. Thank Dr. Maria Cristina Fassina for her useful help, and thank Prof. Antonio Papagni for fruitful discussions. I am grateful to Pirelli Company for funding my PhD scholarship and paying my registration fee of Princeton University. I also acknowledge the PCAM European Doctorate Programme within which this work has been done.